NORTHWESTERN UNIVERSITY

Towards Quantum Applications of Integrated Photonic Devices

A DISSERTATION

SUBMITTED TO THE GRADUATE SCHOOL

IN PARTIAL FULFILLMENT OF THE REQUIREMENTS

for the degree

DOCTOR OF PHILOSOPHY

Field of Physics

By

Vesselin Velev

EVANSTON, ILLINOIS

September 2018

ABSTRACT

Towards Quantum Applications
of Integrated Photonic Devices

Vesselin Velev

Chip-based photonic devices are doing for optics what integrated circuits have done for electronics. By directly combining many individual components in a compact, scalable and robust way, photonic chips open the possibility for creating optical and electro-optical devices that could not be practical with discrete components. The applications for this technology are broad and far-reaching, ranging from commercial telecommunications uses to fundamental experiments which probe the physical nature of light.

In this work, we focus on novel devices targeted for quantum optics applications that harness the advantages of these integrated systems towards problems in information processing and fundamental research. In order to achieve these goals, we target devices that manipulate and generate quantum states of light. This work will present simulation and experimental results form a host of integrated materials and layouts.

First we will discuss simulation efforts for a receiver design that can selectively manipulate high-dimensional photonic signals in overlapping temporal modes. This lithium-niobate waveguide based experiment relies on precise pump waveforms to extract the target signal mode with high selectivity. The simulation and optimization efforts presented here support the experimental work carried out by other members of this group.

To complement our receiver scheme, we present a CMOS-compatible platform for telecom C-band photon pairs. This chip is based on a novel integrated waveguide which uses hydrogenated amorphous silicon as the guiding material. This short, 8-mm chip produces photon-pairs in far-detuned multiple wavelength channels simultaneously with a coincidence-to-accidental ratio as high as 400. With insignificant Raman scattering over a spectrum of at least 5 THz, this material holds promise for large-scale quantum applications, especially those based on multiplexed photon sources.

Next, we present work in silicon nitride ring and disk resonators. With a moderate $\chi^{(3)}$, but no two-photon absorption for light near 1550 nm, this material has been shown to be highly versatile for chip-based based nonlinear optics in the near infrared. In this work, we investigate all-optical switching behavior which can route and filter quantum signals without introducing degrading in-band spontaneous noise. Finally, we present simulation and preliminary experimental work towards phase-sensitive stimulated and spontaneous cascaded four-wave mixing which can be used to manipulate frequency comb generation of classical or quantum signals.

In full, we show progress towards integrated devices which can be the basis of sophisticated large-scale chip-based quantum photonic circuits communicating via optical fiber interconnects.

Acknowledgements

I have to admit, this has been such a long and tumultuous process. I could never have predicted how all this would play out the beginning. Because of this the list of people that deserve to be acknowledged is quite long.

First I'd like to thank my advisor, Prof. Prem Kumar. Over the years the group has undergone many changes and I am grateful for your guidance and perseverance. I'd also like to thank the committee, Prof. Brian Odom and Prof. Nate Stern. Thank you for your time and your guidance. Without Prof. Greg Kanter and Prof. Kim Fook Lee, I would guess a whole group of us would not be where we are today. Patience, guidance, and motivation in the right quantities. I owe a tremendous amount of my success to Prof. Yu-Ping Huang. He connected me with our Johns Hopkins collaborators and helped me prepare for multiple conference talks. Much of what is presented here is motivated by work we did together before he left. During my undergraduate times, I worked in Prof. Paul Kwiat's lab. It was an excellent group and my experiences there helped me set my course in graduate school.

At this point, I'd like to thank every member of the group that I interacted with over the seven years I was here. I'd especially like to thank Abijith Kowligy. His physics and optics knowledge was second to none. When in real doubt, ask Abijith. He would always take the time to discuss. I shared an office with Neil Corzo for

a long time and helped me tremendously before he left. So did Tim Rambo and Paritosh Manurkar. I have to mention Gideon Alon, who I worked with at the very start of my time in Prof. Kumar's Lab and helped me get going. At this point I'd like to thank our collaborators, Prof. Mark Foster and Prof. Amy Foster, and their former student Ke-Yao Wang. We spent intense weeks working together during his visits. During my visit to Sandia, I cannot thank Dr. Ian Frank and Dr. Ryan Camacho enough. Ian was extremely patient and taught me everything I know about device fabrication.

I have also thank Sammy Nowierski and the opportunity you gave me in California. In the same way, I am grateful to Julia Larikova for the work we did together and the contacts she made for me. I owe a lot to her. Brad Elkus, we had a great time together and it was a pleasure working with you. I wish you the best, and hope the chips fall your way. François Callawart, we became friends over our love of cycling. Then over coffee one day, we realized we could work together. The 3-D printed inverse design experiments were so different than my optics work. And quite fruitful.

I'd also like to thank Prof. Michael Schmitt for championing my cause at the beginning. I hope I repaid some of that confidence as your teaching assistant. And speaking of teaching, I cannot speak highly enough of Prof. Krusberg. Her example showed me what it means to teach undergraduate physics. When my motivation in the lab wavered, she showed me something new that I found satisfying and important. What she and our students taught me has already proven invaluable.

Outside of the lab, I cannot stress enough how important these people have been to me and my last seven years in Chicago. I'd like to thank Nick and Jessica Boi. Our friendship started at UIUC and has only gotten stronger. It's not going

anywhere. Chris Pike took a chance following me into the great open expanse of Kansas so I returned the favor by following him to a tiny village in northern Spain. I also have to include his wife, Elena Rodina. No one is more cosmopolitan. Dinner will be missed. Vishal Soni and George Mossessian came up with me as physics students at UIUC. They keep me honest. With that, I can't fail to include Ethan Stone, look where we are now.

And of course, where would I be without Katie DeAmico and my parents, Madlena and George Velev. Their contributions are too vast to describe.

Acronyms

$\chi^{(2)}$ second-order nonlinearity. 35, 39, 40, 52, 53, 56

$\chi^{(3)}$ third-order nonlinearity. 39, 91, 95, 122, 132

a:Si-H hydrogenated amorphous silicon. 32, 33, 84, 89, 91, 140

ARM advanced RISC machine. 167, 168

c-Si crystalline silicon. 32, 84, 85, 89

CAR coincidence-to-accidental ratio. 33, 34, 84, 89, 91

CMOS complementary metal-oxide-semiconductor. 34, 44, 84, 91

CMT coupled mode theory. 93

CTF complex transfer function. 68, 70, 71, 171, 173, 174

CW continuous wave. 122, 173

DCF dispersion-compensating fiber. 74

EDFA erbium-doped fiber amplifier. 54, 122, 133, 177

EOM electro-optic modulator. 132, 139

FCA free-carrier absorption. 84

FDM finite-difference method. 56

FEM finite element method. 34, 93, 94, 97, 99, 106, 108

FFT fast Fourier transform. 56, 59, 164, 165

FPBS fiber polarization beam splitter. 85

FPC fiber polarization controller. 85

FSR free-spectral range. 33, 48, 100, 103, 122, 130, 131, 133, 140

FWHM full-width at half-maximum. 47

FWM four-wave mixing. 26, 33, 34, 39, 50, 51, 85, 87, 101, 104, 110, 118, 127, 132, 136–138, 140

GPIB General Purpose Interface Bus. 176

GPU graphics processing unit. 165, 166

GVD group-velocity dispersion. 85, 96, 104, 127, 131, 173

I/O input/output. 169, 177

JHU Johns Hopkins University. 33, 84

LN lithium niobate. 32, 33, 53, 101, 122, 133, 139, 195

MEMS microelectromechanical system. 122

NLS nonlinear Schrödinger equation. 33, 58

OAWG optical arbitrary waveform generator. 54, 66, 76, 79, 134, 139, 177

OSA optical spectrum analyzer. 47, 128, 131, 176, 177

PC personal computer. 169

PM phase-matching. 35, 41, 43, 62, 68, 69, 71, 78, 94, 103, 104

PML perfectly-matched layer. 106

PPKTP periodically-poled potassium titanyl phosphate. 53

PPLN periodically-poled lithium niobate. 76

Q-factor quality factor. 33, 46, 47, 98, 100, 109, 110, 138, 140

QFC quantum frequency conversion. 39, 52, 53, 63, 66, 76, 77, 104

QPM quasi-phase match. 33, 41, 43, 59, 61, 77, 80, 139, 155, 195, 197

RAM random access memory. 168

RF radio frequency. 54, 80, 132–134

SFG sum-frequency generation. 35, 39, 40, 52, 53, 56, 68, 173, 195

SHG second-harmonic generation. 39, 68, 70, 171, 174, 195, 197

Si_3N_4 silicon nitride. 32, 34, 44, 48, 96, 104, 109, 117, 139, 195

SMF single-mode fiber. 85, 132, 140

SPD single-photon detector. 53, 86, 87

SPDC spontaneous parametric down-conversion. 39, 53, 62, 66, 79

SVA slowly-varying amplitude. 40

TE transverse electric. 49, 85, 101, 103, 104, 107

TGF triple-pass grating filter. 85, 87

THG third-harmonic generation. 39

TM transverse magnetic. 49, 101, 104, 107

TPA two-photon absorption. 39, 84

USBTMC USB Test & Measurement Class. 176

WDM wavelength-division multiplexing. 85

WG waveguide. 33–35, 39, 40, 44, 47, 49, 52, 53, 56, 58–60, 66, 68, 70, 77, 79, 84, 85, 87–89, 91, 93, 107, 110, 114, 115, 139, 140, 155, 164, 165, 170–172, 195, 197

WGM whispering gallery mode. 31, 43–45, 49, 80, 93, 94, 106, 107

Contents

List of Figures

List of Tables

List of Code

1 Introduction

The manipulation of light in dielectric media has taken on ever greater importance. From the underpinnings of the information revolution [1, 2] to the most stable frequency sources [3] known, manipulation of optical systems has become a fundamental building block for classical communications technology and experiments for fundamental scientific understanding.

The invention of the laser [4] made powerful, coherent optical fields accessible which allowed the experimental study of the nonlinear dependence of material polarization on electric field to follow quickly thereafter [5]. Nonlinear interactions have been extensively studied in bulk materials [6] and linear cavities. whispering gallery mode (WGM) resonators are especially of interest because they offer longer light confinement [7].

With advances in fabrication techniques, devices with especially small modal confinement and impressively long photon lifetimes have been demonstrated across a variety of materials [8, 9, 10, 11, 12]. This directly leads to a large cavity enhancement which allows novel nonlinear optics regimes to be probed [12, 13, 14, 15, 16, 17, 18, 19].

At the same time, interest in harnessing quantum mechanics for information processing has intensified tremendously [20, 21]. The implementations of fundamental elements of these protocols have been demonstrated in optical, atomic, and

condensed matter systems [21]. However, all suffer to some extent with issues of stability and scalability. One way to address these concerns for optical systems is on-chip integration using fabrication techniques shared with classical photonic chip devices and the electronics industry.

Leveraging the maturity of silicon chip fabrication, honed over many decades for transistor fabrication to manipulate quantum states of light in on-chip devices combines all these advances. In this prospectus, we will discuss two materials that share this integrability: silicon nitride (Si_3N_4) and hydrogenated amorphous silicon (a:Si-H). Work to integrate lithium niobate (LN) is also progressing [22, 23, 24].

With a mature fabrication capability, Si_3N_4 devices promise extremely low loss and good nonlinear properties [25, 26, 27]. Unlike crystalline silicon (c-Si) devices, for example, Si_3N_4 does not suffer from two-photon absorption in the telecom spectral C-band (roughly 1527 to 1568 nm), making fiber-compatible parametric processes possible[28, 29, 30]. We have proposed efficient on-chip sources for the generation of temporally long photon pairs and photon manipulation in this material precisely for this reason [17].

In contrast, a:Si-H has shown extremely high optical nonlinearities, 2 orders of magnitude higher than Si_3N_4 [31, 32, 33]. Phase-sensitive amplification [34] and picosecond all-optical switching in resonators has been demonstrated in this material [35]. The low deposition temperature of this material leaves the door open for its integration with other dielectrics and electronic elements. Despite its amorphous nature, Raman gain is moderate in the telecom C-band of the optical spectrum. We demonstrated this by observing high-purity photon-pair generation at two wide detunings [36].

1.1 Chapter Guide

In Chapter 2, general properties of integrated optical systems are discussed. We highlight the mode structure of waveguides (WGs) and resonators. We introduce the phase-matching relations for $\chi^{(2)}$ materials in traveling wave devices. Specific emphasis is placed on periodic poling to achieve quasi-phase match (QPM) for parametric processes because we refer back to this concept in Chapter 3. Switching to resonant systems, we discuss the concepts of quality factor (Q-factor), free-spectral range (FSR), and finesse to describe the linear properties and field enhancement present in these systems, with an emphasis on the compact, thin, rectangular cross-section devices typical on chip. Finally we discuss the necessary conditions for FWM in these structures. Chapters 6, 7, 8 are based on these concepts.

In Chapter 3, we cover work related to the mode-selective receiver design. This device combines the uses the tailored waveform of a pump signal, which when incident on a WG (LN in this case), selectively upconverts a single signal mode. We solve the nonlinear Schrödinger equation (NLS) equations using the split-step Fourier method solver. When we combine this with a random-walk optimization routine, we can create optimized pump shapes to maximize mode-selectivity. This receiver also has the advantage of upconverting the signal light from the telecom C-band to the visible spectrum, allowing the use of efficient silicon single photon counters.

In Chapter 4, we discuss the experimental generation of photon pairs in the C-band using FWM. In collaboration with Johns Hopkins University (JHU), we test a novel a:Si-H WG chip which has exceptional effective optical nonlinearity. We characterize the coincidence-to-accidental ratio (CAR) of the pair source and investigate the Raman gain present at two different pump detunings. Despite small

measured Raman gain, we measured exceptionally high CAR of up to 400. In this metric, we compete with cryogenic-cooled optical fiber sources with a 8-mm long, room-temperature, complementary metal-oxide-semiconductor (CMOS)-compatible WG.

Chapter 5 is an overview of resonator simulation. This work focuses on the eigenmode solver developed within the commercial finite element method (FEM) solver COMSOL. With our implementation, the model assumes only rotational symmetry of the system to solve for the eigenmodes of a resonator with arbitrary cross-section. We use this code to predict the dispersion and mode volume of the chip-based Si_3N_4 devices in our possession to estimate their nonlinear properties.

In Chapter 6, we cover preliminary work for the chip-based resonator experiments to follow. As these devices were fabricated by Dr. Ryan Camacho's group at Sandia National Laboratory, the author's on-site experience is detailed. We discuss details of the design of our chip coupling setup and it's performance.

In Chapters 6, 7, 8, we study nonlinear interactions in Si_3N_4 devices. The first chapter focuses on the enclosure and alignment setup to couple light into the resonator. The second discusses an all-optical switching scheme. The final chapter focuses on experiments designed to seed a cascaded FWM interaction with a 3 pump waves with a fixed phase relationship.

2 Waveguide and Resonator Basics

In order to discuss the propagation of light through dielectric optical medium, we must begin with Maxwell's equations. From these, we will derive the optical wave equation which will be key in understanding the nonlinear interactions in our devices.

After setting this basic framework, we will discuss nonlinear interactions in a second-order nonlinearity ($\chi^{(2)}$) WG device. The phase-matching (PM) requirements of the device will be considered, along with a method to overcome this limitation. This background forms the foundation for the simulations of sum-frequency generation (SFG) in Chapter 3.

We will also cover the unique properties of microresonator devices discussed in greater detail in Chapter 5. A mathematical understanding of the cavity enhancement factor will be shown. We will describe the mode structure basics. Next, the polarization properties of the device will be discussed. Finally, the PM conditions will be introduced.

2.1 Maxwell's Equations

Maxwell's equations, written in SI units are

$$\nabla \cdot \mathbf{D} = \rho, \tag{2.1.1}$$

$$\nabla \cdot \mathbf{B} = 0, \tag{2.1.2}$$

$$\nabla \times \mathbf{E} = -\frac{\partial \mathbf{B}}{\partial t}, \tag{2.1.3}$$

$$\nabla \times \mathbf{H} = \frac{\partial \mathbf{D}}{\partial t} + \mathbf{J}, \tag{2.1.4}$$

where $\mathbf{D}$ is the displacement field, $\mathbf{E}$ is the electric field, $\mathbf{H}$ is the magnetic field, and $\mathbf{B}$ is the magnetic flux density [37, 38, 39]. We are interested in the solution to the wave equation in a material in which there are no free currents ($\mathbf{J} = 0$) and no free charges ($\rho = 0$). The linear constitutive relations are $\mathbf{H} = 1/\mu_0\mathbf{B}$ and $\mathbf{D} = \epsilon\mathbf{E}$, because in the materials we are interested in, the magnetic permeability is equal to that of the vacuum [6, 1]. In order to derive the wave equation for the optical light, we now take the curl of the Maxwell-Faraday equation, (2.1.3):

$$\begin{aligned} \nabla \times (\nabla \times \mathbf{E}) &= \nabla(\nabla \cdot \mathbf{E}) - \nabla^2\mathbf{E} \\ &= \nabla \times (-\frac{\partial \mathbf{B}}{\partial t}) \\ &= -\frac{\partial}{\partial t}(\nabla \times \mathbf{B}) \\ &= \frac{\epsilon_r}{c^2}\frac{\partial^2 \mathbf{E}}{\partial t^2}, \end{aligned} \tag{2.1.5}$$

where $c = 1/\sqrt{\mu_0\epsilon_0}$ and $\epsilon_r = \epsilon/\epsilon_0$ [39, 6]. With a straightforward substitution, this will also explain the optical nonlinearity effects due to a modification of the constitutive relation for the electric field [6, 1].

2.1.1 Boundary Conditions

We need to consider the interaction of the electric field at the interface between two materials. The guiding properties of the devices and the evanescent coupling of light between them depends on the boundary conditions.

The fields behave according to the following relations at the interface of two materials:

$$\epsilon_1 E_1^{\perp} = \epsilon_1 E_2^{\perp}, \tag{2.1.6}$$

$$\mathbf{E}_1^{\parallel} = \mathbf{E}_2^{\parallel}, \tag{2.1.7}$$

$$B_1^{\perp} = B_2^{\perp}, \tag{2.1.8}$$

$$\frac{1}{\mu_1}\mathbf{B}_1^{\parallel} = \frac{1}{\mu_2}\mathbf{B}_2^{\parallel}. \tag{2.1.9}$$

The subscript denotes which side of the interface the field refers to. The relations differentiate between the components of a field parallel ($\parallel$) and perpendicular ($\perp$) to the boundary [39, 6, 40].

For the materials considered here the permeability of each part is equal to that of the vacuum ($\mu_1 = \mu_2 = \mu_0$). Therefore the magnetic fields and densities are continuous on either side of an interface, a property which we will exploit when solving the wave equation numerically to determine the modes of a microresonator later in this work [40].

2.1.2 Optical Nonlinearity

The optical nonlinearity enters the Maxwell equations through a modification of the linear constitutive relations. As the intensity of an optical beam increases, the

nonlinearities in the response of the atoms that constitute the material become more apparent [6], but even the vacuum becomes nonlinear under a high enough electric field [41, 42]. A coherent superposition can form, leading to radiation at a different frequency in a well-defined beam.

Assuming an isotropic material for clarity, the dielectric tensor simplifies to a scalar. The relation between the displacement field ($\mathbf{D}$) and the electric field ($\mathbf{E}$) contains the nonlinear polarization, $\mathbf{P}_{\mathrm{NL}}$ as

$$\mathbf{D} = \epsilon_0 \epsilon_r \mathbf{E} + \mathbf{P}_{\mathrm{NL}}, \tag{2.1.10}$$

where the first term on the l.h.s represents the linear effect due to the refractive index. A simple perturbative expansion of $\mathbf{P}_{\mathrm{NL}}$ in terms of the electric susceptibility of the material (χ), is

$$\mathbf{P}_{\mathrm{NL}} = \epsilon_0 \left[\chi^{(2)} \mathbf{E}^2 + \chi^{(3)} \mathbf{E}^3 + \dots \right], \tag{2.1.11}$$

with the number of relevant terms in the expansion constrained by the strength of the field and the particular material properties. While all materials have odd-order nonlinear coefficients ($\chi^{(n)}$ for $n = 1, 3, \dots$), materials which are centrosymmetric have zero even-order bulk nonlinearities, which is true for described microresonator work. The updated wave equation including the nonlinear polarization is

$$\nabla^2 \mathbf{E} - \frac{\epsilon_r}{c^2} \frac{\partial^2 \mathbf{E}}{\partial t^2} = \frac{1}{\epsilon_0 c^2} \frac{\partial^2 \mathbf{P}_{\mathrm{NL}}}{\partial t^2}. \tag{2.1.12}$$

2.2 Waveguide Interactions

A WG, is quite simply, a structure that can guide electromagnetic waves. The intuitive understanding of the operation of these devices does not vary greatly across the many orders of magnitude for electromagnetic oscillation, from radio waves to x-rays, but here we confine ourselves to optical devices in the visible and telecommunications (from roughly 500 nm to 2 μm in wavelength) frequency bands [43]. The two most common devices we are most familiar with are the ubiquitous optical fiber and waveguides, either bulk crystal or on a photonic chip.

Compared to other easily-accessible media, such as optical fiber, bulk or chip-based waveguides promise much higher effective optical nonlinearity which allows meaningful nonlinear interaction in a compact space at lower pump powers. Waveguide devices are used for efficient frequency-conversion processes, such as SFG, and second-harmonic generation (SHG) in devices with a strong $\chi^{(2)}$ or FWM, two-photon absorption (TPA), and third-harmonic generation (THG) in materials due to the third-order nonlinearity ($\chi^{(3)}$) [6, 1]. While these processes can be convincingly described by classical electrodynamics, other processes such as spontaneous parametric down-conversion (SPDC) [44, 45] or quantum frequency conversion (QFC) [46] cannot. With the help of quantum mechanics, the same optical nonlinear material properties can be used to generate entangled photons (SPDC) or translate the carrier frequency of quantum signals (QFC), for example. There are just too many examples of waveguide uses to list.

2.2.1 Waveguide Nonlinear Interaction

In order to solve for the nonlinear interaction in a $\chi^{(2)}$ WG, we start with Eq. 2.1.12. We first assume that the electric field, $\mathbf{E}$, can be represented by only the amplitude

of the wave, $A(z)$, where $\hat{z}$ is along the length of the WG as

$$\mathbf{E}(\mathbf{r},t) = E(z,t) = A(z)e^{i(kz-\omega t)} + \text{c.c.}, \tag{2.2.1}$$

where k is the wavevector, defined as $n(\omega)\omega/c$, and ω is the oscillation frequency. This is valid for devices that have single spacial modes, which in itself is critical for good performance. The applied fields are represented as $E_i(z,t)$ where $i = 1, 2$ for the two input optical frequencies of light, while the SFG is $i = 3$. The amplitude of the nonlinear polarization is

$$P_{\text{NL}} = 4\epsilon_0 d_{\text{eff}} A_1 A_2 e^{i(k_1+k_2)z} \tag{2.2.2}$$

under the assumption of a constant geometry with a fixed polarization. d_{eff} is the effective optical nonlinearity which is a function of the $\chi^{(2)}$ strength and the overlap of the spacial distributions among the 3 modes. Eq. 2.1.12 can now be simplified to

$$\frac{d^2A_3}{dz^2} + 2ik_3\frac{dA_3}{dz} = -\frac{4d_{\text{eff}}\omega_3^2}{c^2}A_1A_2e^{i\Delta kz}, \tag{2.2.3}$$

where $\Delta k = k_1 + k_2 - k_3$, the phase difference due to wavevector mismatch. The slowly-varying amplitude (SVA) approximation allows us to neglect the first term of the the left side as, generally

$$\left|\frac{d^2A_3}{dz^2}\right| \ll \left|\frac{dA_3}{dz}\right|. \tag{2.2.4}$$

Integration of the resulting equation gives the amplitude of the resulting wave at a frequency of $\omega_3 = \omega_1 + \omega_2$,

$$A_3(L) = \frac{2id_{\text{eff}}\omega_3^2}{k_3c^2}A_1A_2\int_0^L e^{i\Delta kz}\,dz = \frac{2id_{\text{eff}}\omega_3^2}{k_3c^2}A_1A_2\left(\frac{e^{-i\Delta kL}-1}{i\Delta k}\right). \tag{2.2.5}$$

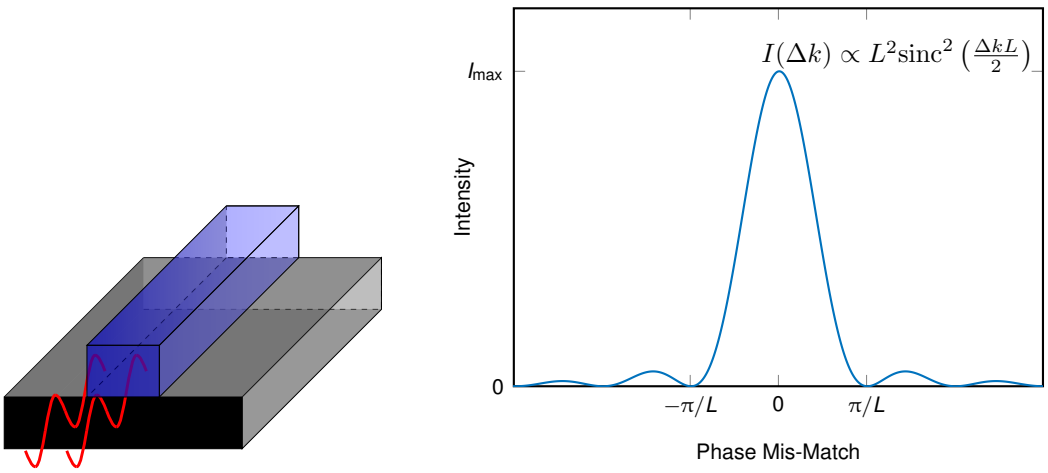

(a) (b)

Figure 2.2.1: (a) Shows a typical channel WG geometry. The blue element represents the guiding dielectric, while the grey slab is the cladding. (b) The intensity of the sum-frequency wave scales with the square of the length of the WG (L) while the phase-matching curve narrows in frequency with L.

From this equation, it is easy to see that the intensity of the upconverted light,

$$I_3(L) \propto L^2 \mathrm{sinc}^2\left(\frac{\Delta k L}{2}\right), \tag{2.2.6}$$

is very strongly connected to the wavevector mismatch.

2.2.2 Waveguide Phase Matching Considerations

In order to overcome the limitations of natural PM as described in the previous subsection, QPM gratings were developed [6, 47]. If $\Delta k \neq 0$, as the light propagates through the material, the nonlinear mixing process oscillates between generation and depletion of the sum frequency wave. However, a spacial periodic inversion of the c-axis of the material effectively changes the sign of the d_{eff} term. When a grating with the correct poling structure is implemented, the inherent wavevector mismatch can be compensated for and *PM* will be achieved as shown in Fig. 2.2.2.

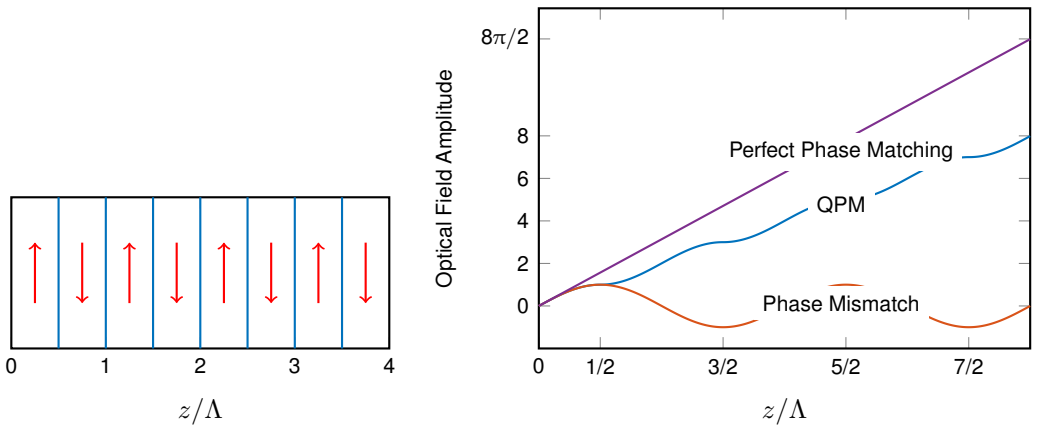

(a) (b)

Figure 2.2.2: (a) A periodically-poled WG, where Λ is the polling period. The axis of the crystal is inverted, changing the sign of the effective nonlinearity as shown by the arrows. This is the most straightforward type of QPM structure. (b) Three different types of PM conditions are shown here. In the negligible pump depletion case, with ideal PM ($\Delta k = 0$), the amplitude in the sum-frequency grows linearly. In a structure of the type shown in (a), the amplitude increases monotonically but only to a level $2/\pi$ as high as the ideal case. For a case with phase mismatch, the output amplitude is likely near zero.

The simplest grating structure is a inversion of the sign of d_{eff} following a square-wave function with a period of Λ,

$$d(z) = d_{\text{eff}} \operatorname{sign}\left[\cos(2\pi z/\Lambda)\right], \tag{2.2.7}$$

where $d(z)$ is the spacial dependence of the coupling coefficient. Analytically, it is very revealing to construct the Fourier series of the grating,

$$d(z) = d_{\text{eff}} \sum_{m=-\infty}^{\infty} G_m e^{-imkz}, \tag{2.2.8}$$

where $k_m = 2\pi/\Lambda$ is the magnitude of the grating vector. The Fourier coefficients

for a uniform grating of the form in Eq. 2.2.7 are given by

$$G_m = \frac{2}{m\pi}\sin(m\pi D), \tag{2.2.9}$$

where D is the duty cycle of the grating. Typically, we are only interested in the first term ($m = 1$), as this has the largest coefficient and is therefore the most efficient. With a duty cycle of 50%, the QPM first-order grating term is

$$d(z) = \frac{2}{\pi} d_{\text{eff}} e^{ikz}. \tag{2.2.10}$$

By replacing d_{eff} with $d(z)$ in Eq. 2.2.5, and completing the integration, we show that the intensity depends on length in the original sinc squared fashion as shown in Fig. 2.2.1b, but the phase mismatch is given by $\Delta k_{\text{QPM}} = \Delta k - 2\pi/\Lambda$ and the amplitude is decreased by a factor of $2/\pi$ [6]. From here it is easy to show that

$$\Lambda = \frac{2\pi}{\Delta k} \tag{2.2.11}$$

for a periodically poled grating.

We should note that there are many other forms of QPM gratings possible [48, 49]. The goal of these schemes is typically to increase the extinction of the PM curve, which is poor near the secondary maxima of the sinc function, to narrow or broaden the peak, or to introduce multiple PM peaks [50].

2.3 Whispering-Gallery Mode Microresonators

Axisymmetric dielectric resonators guide light in so-called WGMs near the resonator's periphery. A unique property of these devices is that they only support

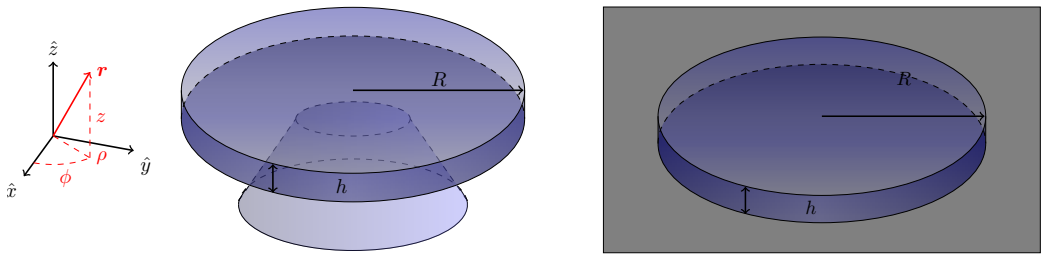

(a) (b)

Figure 2.3.1: Two types of geometries will be discussed in this work. (a) is the typical geometry associated with our Si_3N_4 devices. The pedestal mounted disk resonator is surrounded by air on all sides. (b) is a microdisk mounted on a cladding, similar to the WG devices shown earlier. This is the typical geometry for a:Si-H devices, though some are rings and not disks. In both cases, the coupling (bus) WGs are not shown.

certain eigenmodes of optical radiation. These eigenmodes constitute the eigenfrequency of the resonance, along with the spacial distribution of the electromagnetic field of the radiation. The cavity has a discrete spectrum of eigenmodes, with finite (though sometimes quite long) lifetimes. A WG device however, supports a continuum of frequencies in a band for which it guides a particular spatial eigenmode.

For the eigenfrequency, light coupled into this cavity relies on total internal reflection from the curvature of the walls of the cavity to form a standing wave. The corresponding eigenmodes are called WGMs because of an identical phenomena observed for sound waves in St. Paul's Cathedral in London by Lord Raleigh [51]. Optical materials that support WGMs have been shown in various materials and configurations for a wide range of applications [52, 53, 54, 7, 10, 55, 56, 17]

In this dissertation, we focus on optical resonators made of Si_3N_4. These materials have the advantage of CMOS compatibility, which allows them to be grown on a silicon wafer. These devices can then be integrated into larger photonic circuits in

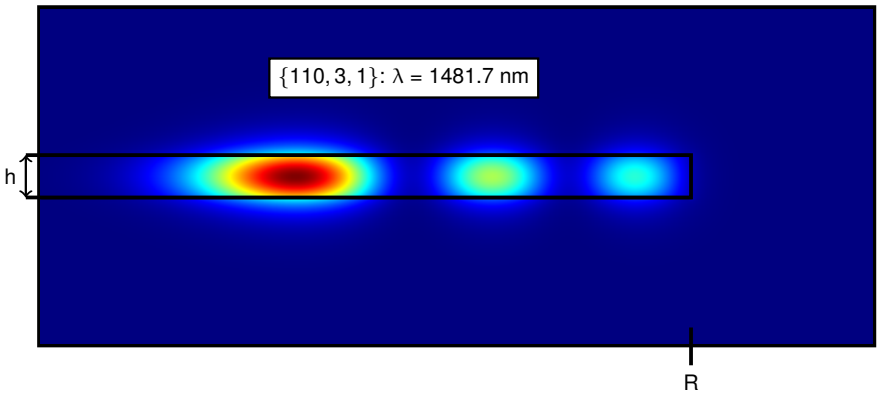

Figure 2.3.2: The mode shape depicted here in cross-section is typical for a integrated chip-based Si_3N_4 device. The geometry parameters are $R = 20\,\mu$m and $h = 300\,$nm. The mode number is $\{110, 3, 1\}$ and has TE polarization. The plot shows the absolute value of the electric field magnitude.

order to build scalable and ultra-stable circuit-like implementations. Both of these materials are centrosymmetric and possess a leading order $\chi^{(3)}$ nonlinearity.

2.3.1 Mode Families

The geometry of the resonator constrains the spatial distribution of the electromagnetic field. However, the axial symmetry of the device manifests itself in symmetries of the eigenmodes themselves. This lends itself to a simple characterization based on three integers, $\{m, n, k\}$. While most devices also support two orthogonal polarizations for each mode number (as long as the mode itself is guided), the polarization basis will be dealt with explicitly in a later subsection.

Mode number m is especially important as it plays the role of the wave-vector in a resonator. While the linear momentum, k is not well defined in a cylindrical geometry because it depends on the radial position, ρ, which varies between eigenmodes, the angular momentum is. Due to the axial symmetry of the ideal WGM resonator, the electric field of the resonator mode depends on this value explicitly,

as $\mathbf{E} \propto e^{im\phi}$, where ϕ is the azimuthal coordinate. The rest, $\{n, k\}$, correspond to the number of maxima, or lobes, of the electric field in the $\hat{\rho}$ and $\hat{z}$ directions, respectively. It is important to note that some ring structures, by design, support only the fundamental eigenmode $\{m, 1, 1\}$. Similarly, thin disks may only support one mode in the $\hat{z}$ direction, which is true for most disk devices we will discuss. The notation will be shorted from $\{m, n, 1\}$ to $\{m, n\}$, where the last term is implicitly 1.

While a group of modes with a common m can be considered of the same family, only the primary mode, $\{m, 1, 1\}$ of a given polarization, will have the smallest mode volume within this family. It will also have the lowest eigenfrequency. These primary modes are important because they will maximize the cavity enhancement and have the best performance for nonlinear interactions [13, 17, 57].

2.3.2 Quality Factor

It is only an approximation that the frequency spectrum of a resonator constitutes discrete delta functions. In any real cavity, there is a narrow band of frequencies around the central eigenfrequency which are supported. The important source of this broadening of the cavity line width is due to dissipation of energy in the dielectric material of the cavity or scattering with the walls. The Q-factor is defined as

$$Q = \omega_0 \frac{U}{P_{\mathrm{L}}} \tag{2.3.1}$$

where ω_0 is the center frequency of the resonance, U is the energy in the optical mode, and P_{L} is the power dissipated out of the resonator. As $P_{\mathrm{L}} = -dU/dt$, a simple restatement of the above equation leads to the solution of the energy in the mode as a function of time, $U(t) = U_0 e^{-\omega_0 t/Q}$. Therefore, the Q-factor can also be

expressed as

$$Q = \omega_0 \tau = \frac{\omega_0}{\gamma_0}, \tag{2.3.2}$$

where τ is the relaxation time for the cavity and γ_0 is the full-width at half-maximum (FWHM) of $U(\omega)$. While this formula for the Q-factor is very much general, in experimental settings, the material absorption, surface scattering, bending losses, and and resonator-to-WG coupling all contribute individual γ terms that sum constructively [9, 58]. These terms represent individual Q-factors whose reciprocals sum as

$$\frac{1}{Q_{\mathrm{T}}} = \frac{1}{Q_{\mathrm{I}}} + \frac{1}{Q_{\mathrm{C}}}. \tag{2.3.3}$$

Q_{T} represents the total Q-factor factor, which can, for example, be measured on a coupled system by sweeping a tunable-frequency laser and measuring the width of the resonance, $\delta\omega$ on an optical spectrum analyzer (OSA), as $\delta\omega = \gamma_{\mathrm{T}}$. It is comprised of the resonator-WG coupling Q-factor, Q_{C} and the intrinsic resonator Q-factor which is broken up via

$$\frac{1}{Q_{\mathrm{I}}} = \frac{1}{Q_{\mathrm{R}}} + \frac{1}{Q_{\mathrm{S}}} + \frac{1}{Q_{\mathrm{A}}} \tag{2.3.4}$$

where Q_{R} is due to bending loss, Q_{S} is due to scattering, mainly due to surface imperfections, and Q_{A} is due to material absorption [58, 59].

The Q-factor will play an important part in all discussions of cavity performance in the rest of this dissertation. It is the key to a micro-resonator's filtering and an integral part of its cavity enhancement as shown below.

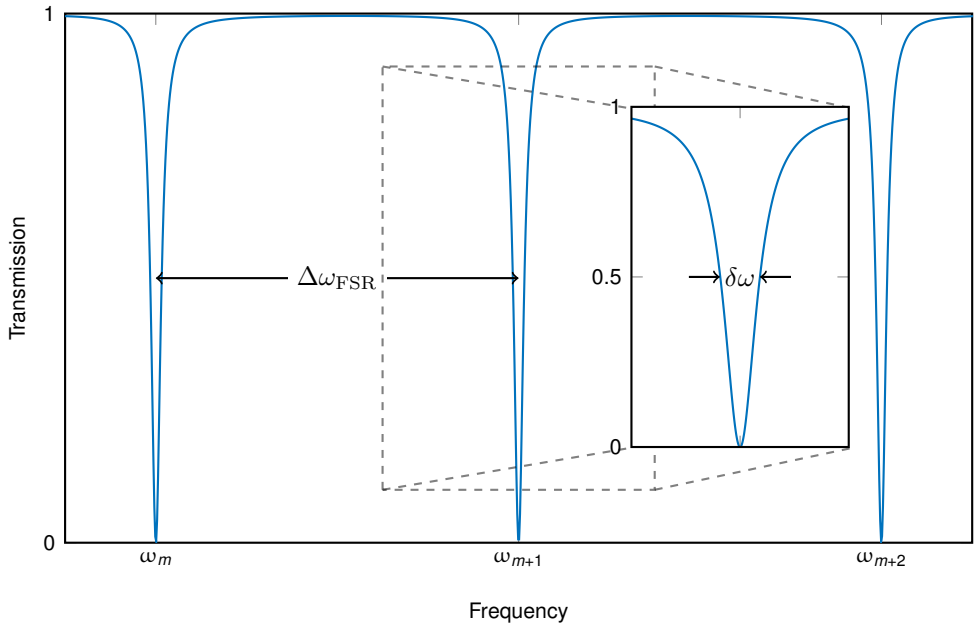

Figure 2.3.3: This is the transmission spectrum from a bus WG critically coupled to a microresonator. The dips are due to light coupling into the cavity. The FSR of a resonator is the frequency difference of two primary modes. The inset shows that the linewidth of a coupled cavity is $\delta\omega$, which is related to the total Q-factor of the cavity via $Q = \omega_m/\delta\omega$.

2.3.3 Free-Spectral Range and Finesse

The FSR of a cavity is defined as the frequency spacing, $\Delta\omega_{\mathrm{FSR}}$ between modes. This can be defined between different mode numbers, such as the spacing in eigen-frequency between the $\{m+1, n, k\}$ and $\{m, n, k\}$ mode. However, as shown in Fig. 2.3.3, we will define it as the difference between the primary modes. This parameter is proportional to the inverse of the radius of the disk. For a square Si_3N_4 microdisk resonator of radius 30 μm and a thickness of 350 nm (similar to that in Fig. 2.3.2), the FSR in the telecommunications C spectral band is 6 to 7 nm.

A key advantage of axial-symmetric cavities is the large build-up of photons in

their eigenmodes. This build-up is proportional to the finesse, $\mathcal{F}$, defined as

$$\mathcal{F} = \frac{\Delta\omega_{\mathrm{FSR}}}{\delta\omega}. \tag{2.3.5}$$

The circulating power scales with finesse as $\mathcal{F}/(2\pi)\,P_{\mathrm{C}}$, where P_{C} is the power coupled into the resonator from the external WG. For the same cavity used in the example above, $\mathcal{F} \approx 5,000$ for $Q_{\mathrm{T}} = 1 \times 10^6$, so if $P_{\mathrm{C}} = 1\,\mathrm{mW}$, the circulating power is over 750 mW. Intuitively, this enhancement is due to the standing wave formed inside the resonator by the large difference between the time light takes to complete a round trip compared to the time it remains in the cavity on average.

2.3.4 Polarization of Whispering Gallery Modes

Even a resonator fabricated from a homogeneous material can support modes of two polarizations in the same way a WG can. The accepted definitions of transverse electric (TE) and transverse magnetic (TM) modes are as follows: TE modes have $E_z = 0$ everywhere, while TM modes have $B_z = 0$ everywhere. In a WGM resonator, the same conventions hold only approximately, especially for devices that have lower symmetry (a shallow wedge shape, for example [60]). Fig. 2.3.4 shows the different shapes for an example mode with the same mode number, but for different polarizations. The results are from a full-vector numerical solver discussed in Ch. 5 [17, 40].

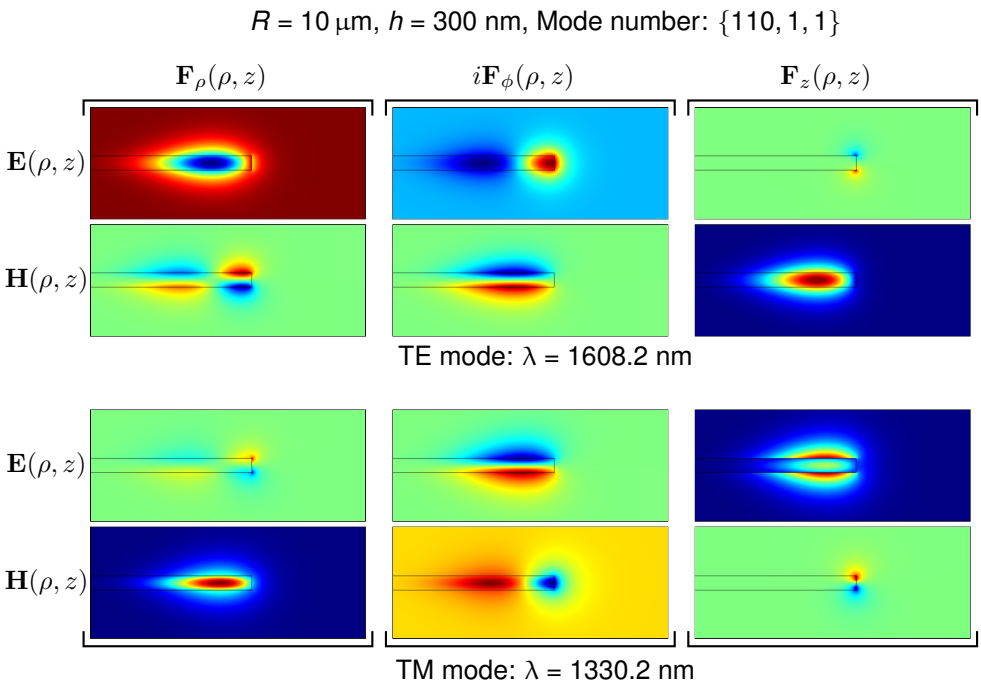

Figure 2.3.4: The numerical simulation for two eigenmodes differing only in polarization of a Si_3N_4 resonator is shown here. Note the difference in eigenfrequency. The columns show the different components (ρ, ϕ, z) of the field vectors, while the rows show the **E** and **H** fields of the two polarizations. The color scale represents the field magnitude (each component is only real) of that component only. The scale is relative.

2.3.5 Phase Matching in Micro-Resonators

For a FWM interaction, the energy conservation condition is easily stated in a frequency-equivalent manner (as $E = \hbar\omega$) as

$$\omega_1 + \omega_4 = \omega_2 + \omega_3, \tag{2.3.6}$$

where each frequency $\omega_i, i \in \{1, 2, 3, 4\}$ is an eigenfrequency of the micro-resonator, monotonically increasing. The best performance requires four simultaneous resonances, although this is not strictly necessary [61]. Momentum conservation is

expressed as

$$m_1 + m_4 = m_2 + m_3, \tag{2.3.7}$$

where m_i is the modal number. Because for a given m, the frequency-dependent dispersion properties of the material govern the corresponding eigenfrequency of the primary mode, meeting both of these conditions in practice is somewhat difficult. This is especially true for smaller devices.

There are various methods used to overcome this challenge, these fall into two categories: quasi-phase matching, and geometry engineering. For the devices of interest, we will use geometry engineering (or polarization mode selection) as it preserves the high optical nonlinearity of the material. Another consideration is that generally even moderate pump powers needed for FWM will disturb the cavity due to thermal effects.

3 Quantum Frequency Conversion Simulation

The combination of nonlinear media with strong classical waveforms has opened up new applications for manipulating quantum signals [16]. Similarly, fiber optics is a strong candidate for the exchange of information between nodes of a quantum network. Tools are needed with are capable of manipulating and measuring spatiotemporal modes of a quantum optical signal. Using QFC, we propose a mode-selective quantum signal upconverter. In this chapter, we simulate a receiver which is capable of manipulating arbitrary optical waveforms while, in principle, exhibiting extremely low loss and noise. Our technique relies on a SFG process in a $\chi^{(2)}$ WG where the pump pulse is generated in an arbitrary waveform. The signal is a waveform comprised of a set of orthogonal yet spatially, spectrally and temporally overlapping time modes indicative of those generated by an entangled photon source. The simulation work aims to optimize the waveform of the pump in order to select out an individual mode of this basis by frequency upconversion [62, 63, 16, 64, 65].

3.1 Quantum Optical Arbitrary Waveform Manipulation Simulations Introduction

We present numerical simulations for an optical technique capable of temporal mode selectivity for quantum signals. Various applications such as ultradense quantum coding or high-speed quantum computing can benefit from this optical technique [66, 67].

An entangled photon source, such as a SPDC crystal, naturally produces photons in superposition of overlapping temporal modes. We harness this mode-set for our system. This simulation specifically focuses on the receiver properties, which performs mode-selective QFC of the carrier frequency of the target mode ($\omega_{\mathrm{r}} = \omega_{\mathrm{s}} + \omega_{\mathrm{p}}$, where r is the upconverted light) [46, 68]. QFC is a process where the carrier frequency of the photon is translated without disturbing its quantum state; it is the quantum analog to SFG for classical waveforms. The receiver also has the advantage that the upconverted light is in the near visible spectral range, which can then be detected by a relatively low-cost and efficient silicon-based single-photon detector (SPD).

Experimentally, the upconversion is performed in a periodically-poled potassium titanyl phosphate (PPKTP)[69] or reverse proton exchange patterned LN WG [70, 71] on which the signal modes and the pump is incident. Various schemes for the layout of WG and pumps have been studied as shown in Fig. 3.1.1 [50], but the core functionality is the same. With a large material $\chi^{(2)}$ and tight mode confinement compared to bulk crystals, the WG at the center of the experiment has a high effective nonlinearity. Ridge-loaded or patterned LN on-chip WGs promise even higher efficiencies and even compact footprints, not to mention integration with other optical elements [72, 23, 73]. Our simulation outlined here applies to any $\chi^{(2)}$

system.

In order to ensure phase-matching, our device needs to be poled as discussed in subsection 2.2.2. This allows us to operate with a strong classical pump and signal in the telecom C-band with a sum-frequency below 800 nm for only a $2/\pi$ reduction in the optical nonlinearity. Finally, because we aim for telecom signals and pumps, our input beams can leverage fiber optics for transmission and readily available filters and amplifiers for pump preparation.

We need to tailor the temporal shape of our pump waveform for signal mode selection. We accomplish this experimentally by manipulating the optical waveform in the frequency-domain by cascading a radio frequency (RF)-driven phase and amplitude modulator-based frequency-comb source [74, 75] with an optical arbitrary waveform generator (OAWG) which modulates the phase and amplitude of each comb line independently [76]. This gives us control of the pump pulse up to the bandwidth limited by the RF comb which performs the desired operation efficiently with minimal cross-talk [76, 77, 78]. Finally, a erbium-doped fiber amplifier (EDFA) amplifies the resulting pump pulses to the required power level necessary for the conversion process.

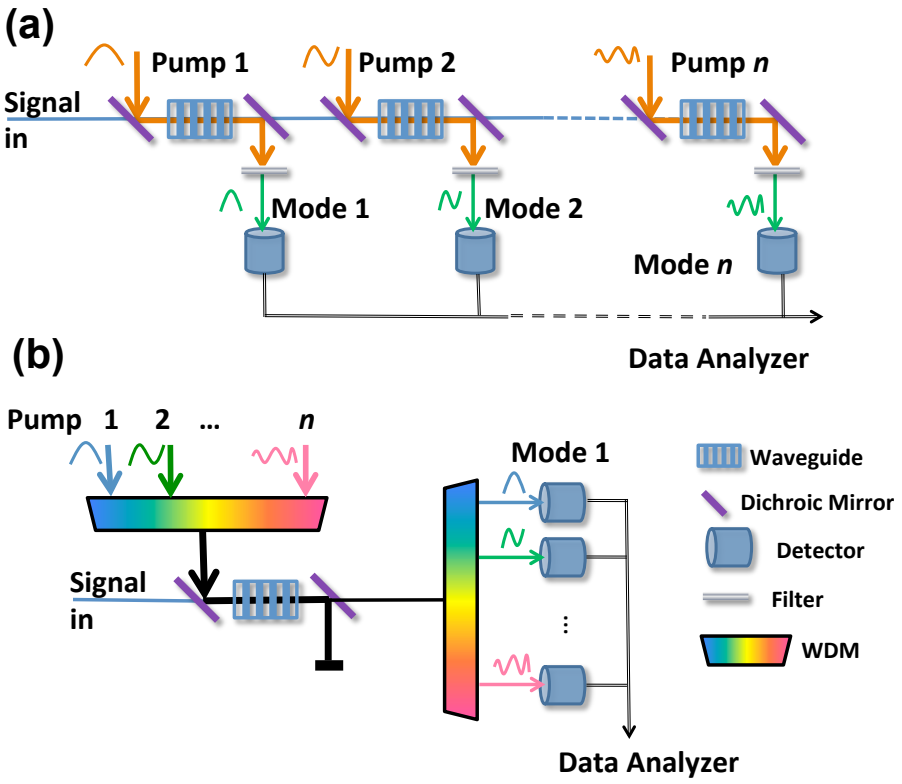

Figure 3.1.1: Two different schemes for the experimental implementation of the receiver. Both share pumps generated via a OAWG which up-converts an individual mode of the signal. (a) is a sequential scheme, which would require multiple waveguides for the signal to pass through. (b) is the parallel scheme, where one WG with n PM peaks can upconvert n modes of a signal into n different frequencies. Simulations for both schemes are discussed in this chapter.

We are interested in simulating the waveguide interaction in order to iteratively optimize the shape of of the mode-selective pumps. Our comb-source bandwidth is $B = n \times f_{\text{comb}}$. Experimentally, our modulator driving frequency and therefore spectral line spacing is $f_{\text{comb}} = 20\,\text{GHz}$, while we are limited to $n = 17$ comb lines, for a total bandwidth of $B = 340\,\text{GHz}$. However, larger bandwidths are accessible and some simulation work will reflect this as pump bandwidth is a fundamental constraint on the system. Another is the parameters of the waveguide in terms of

its dispersion but also its fabrication. We also address the problem of WG width variations which perturb the waveguide dispersion through a statistical model in Appendix B.

3.2 Simulation Overview

The simulation effort focuses mainly on the WG nonlinear optical interaction central to the receiver. Our goal is to select out via frequency upconversion only a single temporal mode of the signal set via pump shaping. In order to solve this inverse-design problem, we have two numerical components; the numerical SFG solver, and the optimization routine which uses this solver in order to design the pump shape.

Subsection 3.2.1 covers solution of the nonlinear equations of motion, while 3.2.2 discusses the optimization routine to determine pump waveforms. Appendix A contains the full MATLAB code and some notes on its performance.

3.2.1 Propagation Solver

To quantify the performance of our receiver, we need to simulate the efficiency of upconverting a given signal mode from a temporal mode set based on a pump waveform in a $\chi^{(2)}$ WG. We use the split-step Fourier method [1] to solve the equations of motion because of its proven efficiency compared to finite-difference methods (FDMs) . The algorithm relies on very efficient, parallelized, fast Fourier transform (FFT) algorithms. We use Matlab's built-in implementation of the FFTW library (see Appendix A.3 for more details).

In this simulation, we simplify the equations of motion by assuming that the

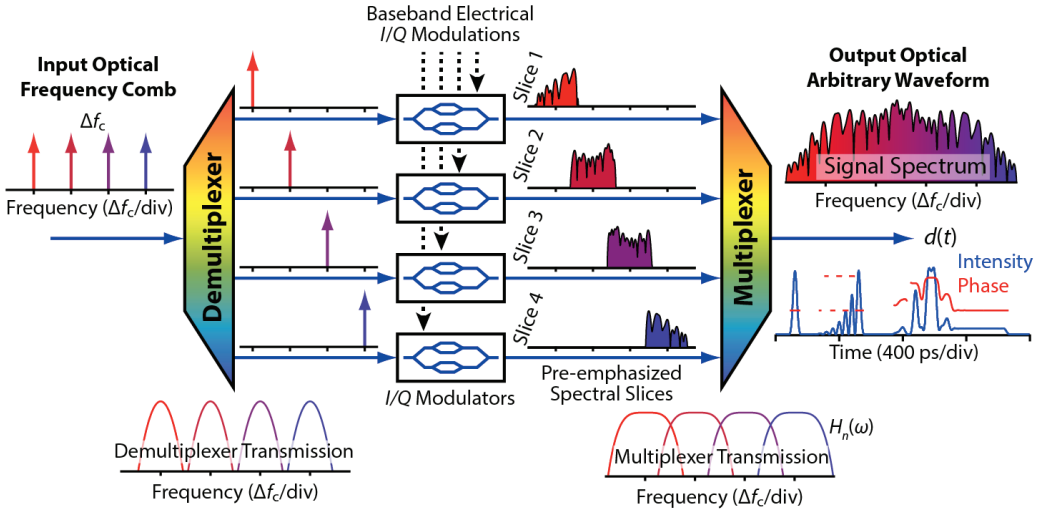

Figure 3.2.1: Schematic of the OAWG device. A frequency comb is demultiplexed. Each individual line is modulated in both amplitude and phase. The output waveform is generated after the modified lines are multiplexed together.

waveguide is single-mode for all wavelengths of interest. We also assume that the group-velocity mismatch between the upconverted light and the signal/pump pair is the only significant form of chromatic dispersion . This naturally implies that the dispersion of each of the three pulses is negligible over the frequency span of the pulse. However, additional dispersion terms can be added if the process under investigation warrants it. The equations of motion for the signal and idler in the undepleted pump regime are:

$$\left(\frac{\partial}{\partial z}+\beta_r\frac{\partial}{\partial t}\right)A_r^i(z,t)=i\gamma A_p(t-\beta_p z)A_s^i(z,t), \tag{3.2.1}$$

$$\left(\frac{\partial}{\partial z}+\beta_s\frac{\partial}{\partial t}\right)A_s^i(z,t)=i\gamma A_p^*(t-\beta_p z)A_r^i(z,t), \tag{3.2.2}$$

where $A_p(t)$ represents the pump amplitude at frequency ω_p, while A_r^i and A_s^i are the amplitudes of the upconverted and signal light for temporal mode i, respectively [62, 64]. $\beta_i, i \in \{r,s,p\}$ is the inverse of the group velocity for each of the three

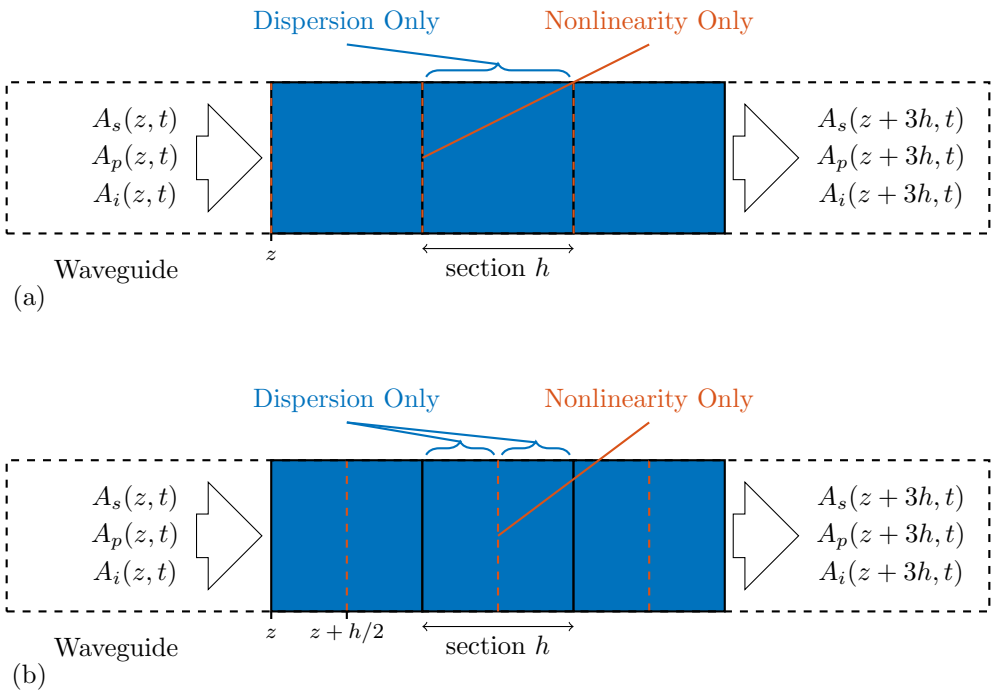

Figure 3.2.2: A split-step Fourier solver numerically solves for the interaction of the 3 optical waves in the waveguide. The device is divided into N segments of length h. (a) shows the standard split-step Fourier method, while (b) shows the symmetric version.

waves. We operate under the condition that $\beta_r \neq \beta_s = \beta_p$, as stated above. γ depends explicitly on the optical nonlinearity of the WG and the overlap of the spacial modes of the three electric fields in the device.

The split-step Fourier method relies on the approximation that dispersion terms and nonlinear terms of the equations can be treated independently. Re-writing the NLS as

$$\frac{\partial A}{\partial z} = (\hat{D} + \hat{N})A, \tag{3.2.3}$$

where $\hat{D}$ is the differential operator that accounts for dispersion and loss, while $\hat{N}$

is responsible for the nonlinear interaction in the medium. While in general both operators act together over the length of the WG, a good approximation can be made by dividing the WG (length l_0) into N parts and assuming each operator acts independently over the a small distance $h = l_0/N$. Numerically, the step from position z to $z + h$ can be written as:

$$A_{z+h}(t) \approx e^{h\hat{D}} e^{h\hat{N}} A_z(t), \tag{3.2.4}$$

$$\approx e^{h\hat{D}} A'_z(t). \tag{3.2.5}$$

By replacing the operator $\partial/\partial t$ with $-i\omega$, $\hat{D}$ can be evaluated exactly in the Fourier domain via:

$$e^{h\hat{D}} A'_z(t) = F^{-1}\left[e^{h\hat{D}(-i\omega)} F[A'_z(t)]\right], \tag{3.2.6}$$

where F denotes the FFT. Figure 3.2.2 shows a schematic of the simulation.

An improved version, the symmetrized split-step Fourier method, reduces the error of the approximation to third-order in the step size h. This method estimates the effect of the optical nonlinearity in the middle of the segment of length h, instead of at the start in the method outlined above. Finally, we note that the code has been extended to allow arbitrary QPM gratings and multiple pump and signal waveforms. This ability allows us to study both schemes shown in Figure 3.1.1.

3.2.2 Optimizer

In order to optimize the performance of the receiver, distinct pump waveforms are needed for each operation. We optimize the amplitude and phase of the individual comb lines that constitute the pump shape via a random walk method [79].

The iterative method works by taking the initial state of the comb lines and

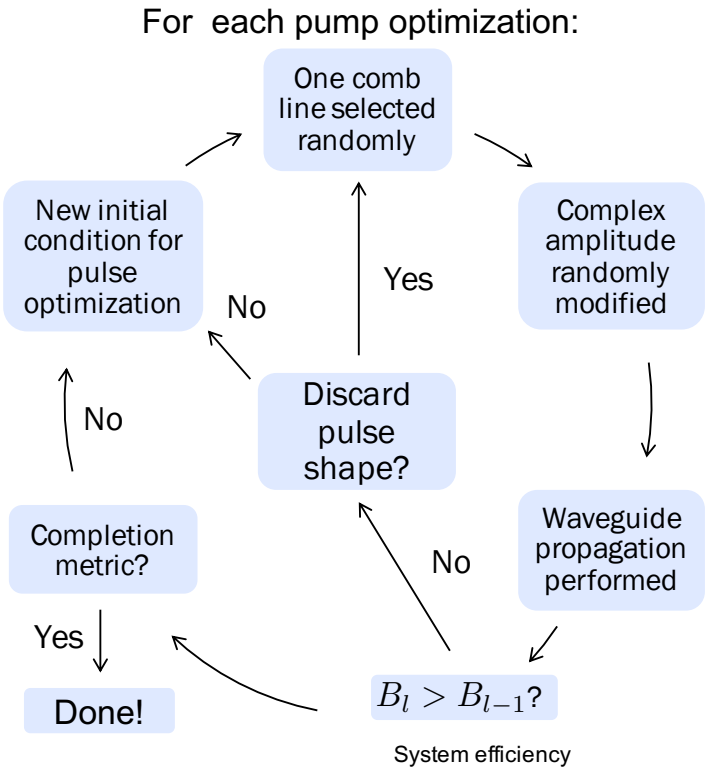

Figure 3.2.3: The flow of the optimizer routine for system efficiency. One lap of the above loop represents one iteration of the solver. l represents the current iteration index, while B_l is the metric used to evaluate performance, as described in subsection 3.3.1.

randomly tuning them. We randomly select a comb line then randomly modulate both its amplitude and phase individually. This new state of comb lines corresponds to a pump which is propagated through the WG via the solver described in the subsection above. Performance of the new pump is checked via a metric against the previous solution. If the new pump performs better, it is then used as the initial condition for the next iteration of the loop. One iteration is shown in Fig. 3.2.3.

A conditional statement implemented in the solver allows an iteration to, in effect, take a step backwards. This step accepts a pump with lower performance than

the previous iteration with a probability given by one minus the ratio of current and previous performance. With this step, the optimization routine can avoid settling in a local minimum of the optimization problem.

The optimization adjusts the amplitude and phase of each line of an arbitrary comb source in order to tailor the pump shape. The comb lines are related from one iteration to the next by

$$C_l^i = C_{l-1}^i \left(1 + \delta_a \mathcal{R}_a e^{i(2\pi\delta_\phi)\mathcal{R}_\phi}\right), \tag{3.2.7}$$

where C_l^i is the complex amplitude of the i-th comb line at the l-th iteration of the optimization loop. δ_a (δ_ϕ) is the tuning parameter representing maximum possible variation of the amplitude (phase) while $\mathcal{R}_i$ is an independent random number uniformly distributed between $-1/2$ and $1/2$.

The initial condition for the pump shape is based on the mode that it will up-convert. This waveform is superimposed with the shape generated by a comb source with equal amplitude in each line. Because each comb line has a non-zero amplitude compared, random modulations of any line will have an effect on the performance of the receiver. An initial condition based on only a subset of available comb lines will be limited to those lines because of the way amplitudes are updated. Figure 3.2.4 contrasts a typical signal mode with the initial condition for the optimization for it's pump waveform.

3.2.3 Quasi-Phase Matching Grating and Nonlinearity

The solver supports arbitrary QPM gratings and optical nonlinearity. While a traditional square pattern is efficient, as seen in Section 2.2.2, other distributions can

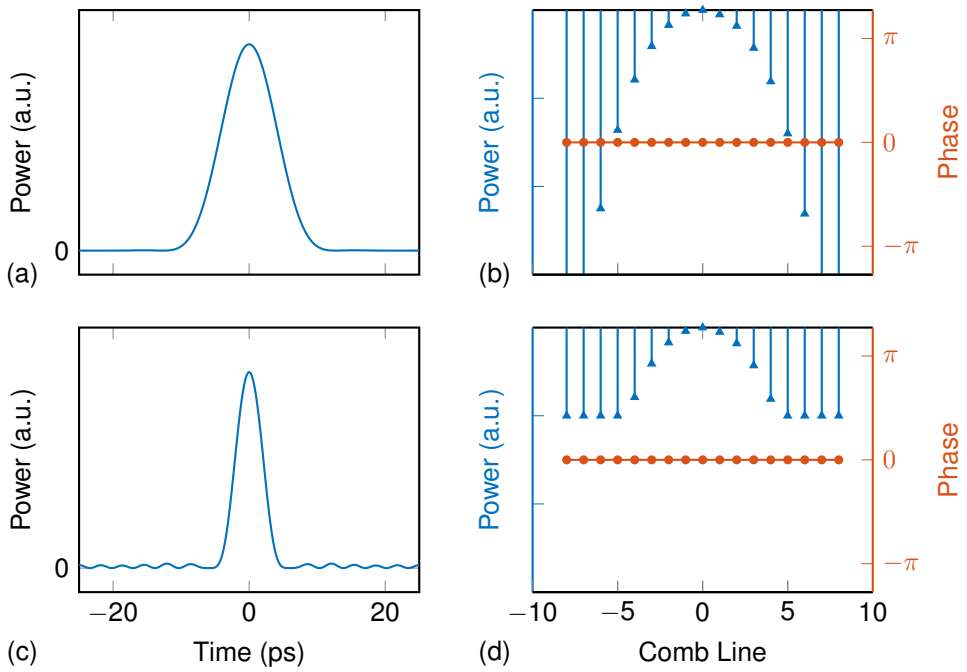

Figure 3.2.4: The pump initial condition is a combination of the profile of the target signal mode combined with a flat spectrum. The temporal, (a), and spectral, (b), profile of the target signal is shown with the corresponding initial condition for the pump temporal, (c), and spectral, (d), waveform

be advantageous. Chirped gratings reduce undesirable effects from other nonlinear interactions due to the $\mathrm{sinc}(x)^2$ phase-matching spectrum. The ability to simulate waveguides with multiple PM peak waveguides is leveraged in Section 3.6. Changing the nonlinearity scales the pump amplitudes uniformly so it's exact input value is not relevant to us.

3.3 Simulation Results

Here we show the results of simulation work for mode-selective upconversion. We simulate the operation of our receiver design on an example quantum signal mode set which can be generated with a phase-matched SPDC source driven by a 15-

ps duration pump pulse with fifth-order super-Gaussian spectral shape. Using the optimization routine outlined above and the phase-matching information of our waveguide, we generate optimized pumps for mode-selective QFC.

3.3.1 Performance Metrics

The performance of the receiver comes down to conversion efficiency. Converting the modes we need to measure without converting those we do not need. We denote conversion efficiency as the ratio $\eta_{(i,j)}$, which is the ratio of power of light upconverted by pump j from signal mode i over the input signal power in mode i in the classic optical wave case. In the quantum regime, this efficiency represents the probability of upconverting a photon that is in mode i by pump mode j.

In order to understand the holistic performance of the receiver in presence of many signal modes, three new metrics are considered:

$$S_k = \frac{\eta_{(k,k)}}{\sum_{i=1}^{n} \eta_{(i,k)}}, \tag{3.3.1}$$

$$B_k = \eta_{(k,k)} \times S_k = \frac{\eta_{(k,k)}^2}{\sum_{i=1}^{n} \eta_{(i,k)}}, \tag{3.3.2}$$

$$D = \sqrt{\sum_{i=1}^{n}\sum_{j=1}^{n} \left(\eta_{(i,j)} - \eta_{(i,j)}^T\right)^2}. \tag{3.3.3}$$

S_k is the system selectivity. It measures the ability of the receiver to select one and only one mode, k. The sum over η is over the total number of modes generated by the entanglement source. $\eta_{(i,j)}^T$ are the target efficiencies, or goal of the final result. B_k extends this measure into one value that attempts to characterize the overall system efficiency by combining the system selectivity with the efficiency of converting the mode of interest. A high selectivity but low system efficiency describes a device that

only selects the correct mode with high effective loss. Finally, we use D to represent the geometrical distance between the current set of conversion efficiencies and the target performance. For example, the ideal receiver would satisfy target efficiencies

$$\eta^T = \begin{bmatrix} 1 & 0 & \cdots & 0 \\ 0 & 1 & \cdots & 0 \\ \vdots & \vdots & \ddots & \vdots \\ 0 & 0 & \cdots & 1 \end{bmatrix}, \tag{3.3.4}$$

where η^T is square of size n and $\sum_{k=1}^{n} S_k = n$, $\sum_{k=1}^{n} B_k = n$, $D = 0$. This device would convert the target mode with 100% efficiency and only this target mode across the whole temporal overlapping signal set.

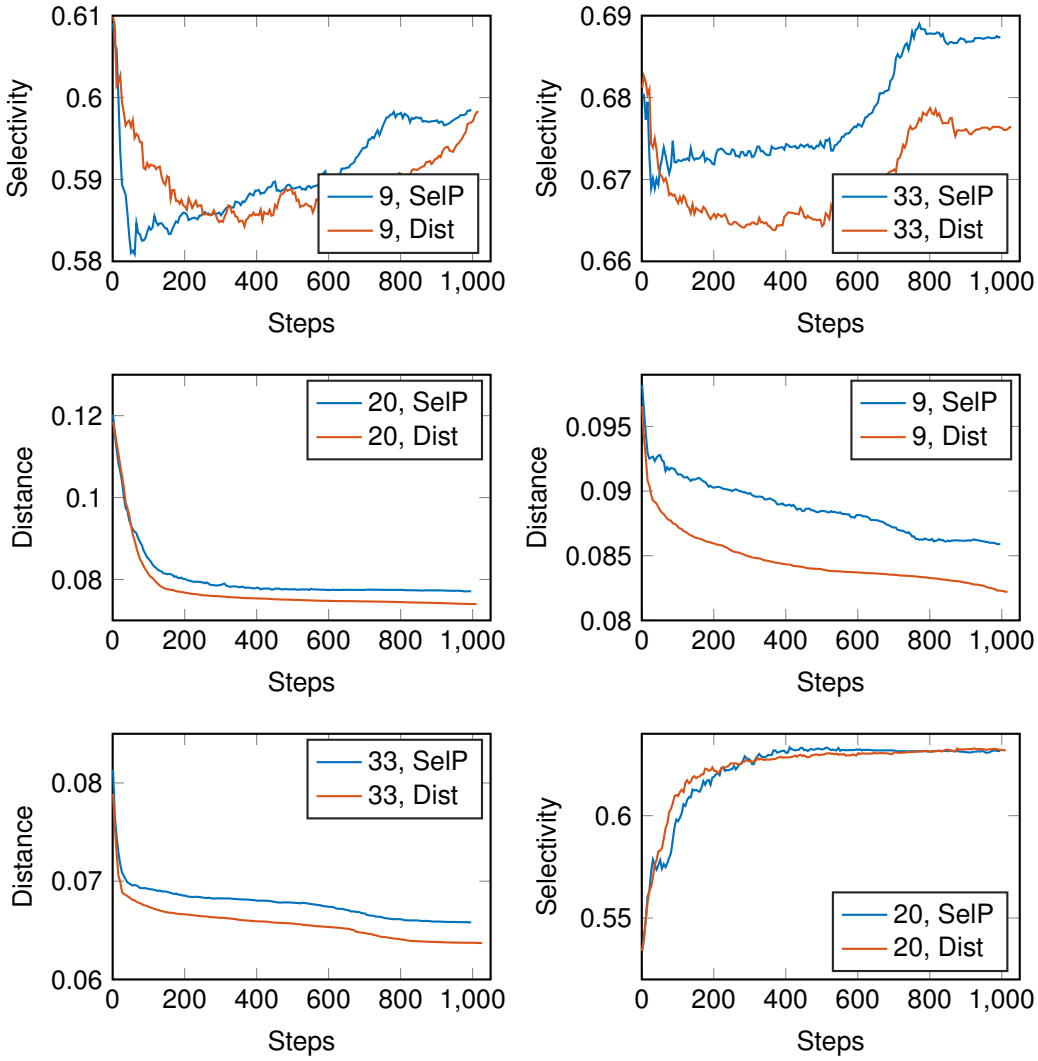

Figure 3.3.1: In these three test cases, the results of optimizations based on distance (D) and weighted selectivity (B) are shown.

We typically optimize to minimize distance, as this one parameter summarizes the performance of receiver, as seen in Fig. 3.3.1. Generally the other metrics trend with D. However, we can modify the target efficiency matrix to tune the goal of the simulation.

In the (classical) validation of the receiver, individual signal modes can be

prepared by an OAWG in the same way pump pulses are generated, allowing us to directly measure each conversion efficiency independently.

3.3.2 Selectivity Results

The first simulation of the receiver is also the most basic. We show the ability of our method to mode-select via QFC a single or a superposition of input modes. For our example, we consider the Schmidt modes of a two-photon state generated via SPDC driven by a 15-ps duration, fifth-order super-Gaussian pump pulse [80]. The signal/idler spectral windows are defined by rectangular 5.4-nm filters.

We numerically optimize pump pulse shapes for the photon modes described above for a commercial 6-cm long WG with a inverse group velocity difference of 2.54 ps/cm and negligible group velocity dispersion. Fig. 3.3.2, the first, fifth, and tenth mode signal modes (a) are plotted and their corresponding pumps (b). The desired phase and relative amplitude of the OAWG manipulated comb lines for the first and fifth mode is shown. Extending this further, the conversion efficiency of all 10 modes for each of the 10 pumps is shown in Fig. 3.3.3. Each mode is upconverted with over 90% efficiency, however cross-talk increases (selectivity decreases) as the mode number increase.

In order to show the flexibility needed for operation of this receiver in a quantum communication setting, it is important to show that performance is maintained across arbitrary coherent superpositions of these modes. We consider the superposition $\psi_{\pm} = 1/\sqrt{2}(\psi_1 \pm \psi_5)$ as an example. The performance of the receiver for modes re-optimized for this superposition basis is shown in Fig. 3.3.4. The performance is nearly identical to that of the previous Schmidt basis. We note that the pump amplitudes and phase of the newly optimized pumps are significantly different than

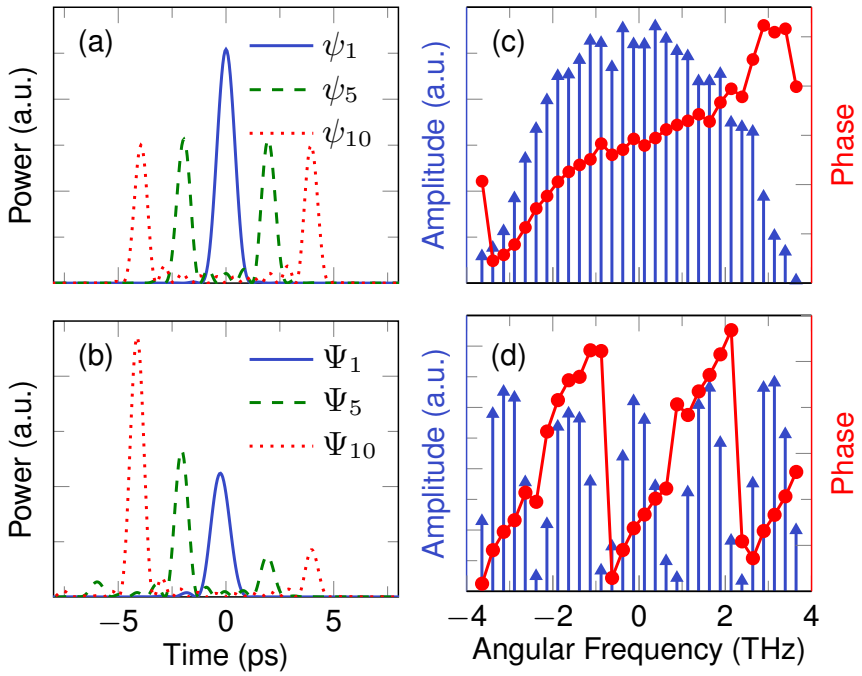

Figure 3.3.2: (a) is the first, fifth, and tenth signal modes. (b) is the corresponding simulated pump modes generated via OAWG in order to maximize selectivity of the receiver. (c) and (d) are the amplitude and phase of each individual comb line for the first (c) and fifth (d) pump waveform. The pump amplitudes here are arbitrary, however for a typical LN or PPKTP WG, the peak power of the pump pulses is on the order of watts.

a simple superposition of the non-superposition pump shapes.

In the mode-resolved photon counting scheme shown in 3.1.1(a), after passing through a stage of receiver, the mode profiles of the upconverted photons may be modified. However, numerical simulations show that the modes maintain their orthogonality. Fig. 3.3.5 shows that receiver can overcome this distortion also if we optimize pump shapes at each stage to match the evolving signal set.

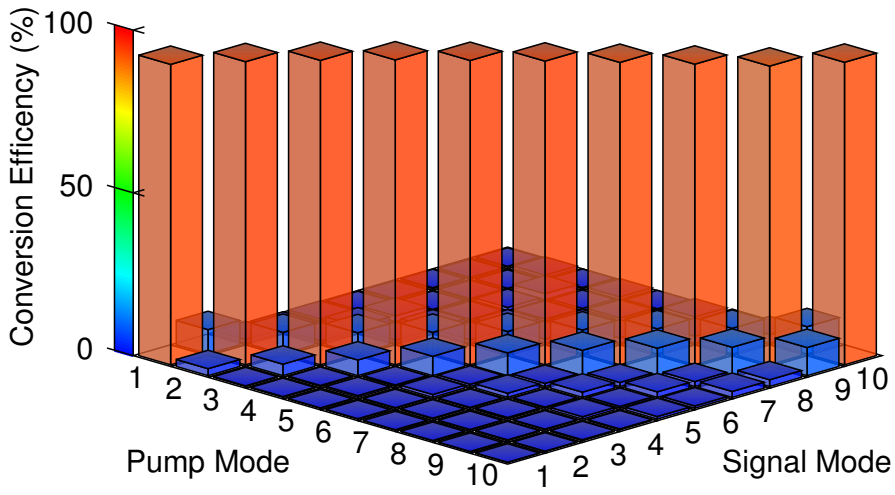

Figure 3.3.3: Conversion efficiency matrix for ten signal modes. The n-th pump mode is optimized to maximize selectivity of the n-th signal mode. Off-axis terms represent cross-talk due to imperfect selectivity.

3.4 Waveguide Width Variations

It has been shown that variations in WG width due to fabrication inconsistencies are a leading cause to distortions in the shape of the phase-matching bandwidth of a WG [48]. Because our devices suffer from this distortion measured via SHG with a tunable wavelength pump, we modified the numerical solver discussed in subsection 3.2.1. By including a position-dependent phase-mismatch, $\Delta k \rightarrow \Delta k(z)$, we can simulate the effects that these variations have on the performance of our receiver.

Because we cannot make the direct measurement of the complex transfer function (CTF) of our device (as done in [48]), we instead built a statistical model to simulate these effects. Comparing the spectral PM dependence calculated from the model to the measured dependence of the conversion efficiency of our WG for SFG allows us to select a small range of CTFs that are representative of the physical de-

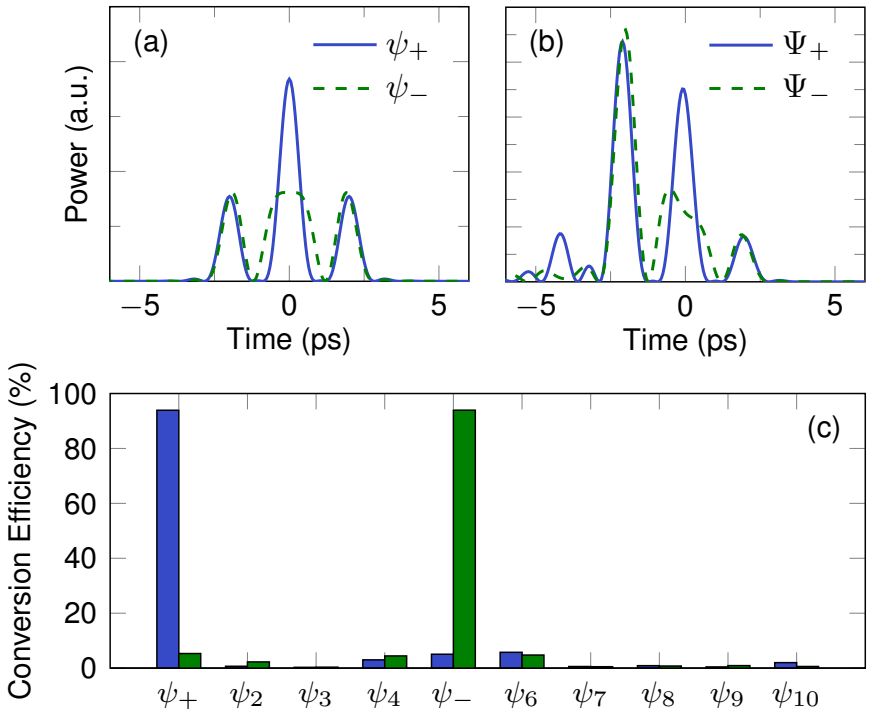

Figure 3.3.4: (a) The signal modes, $\psi_\pm = 1/\sqrt{2}(\psi_1 \pm \psi_5)$. (b) The corresponding pump modes for $\psi_\pm$ are $\Psi_\pm$. These pump modes are not simple superpositions of the non-rotated basis pumps. (c) The conversion efficiency performance in the 'superposition' basis is nearly identical to that in the original basis.

vice used in the experiments. Measuring the phase relationship between the input and output light would give us an exact model to feed into the simulation. Appendix B describes the details of this statistical model.

3.4.1 Width Variation Compensation

The waveguides used in these experiments were fabricated by Martin M. Fejer's group from Stanford University, who are world leaders in poling and chip fabrication. Despite this, our devices suffer from non-ideal PM curves, as shown in blue in Figure. 3.4.1. Because we do not have a sum-frequency generation cross-frequency resolved

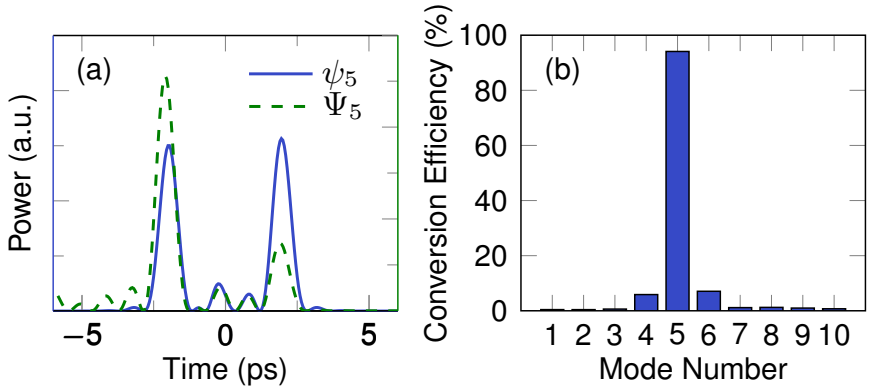

Figure 3.3.5: (a) The fifth signal mode after one stage, ψ_5, and the corresponding pump pulse, Ψ_5. The amplitude is arbitrary. (b) A plot of $\eta_{(i,5)}$. The conversion efficiency is roughly 10% for mode four and six.

optical grating to directly measure the phase of the WGs SHG light [48], we built a model which estimates the CTF and comparing how well it matches the measured response.

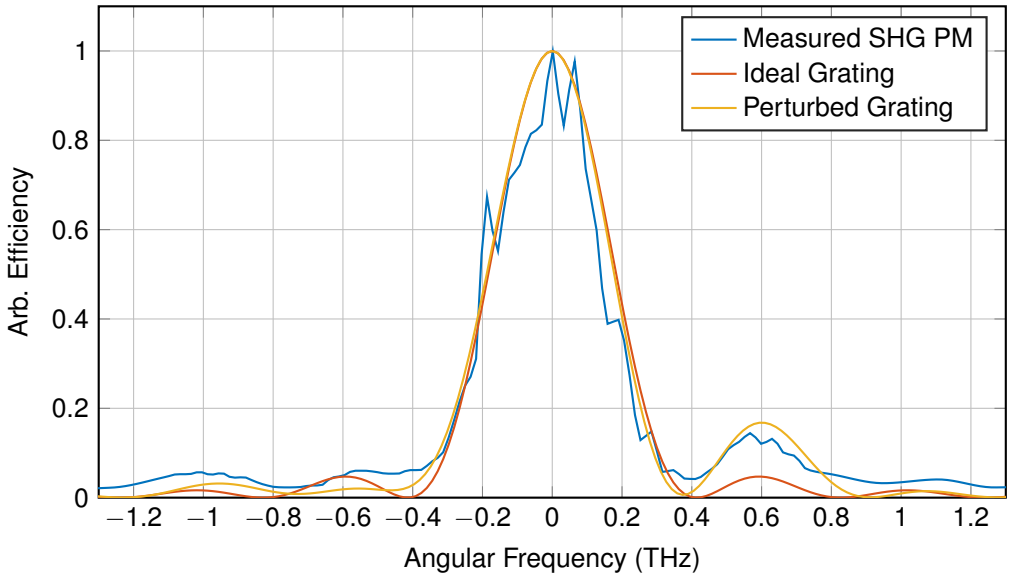

Figure 3.4.1: The measured PM curve of the actual waveguide used in the experiment is shown in blue. The red curve shows an ideal curve, proportional to $\text{sinc}^2(\omega)$, for a square QPM grating. The yellow curve represents a numerical estimate of the measured curve based on varying the width of the waveguide as a function of its position.

The simulation to generate candidate CTFs starts by estimating the correlation length and size of width variations in the waveguide. These width variations lead to local differences in group index, n_g, which distort the grating. Because the devices are 46 mm long, we randomly poll either 23 or 46 times a normal distribution centered around the expected Δk with various standard deviations. From this the CTF can be calculated. See Appendix B for the details of the simulation. In Figure 3.4.1, the best estimate, calculated via sum of least squares from 1000 trials is shown in yellow.

Ultimately, we are interested in the how these PM distortions affect the mode-selective receiver. Because the distortion is relatively small, our simulations show that the optimization algorithm can compensate to some degree and recover some

of the unperturbed or ideal grating performance. Figure 3.4.2 shows an example of the simulation results. Here a pump optimized for signal mode 3 is used. When the exact same pump mode is used with the perturbed grating, the conversion efficiency of the target mode drops but others increase, which constitutes a drop in selectivity. After running the optimization algorithm with the perturbed grating, performance recovers to roughly half way between the ideal case and using the ideal pumps with the perturbed grating. Expanding this to other pumps in the mode set, Figure. 3.4.3 shows that re-optimization can compensate for a perturbed grating to recover selectivity and efficiency for each pump simulated.

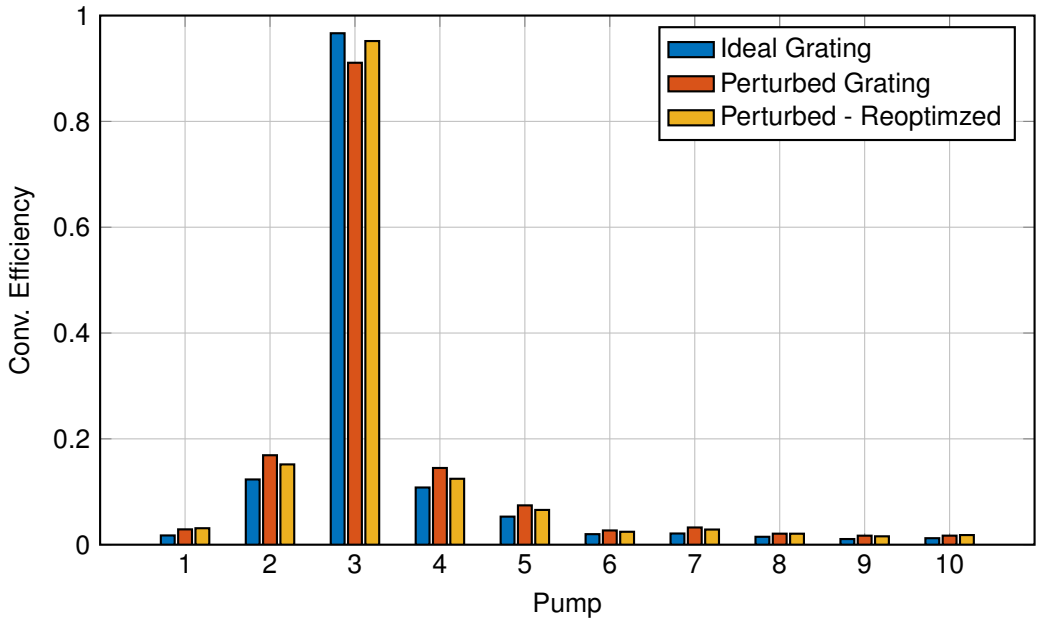

Figure 3.4.2: We compare the results between the ideal and perturbed gratings for a pump optimized to upconvert mode 3 from a signal set. We compare the original pump shape, the original pump shape on the perturbed grating, and a re-optimized pump specifically for the perturbed grating. Conversion efficiency and selectivity increase after the re-optimization despite the non-ideal shape.

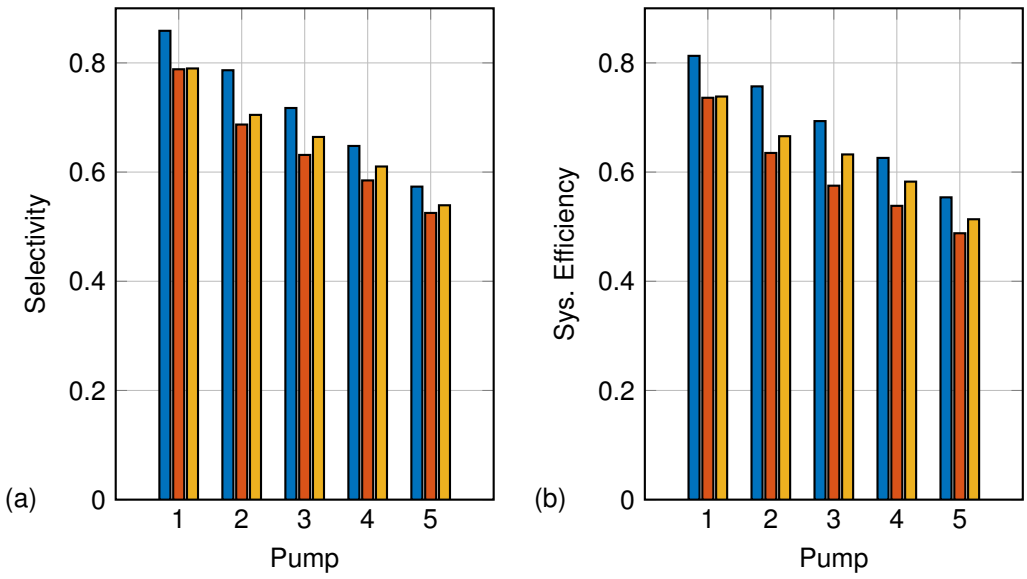

Figure 3.4.3: (a) shows the selectivity, S_k, and (b) shows the system efficiency, B_k. While Figure 3.4.2 looked at individual conversion efficiencies for a select pump on the sample signal mode set, this looks at any degradation caused by the perturbed grating on 5 pumps optimized to upconvert the first 5 signal modes. Colors represent the same grating as in the previous figure.

3.5 Dispersion Tolerance

In every simulation shown up to now, the signal source and receiver have been connected with a idealized link which causes no distortion of the signal waveforms. However, in any realistic communication system, optical fiber will be used which has non-negligible dispersion. During fiber transmission, even a small amount of residual dispersion (due to imperfect dispersion compensation, for example) in the fiber links can significantly disrupt the overlapping time-frequency modes and induce cross-talk between them, resulting in information error on the receiver end. Figure 3.5.1 shows the system under simulation.

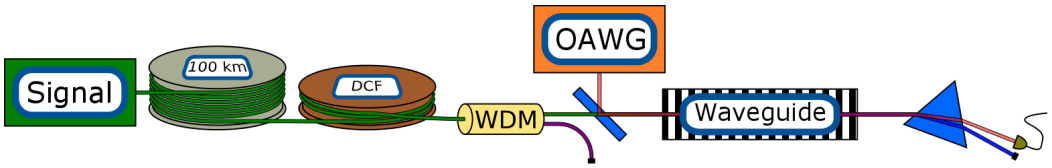

Figure 3.5.1: Schematic of the simulated system. 100 km of SMF is used to for the transmission fiber. DCF is added as part of the receiver system in order to compensate for the inherent dispersion in such a long transmission line.

3.5.1 Fiber Link

The fiber link consists of 100 km of transmission fiber, with loss and dispersion consistent with TrueWave Reduced-Slope fiber. After the fiber link, there is a spool of dispersion-compensating fiber (DCF) to reduce chromatic dispersion effects caused by the transmission fiber. However, there is a residual 2% slope mismatch between the transmission and compensation fibers which leads to 8 ps/nm of residual dispersion, typical of a real-world scenario. This residual dispersal dispersion is the cause of the pulse changes in Figure 3.5.2

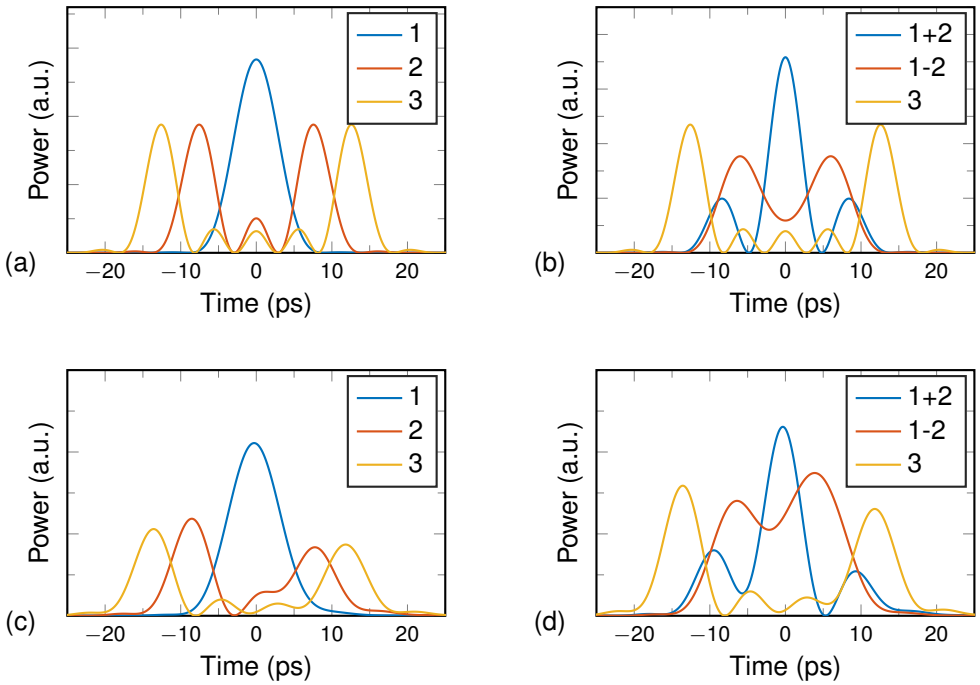

Figure 3.5.2: Three signal modes, and their superpositions are shown before (top row) and after (bottom row) transmission in the fiber link. Despite the presence of DCF, the final pulses are distorted.

3.5.2 Simulation Results

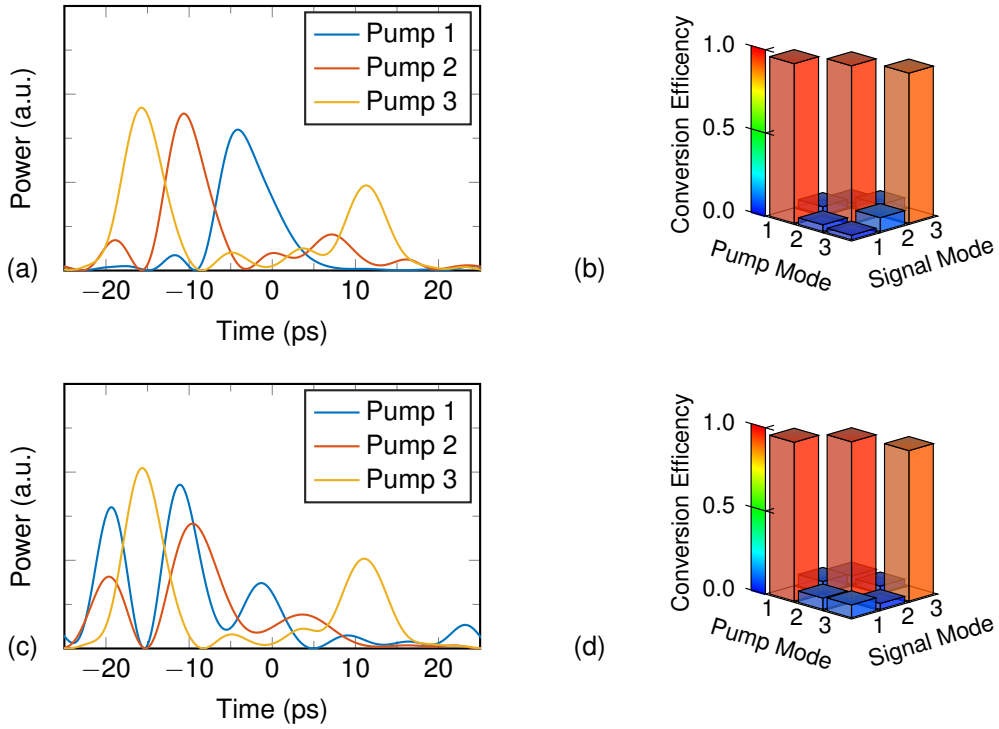

Figure 3.5.3: The pump mode shapes needed for the standard case, (a), and the superposition case, (c). (b) and (d) show the respective conversion efficiency matrix for the 3 pumps.

For practical considerations, consistent with our experimental implementations, we use an OAWG with 20 comb lines spaced at 10 GHz as the input to shape the pump waveforms. The QFC process occurs in a 8-cm-long periodically-poled lithium niobate (PPLN) waveguide with 3-ps/cm group-velocity difference between the pump and the up-converted (sum-frequency) light. As shown in Figure 3.5.3, high selectivity is possible despite the residual dispersion. The upconversion efficiency for the target signa mode is over 95% for each of the 3 cases shown, while selectivity is over 85%. Performance of the receiver is broadly similar for the superposition modes shown in Figure 3.5.2, which is crucial for quantum communications. Furthermore,

this result showcases the generality of our scheme for any basis of orthogonal temporal modes.

3.6 Multi Phase-Matched Waveguides

In order to implement the multiplexed scheme shown in Figure 3.1.1, we need a parallel QFC implementation [50, 16]. With each pump at a distinct central wavelength, λ_i, the WG needs to be poled in such a way that it has multiple QPM peaks. Each peak corresponds to a pump which corresponds to a signal mode which will be upconverted to a unique wavelength. The major advantage of the parallel vs sequential layout is that the former requires one WG, making it more compact and dramatically reducing the transmission loss of the quantum signal input. While loss scales linearly with the number of signal modes in the sequential case, it is constant in the parallel case. However, the requirements for poling are stringent and may introduce higher cross-talk (reduced selectivity) because of the nature of the phase-matching spectrum of the mutli-peaked WG, as shown in Figure 3.6.1.

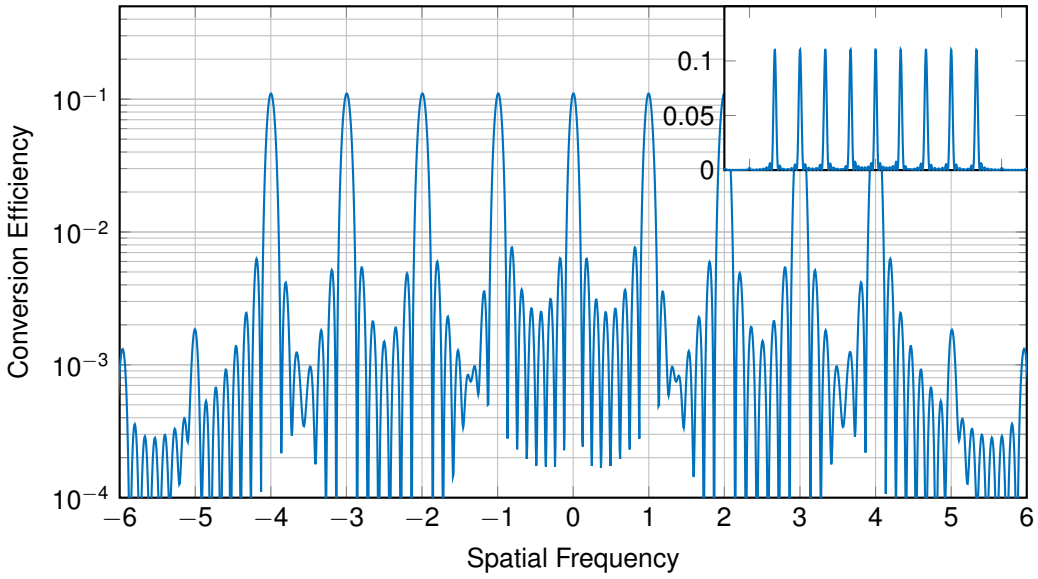

Figure 3.6.1: The x-axis of this plot is normalized to the wavelength of the fundamental grating, Λ_{ph}, so that the spatial frequency is $(\Delta\beta - K_{\text{QPM}})/(2\pi/\Lambda_{\text{ph}})$. For SHG with a pump in the telecom C-band in this waveguide, the peaks are roughly 2 nm apart in optical wavelength. Each peak has a sinc^2 shape. The inset shows the same grating with the y-axis on a linear scale.

3.6.1 Preliminary Results

Simple 2x2 simulation results, using a 20-GHz spaced 20-line comb are shown in Figure 3.6.2. In this case, the two adjacent PM peaks were used to see if cross-talk would increase. The conversion efficiency for the target signal mode was roughly 85%, while no cross-talk terms were greater than 10%. These results can be further improved by increasing the total bandwidth of the comb either by increasing it's spacing or number of comb lines [50].

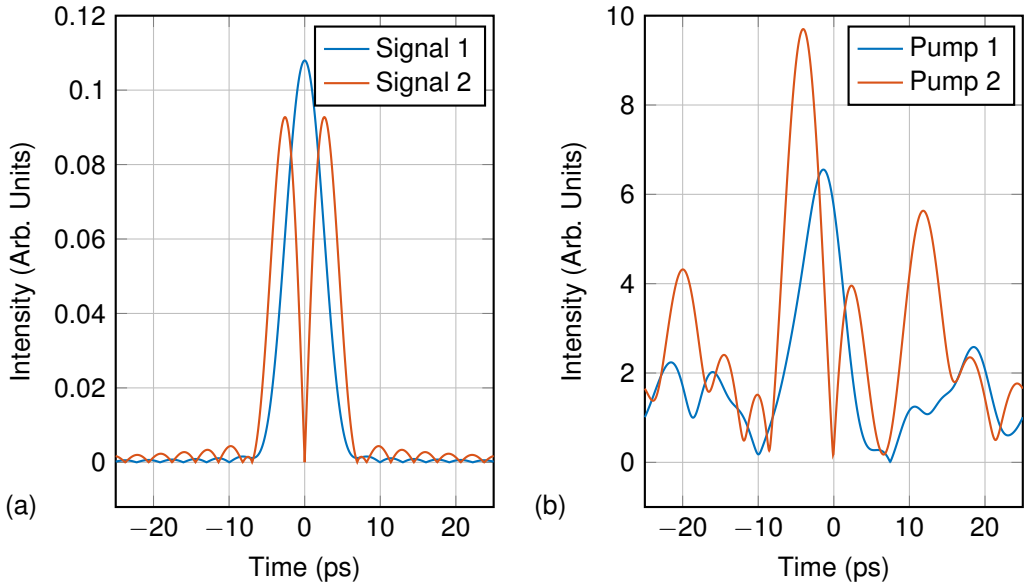

Figure 3.6.2: The signal and matched pump modes for the preliminary simulation.

3.6.2 Conversion Efficiency and Cross-Talk

Experimentally, our comb-source for this multi-peaked WG was initially limited to only 17 comb lines spaced 20-GHz apart. The results presented here show the simulated performance of the device in this configuration. However, we will also show that the system can benefit from increased optical pump bandwidth.

In the experiment, the signal modes are classical signals generated in the exact same way as the pumps, using an OAWG. The 4 signal modes are based on realistic modes that would be produced by a SPDC source but produced in this way to ease study of the system. Modes can be sent in as a complete set or individually, and we can measure the upconversion with a simple powermeter [62]. With these pre-determined signal modes as our target mode-set, we optimize the pump shapes using the simulation to estimate the performance of the device. Presented below are the results of this simulation work under the constraints of the experimental

setup.

Conversion efficiency and selectivity for the initial 17-line 4-by-4 system is shown in Figure. 3.6.3. After 200 iterations of the optimization algorithm, the selectivity and conversion efficiency start to plateau. Figure 3.6.5 shows that exactly, with a further 500 iterations providing no improvement in the key metrics. As another test of the waveforms, in Figure 3.6.4, we vary only the intensity of the pump, keeping its shape the same. We see that conversion efficiency and selectivity tend to both peak near 1, which is equal to the pump power generated by the optimization routine.

Another consideration is whether adjacent nonlinear processes (in spatial frequency) will have a higher cross-talk. Figure 3.6.6 shows that at least in an ideal situation, this is not the case. Optimization produces roughly the same performance for both modes whether the pumps are in adjacent spectral peaks (case 1) or at either end of the QPM spectrum (case 2).

Finally, as we saw in the 17-comb line case, the ultimate performance of our device is bandwidth limited. In Figure 3.6.7 we increase the bandwidth of our pump without increasing the number of parameters in our optimization by increasing the RF spacing of the lines. While a 160 GHz spacing supported by an RF comb is unrealistic, this spacing is easily accessible with a WGM resonator-based frequency combo or an RF-based device with a lower frequency but increased comb lines.

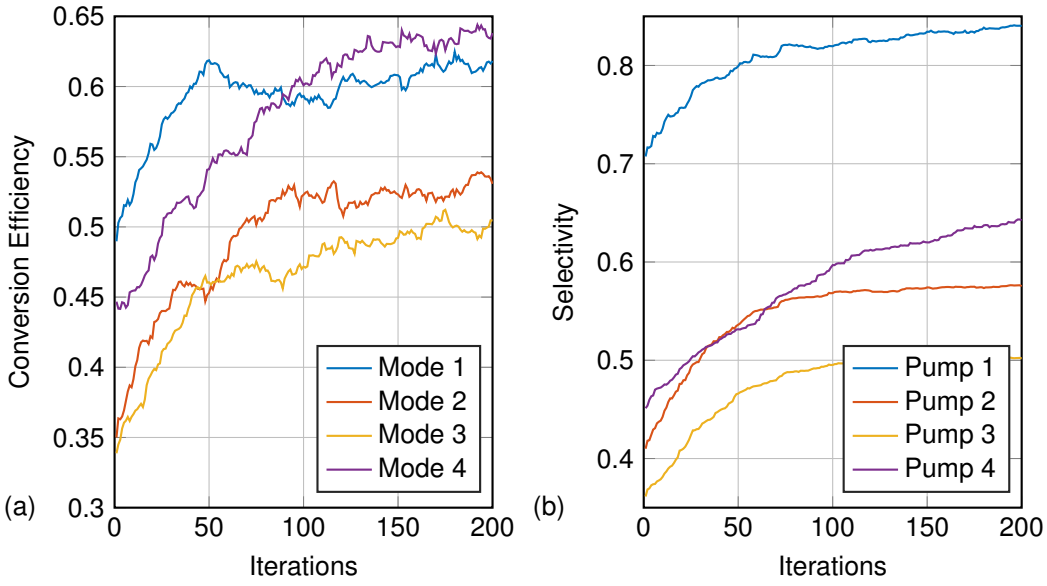

Figure 3.6.3: Conversion efficiency, (a), and selectivity, (b), for the 4-by-4 system simulated after 200 iterations of the optimization loop.

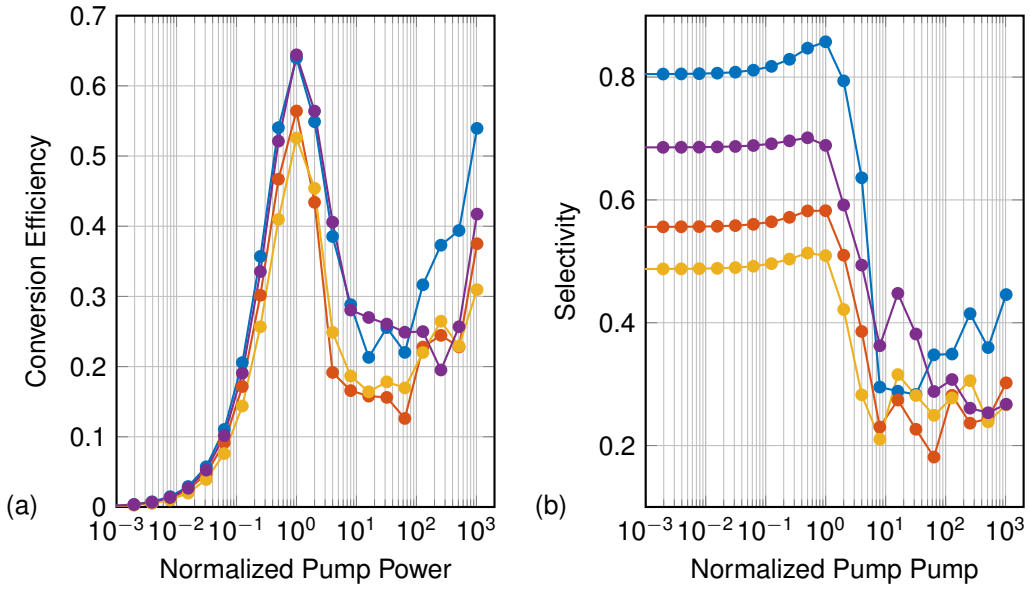

Figure 3.6.4: Power is normalized such that one is equal to the power of the optimized waveform. We vary only the intensity of the pump, not the waveform for this simulation.

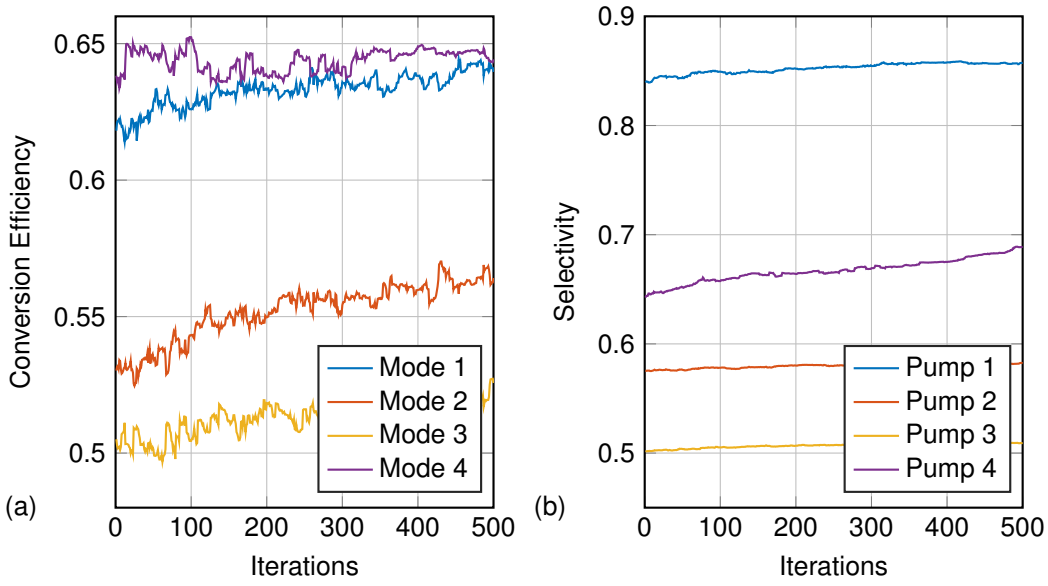

Figure 3.6.5: Running the optimization for another 500 iterations produces no significant increase in performance.

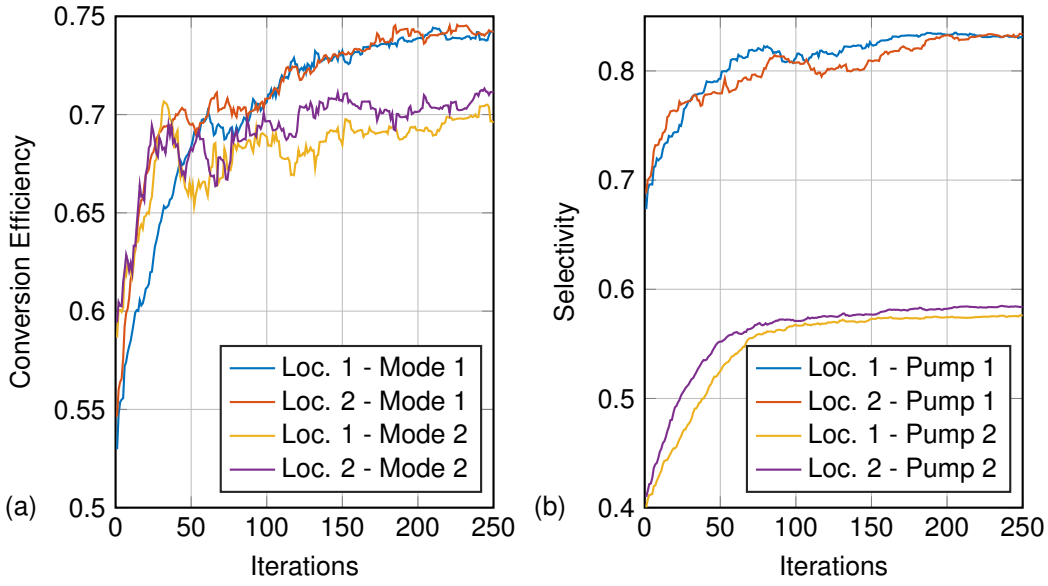

Figure 3.6.6: Simplifying the system to two pumps, we change the separation between adjacent QPM peaks in case 1 against farthest peaks. The results are nearly identical. Cross-talk due to the unique poling is negligible in this simulation.

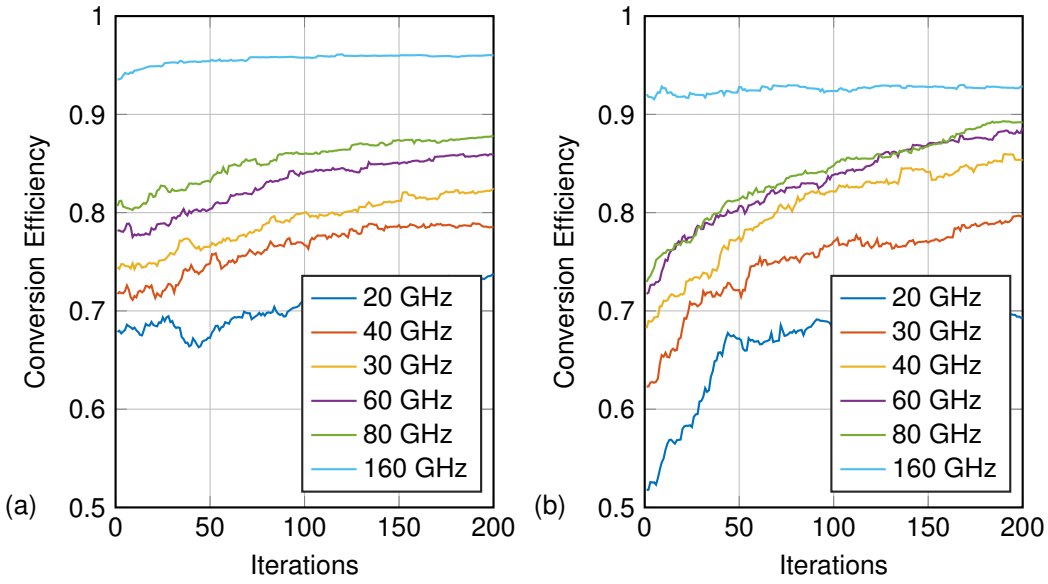

Figure 3.6.7: Increasing the spacing of the comb increases the bandwidth without an increase in the number of parameters that the optimizer needs to contend with. As an exercise, even unrealistically high RF frequencies are included because the total bandwidth may be realizable with a different comb-number vs comb-spacing tradeoff. (a) shows the conversion efficiency of pump 1, while (b) shows the same for pump 2.

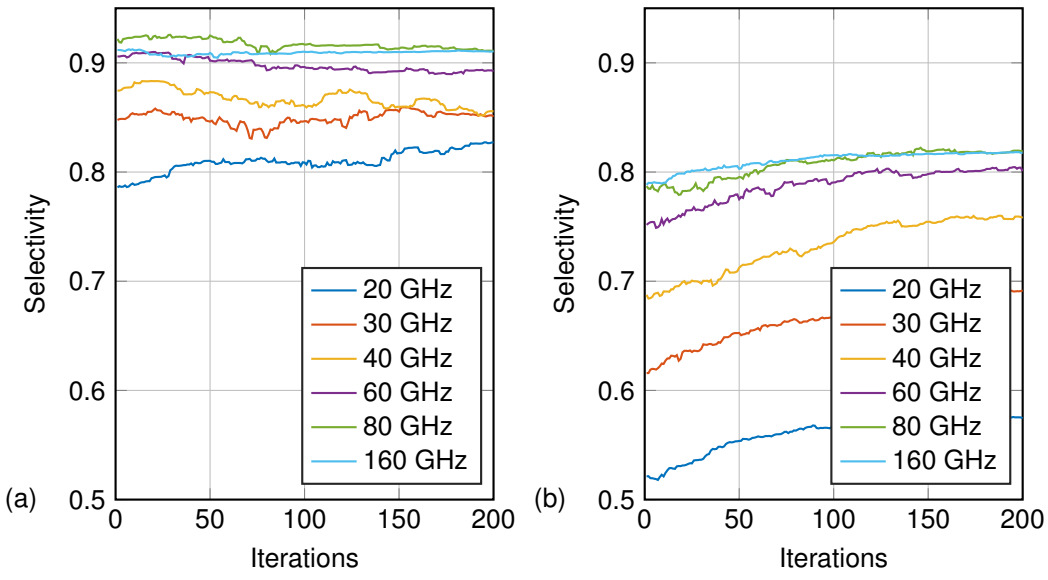

Figure 3.6.8: This is the selectivity complement to Figure 3.6.7.

4 Photon-Pair Generation Experiment

We have demonstrated a a:Si-H WG for photon-pair generation. The measured CAR is as high as 400 for multiple signal-idler channels. The multiple advantages of this material, as outlined earlier, are its very high optical nonlinearity, CMOS integrability, and very low TPA [31, 32, 33]. We harnessed these properties in the telecommunications C-band to show CAR performance at two different detunings (15 and 20 nm) at room temperature. Previous work in this material showed a much lower CAR due to higher linear loss and a lower nonlinear coefficient, γ [81].

Compact sources of photon pairs have been developed in c-Si WGs, however the practical performance of these devices is limited by strong TPA and free-carrier absorption (FCA) effects [28, 29]. The high deposition temperature required for c-Si chip integration is another disadvantage to this material because it complicates integration with other chip features such as electrical devices.

4.1 Device Details & Experimental Setup

The a:Si-H WG used in this experiment was fabricated by Mark Foster and Amy Foster's research groups in the electrical and computer engineering department at JHU. The experiment was carried out at Northwestern. The device is 8 mm long and

has inverse tapered edge couplers to reduce chip-to-fiber coupling loss. The cross-sectional geometry (215 nm by 500 nm) gives a group-velocity dispersion (GVD) of roughly 350 ps/(nm km) at the pump wavelength of 1555.8 nm which is chosen for efficient FWM. Using the cutback method on a device from the same batch, we estimate the loss to be $\approx$ 3.2 dB/cm, but it may be possible to reduce this to less than 1 dB/cm by using a different cladding material [82] or modifying the fabrication technique to reduce WG wall surface roughness[83]. By using a classical FWM measurement of conversion efficiency, we directly measured the γ of our device to be $1260\,\mathrm{W}^{-1}\mathrm{m}^{-1}$ which is an order of magnitude better than a typical c-Si WG (roughly five orders of magnitude than silica). Our collaborators have fabricated devices with $\gamma \approx 3000\,\mathrm{W}^{-1}\mathrm{m}^{-1}$ [31], which if it can be reliably combined with lower loss, will lead to a lower required pump power and increased photon-pair brightness.

The experimental setup is shown in 4.1.1. A mode-locked femotsecond laser (IMRA CX-20) with a repetition rate of 50 MHz is filtered via wavelength-division multiplexing (WDM) filters centered at 1555.8 nm with a non-Gaussian pass-bandwidth of roughly 1 nm. A combination fiber polarization controller (FPC) and fiber polarization beam splitter (FPBS) is used to control the output power of the laser. A second FPC is used in order to ensure correct polarization of the input pump because the designed geometry of the WG is tuned for TE-polarized FWM. To couple light into the chip, a standard lensed fiber is used, while the output coupling is done via a lens-collimator assembly that transmits the light from the chip into single-mode fiber (SMF). The polarizer inside the free-space output coupling removes any cross-polarized light. The fiber-to-fiber efficiency is roughly 8 dB, split roughly evenly between the input and output coupling. A free-space triple-pass grating filter (TGF) serves two functions. First, it isolates the pump by over 100

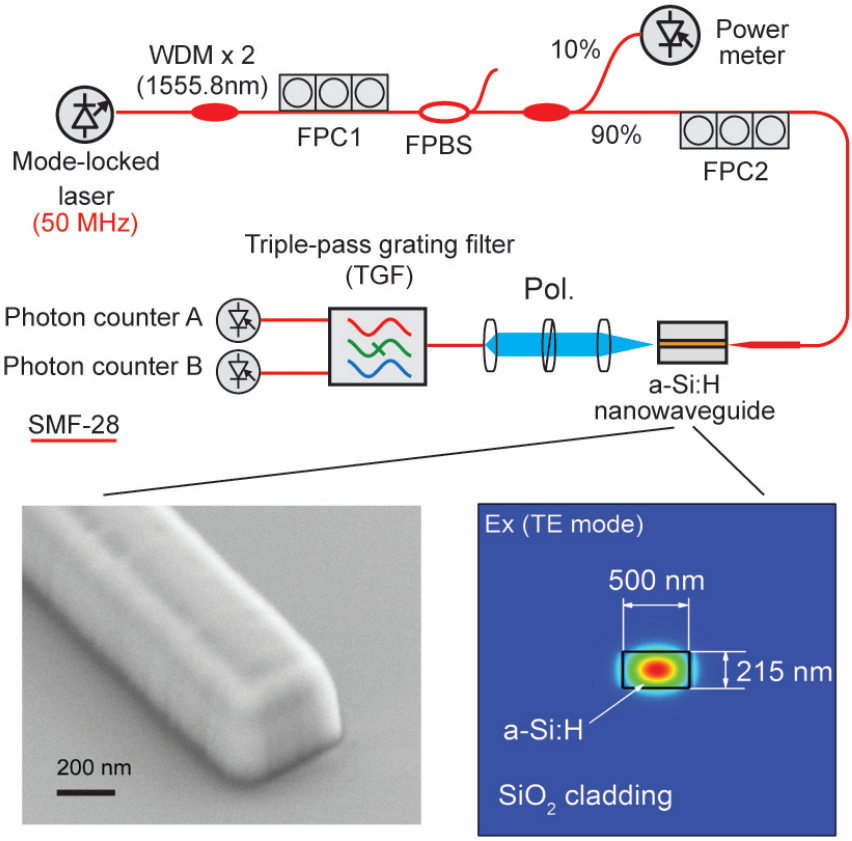

Figure 4.1.1: The experimental setup is shown above. Left inset: Scanning electron microscope image of WG. Right inset: The simulated electric field profile of the device for the TE polarization.

dB, which is key to the function of the InGaAs avalanche photodiode SPDs. Finally it defines a Gaussian-like bandwidth of roughly 0.65 nm for the signal/idler pair. The loss through the filter is 2.6 dB and can be manually tuned over a range of detunings.

4.2 Raman Measurements

The photon counts at two different pump-signal detunings, 15 and 20 nm were taken as the pump power was varied in order to characterize the Raman noise contribution to the photon-pair generation rate. In Fig. 4.2.1, the detection efficiency corrected single-photon counts are plotted as a function of input pump peak power for a detuning of 20 nm. The overall detection efficiency , $\approx 2.7\%$ for the Stokes (and $\approx 1.9\%$ for the anti-Stokes) channel, is due to the losses of the coupling system, filter setup, and sub-unity (near 15%) quantum detector efficiencies. Detector dark-counts were also subtracted from the signal counts [84], which for our InGaAS SPDs were greater than 5 kHz per detector channel.

In a low-conversion regime, $\gamma P_0 L \ll 1$, where P_0 is the instantaneous pump power and L is the interaction length of the WG, the Raman scattering contribution to the photon count is linearly dependent upon the pump power. However, the FWM photon generation rate is quadratic with pump power, which gives us a straightforward way to characterize these two distinct processes. We fit our data (as shown in Fig. 4.2.1) with

$$n_u = \Delta\nu_u \int \left(|\gamma P_0 L|^2 + P_0 L |g_r| N_u\right) \, d\tau, \tag{4.2.1}$$

where $u = s, a$ refers to the Stokes or anti-Stokes channels [45]. $\delta\nu_u$ is the filter bandwidth that defines the bandwidth of the channels (the bandwidth of the TGF). N_u is the phonon population given by the thermal distribution as shown:

$$N_a(\Omega, T) = \frac{1}{e^{\hbar|\Omega|/(k_b T)} - 1} \tag{4.2.2}$$

$$N_s(\Omega, T) = \frac{1}{e^{\hbar|\Omega|/(k_b T)} - 1} + 1 \tag{4.2.3}$$

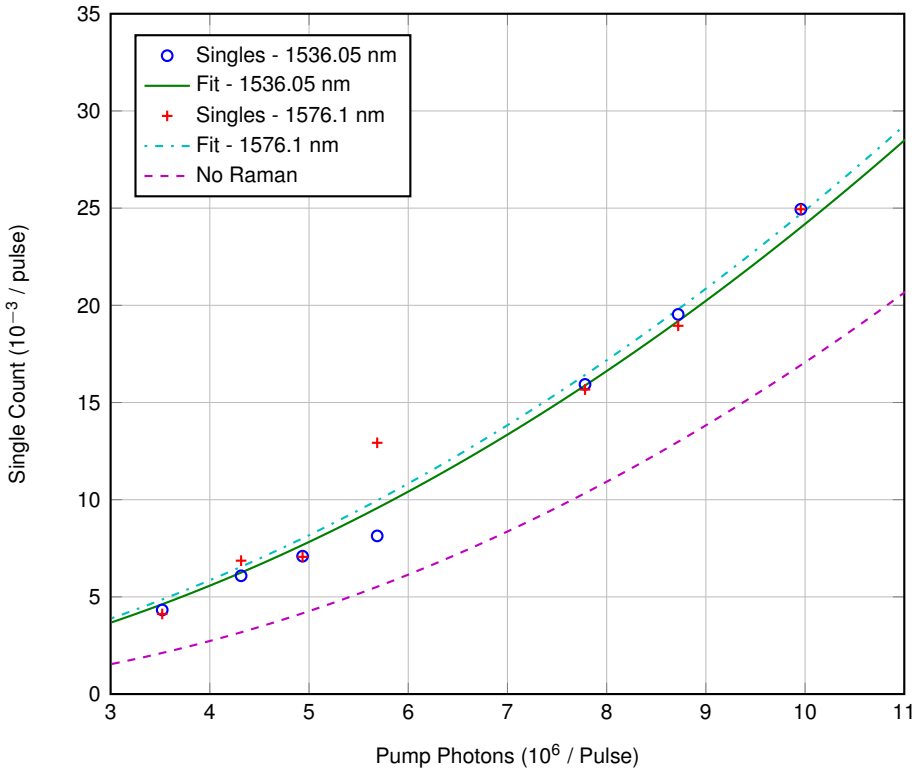

Figure 4.2.1: Measured single counts as a function of pump power for a detuning of 20 nm after dark-count subtraction. Also shown is the count in the absence of Raman noise photons.The statistical error bars are within the marks.

where $\Omega = \omega_p - \omega_s$ and T is the temperature of the WG (room temperature in our case). The integral in 4.2.1 is over the temporal duration of the pump pulse to yield the photon number per pulse.

The fit shown in Fig. 4.2.1 is a least-squares fit of Eq. 4.2.1 with only $|g_r|$, the magnitude of the Raman gain coefficient as a free parameter. The calculated g_r is $28 \pm 3\,\mathrm{W^{-1}m^{-1}}$ for the Stokes channel, and $38 \pm 3\,\mathrm{W^{-1}m^{-1}}$ for the anti-Stokes channel at 20 nm. For 15 nm, the values are $30 \pm 5\,\mathrm{W^{-1}m^{-1}}$ and $45 \pm 8\,\mathrm{W^{-1}m^{-1}}$ for the Stokes and anti-Stokes channels, respectively.

4.3 Coincidence-to-Accidental Ratio Results

The dark-count subtracted CAR is plotted in Fig. 4.3.1, and the corresponding coincidence and accidental counts per pulse are plotted in Fig. 4.3.2 for both detunings. For a detuning of 15 nm, the maximum CAR is nearly 400 for 2.8×10^6 pump photons per pulse. This is a photon-pair generation rate of 1.3×10^{-3} photons per pulse. In the 20 nm case, the CAR is almost 170 for a slightly higher pump power and photon-pair generation rate (2.2×10^{-3} photons per pulse). In comparison, previous work with this material achieved a CAR of less than 10 due to very high loss [81]. Fiber sources on the other hand, require specific detunings to avoid Raman gain peaks and cryogenic temperatures to reduce the phonon population enough to achieve similiar CAR values [85]. Our WG achieves this performance for a compact, room-temperature device which promises scalability and integration with other optical elements.

The a:Si-H WG we studied has demonstrated efficient photon-pair generation over a large detunning (Ω). Despite the amorphous structure, which results in spectrally broader Raman gain, compared to c-Si, the large nonlinearity and low two-photon absorption facilitates the generation of high-quality pairs are generated.

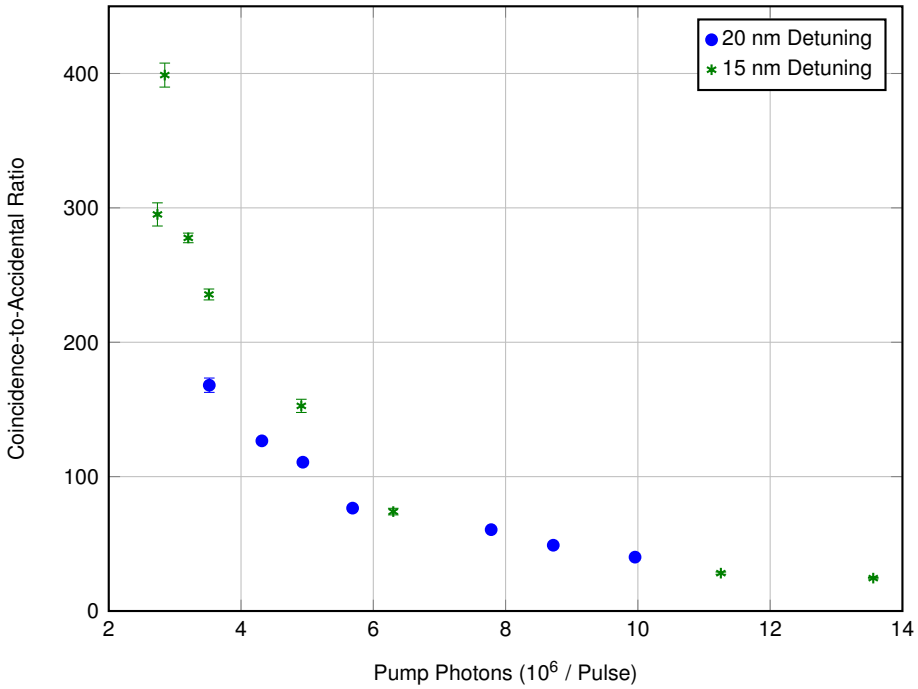

Figure 4.3.1: The CAR plotted here is dark-count subtracted. The highest CAR for a detuning of 15 nm is 399 (168 for 20 nm).

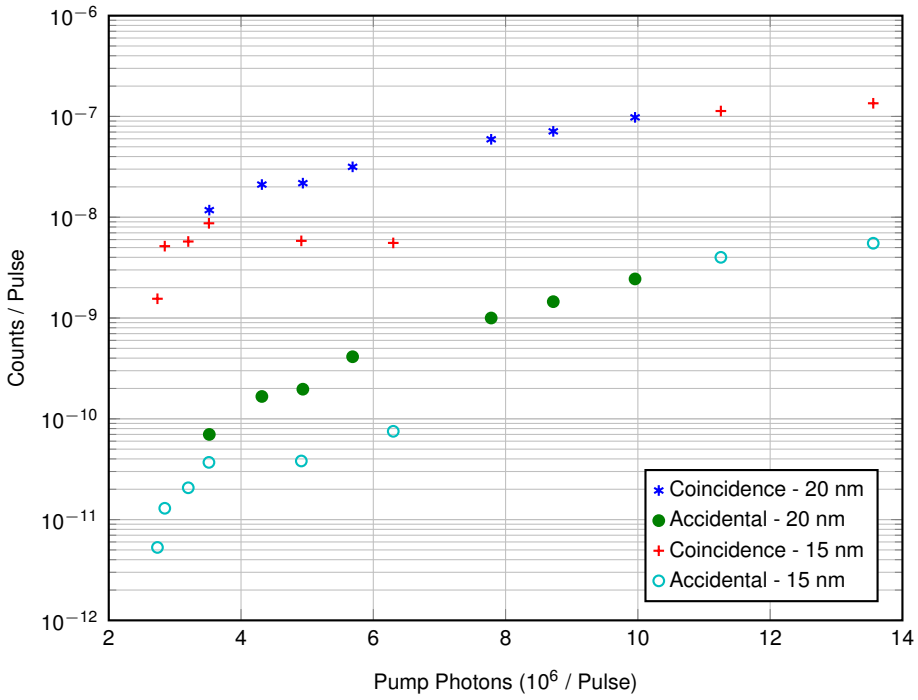

Figure 4.3.2: Dark-count subtracted coincidence and accidental coincidence count per pump photon per pulse. For low pump powers, the accidental coincidence count is dominated by Raman photons.

4.4 Conclusion

We have shown photon-pair generation using a a:Si-H WG with exceptional CAR over multiple, widely detuned wavelength channels. Because of the high optical nonlinearity of our device, the pump power requirement is lower than competing $\chi^{(3)}$ systems which are CMOS compatible. Despite the presence of moderate Raman gain for the two detuning presented, no cryogenics are needed for high CAR of up to 400.

Based on our result, we see promise for this material in future large-scale integrated quantum optics applications. Because of its compact size of our device,

this material is especially well suited to traveling wave designs. A possible future application is a large multiplexed heralded single-photon source which would be an enabling technology for many quantum optics experiments.

5 Microresonator Eigenmode Simulation

We study the linear properties of a WGM resonator by first solving for the eigenfrequencies and electromagnetic field distributions of the supported resonator modes using a FEM solver [40]. Our simulations described in the following sections are critical to understanding the dispersion of the cavity and modal volume of the resonant modes. These parameters are crucial to the nonlinear interactions simulated in later chapters. We also compare the numerical model to an analytic one based on an effective index method. Finally, we use coupled mode theory (CMT) in order to understand the evanescent coupling between a WG and the microring or microdisk [86, 87].

5.1 Numerical Method Framework

A simple rearrangement of Maxwell's equations will produce the magnetic field wave equation,

$$\nabla \times \nabla \times \boldsymbol{H} = -\frac{\epsilon_r}{c^2}\frac{\partial^2 \boldsymbol{H}}{\partial t^2}, \tag{5.1.1}$$

which is the basis on which the simulation is built [39]. This equation is used over the typical electric field wave equation because as long as each element has the same magnetic susceptibility, the magnetic field will be continuous across interfaces [40].

Next, we assume that the resonator's components are temporally invariant, besides the general sinusoidal oscillation at frequency ω. The magnetic field solution takes the form

$$\boldsymbol{H}(\boldsymbol{r},t) = \boldsymbol{H}(\boldsymbol{r})e^{-i\omega t}. \tag{5.1.2}$$

where $\boldsymbol{H}(\boldsymbol{r})$ is the temporally invariant spacial distribution of the magnetic field. As the relative magnetic permeability is 1, the constitutive relation for the magnetic field is simply $\boldsymbol{B} = \mu_0\boldsymbol{H}$ as before. Because of the axial symmetry of the resonator structure, the accumulated round-trip phase must be periodic for a supported mode, therefore $\boldsymbol{H}(\boldsymbol{r}) \propto e^{im\phi}$, where $m \in \mathbb{Z}$ and represents the mode's azimuthal mode number. This is the first of two (or three) mode numbers.

5.1.1 Simulation Setup

Based on previous work [40, 88], we implemented a fully-vectorized numerical solver in the FEM software, COMSOL. This allowed us to solve for the resonant WGMs by only assuming the radial symmetry of the device. While analytic modes work well for spherical or toroidal resonators, our numerical method has proven to be more accurate for the planar disks and resonators typical in integrated platforms like ours.

One of the advantages of this model is that the user can set m so that only a certain family of modes can be studied, which as an example, simplifies parameter searches for satisfying PM conditions. Other than the restrictions inherent in the the 2-D axial symmetric geometry and those listed above, the solution of the eigenmode of the resonator is of the form below:

$$\boldsymbol{H}(\boldsymbol{r}) = e^{im\phi}\{H^{\rho}(\rho,z), iH^{\phi}(\rho,z), H^{z}(\rho,z)\}. \tag{5.1.3}$$

From this solution the corresponding electric fields can easily be solved for.

We should note that the model does not completely ignore the tensor nature of the electric relative permittivity. However, this method constraints it to its diagonal form,

$$\boldsymbol{\epsilon}_r = \{\epsilon_\perp, \epsilon_\perp, \epsilon_\parallel\}, \tag{5.1.4}$$

where $\epsilon_\parallel(\epsilon_\perp)$ is in the axial direction (in the transverse plane). This allows us to simulate devices that have birefringence as long as the material is z cut, which extends the scope of this method beyond the the $\chi^{(3)}$ results shown here. Strekalov et al. used our model to calculate the geometry needed for a lithium niobate resonator to be naturally phase-matched for both frequency doubling and parametric down conversion [15].

5.1.2 Refractive Index

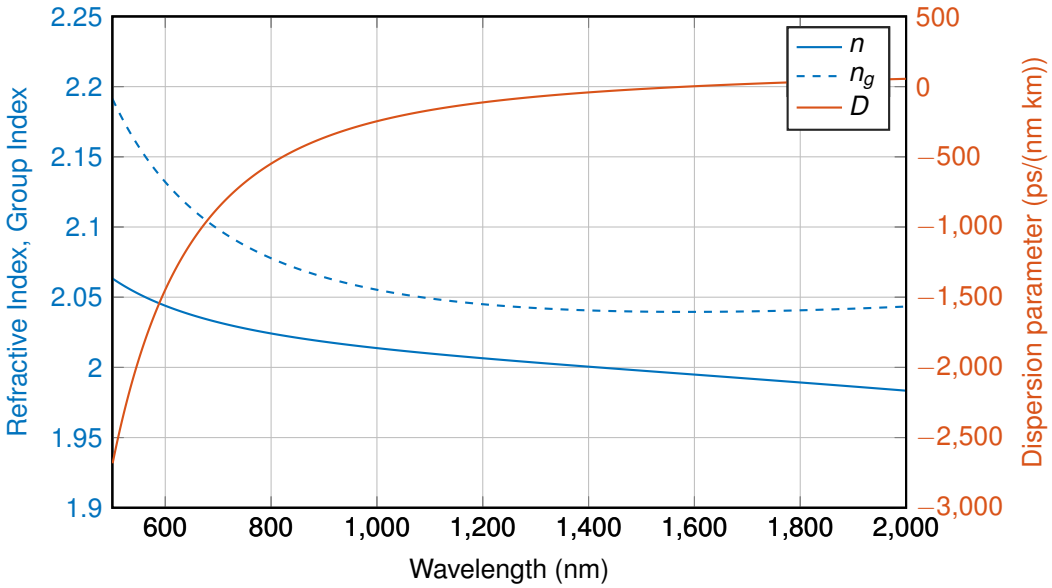

Figure 5.1.1: The refractive and group index of bulk Si_3N_4 are shown. The material has anomalous dispersion only above 1585 nm.

The model relies on the Sellmeier equations for index as a function of wavelength to simulate the dispersion of the cavity. In the case of Si_3N_4, we use an expression for the index of refraction of the form,

$$n^2(\lambda) = 1 + \frac{3.0249\lambda^2}{\lambda^2 - 135.3406^2} + \frac{40314\lambda^2}{\lambda^2 - 1239842^2}, \tag{5.1.5}$$

which is valid from 310 to 5504 nm [89]. The result is plotted in Fig. 5.1.1. This is input directly into the numerical model as-is as the refractive index ($\mathrm{Re}\{\epsilon_r\} = n^2(\omega)$).

The Taylor series expansion of the mode-propagation constant, β, gives relations for the group velocity, v_g, and the group index of light, n_g, via the first derivative with respect to the angular frequency, ω:

$$\beta_1 = \frac{1}{v_\mathrm{g}} = \frac{n_\mathrm{g}}{c} = \frac{1}{c}\left(n + \omega\frac{dn}{d\omega}\right), \tag{5.1.6}$$

$$n_g = n + \omega\frac{dn}{d\omega}. \tag{5.1.7}$$

The derivative of the inverse group velocity with respect to angular frequency is the GVD term:

$$\beta_2 = \frac{1}{c}\left(2\frac{dn}{d\omega} + \omega\frac{d^2n}{d\omega^2}\right), \tag{5.1.8}$$

which is proportional to the dispersion parameter D. The bulk material has normal dispersion throughout the wavelengths of interest.

5.1.3 Geometry and Meshing

The model relies on the geometric simplification from a three-dimensional ring or disk to a two-dimensional cross-section in the $\hat{r} - \hat{z}$ plane. While this dramatically

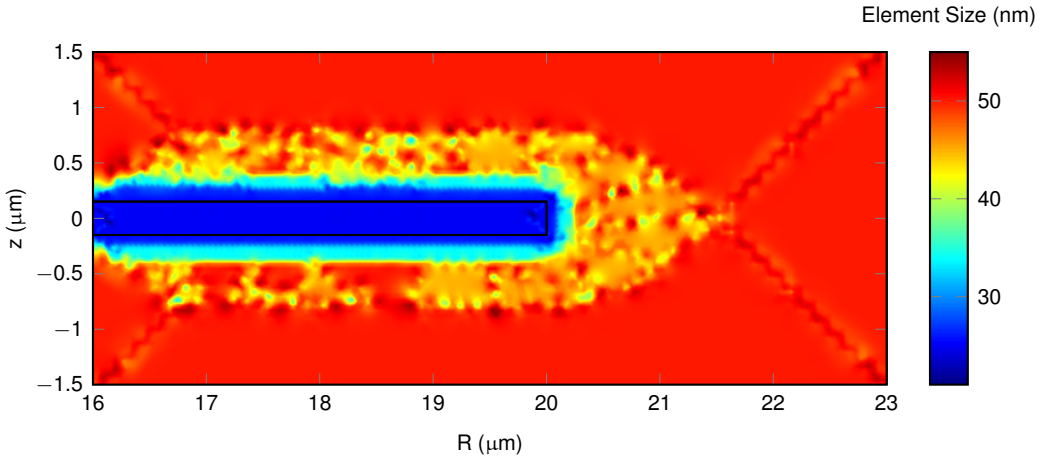

Figure 5.1.2: The geometry of a typical Si_3N_4 disk simulation is shown here. The colors represent the mesh element size for the given meshing parameters, $d_{\max} = 25\,\mu$m, $c_{\text{vac}} = 2$.

speeds up computation compared to a full 3-D solver, it complicates the study of racetrack-shaped resonators or scattering which breaks the axial symmetry of the resonator. Regardless, once we select a cross-sectional geometry of interest, we can draw it and have it meshed.

The mesh quality affects both the solution precision and computation time dramatically. In general, a finer mesh results in a more accurate eigenfrequency. However, the computation time increases roughly as $1/\bar{d}^2$, where $\bar{d}$ is the average length of a mesh element. A balance needs to be struck between precision and computation time in order to ensure the best real-world performance of the model.

The general rule of thumb for FEM computations of electromagnetic fields is five elements per wavelength in the material. Because of the material indexes and the wavelengths of interest (generally 500 nm to 2 μm in vacuum), the maximum element dimension, $d_{\max}$, should range from 50 nm to 200 nm in the dielectric.

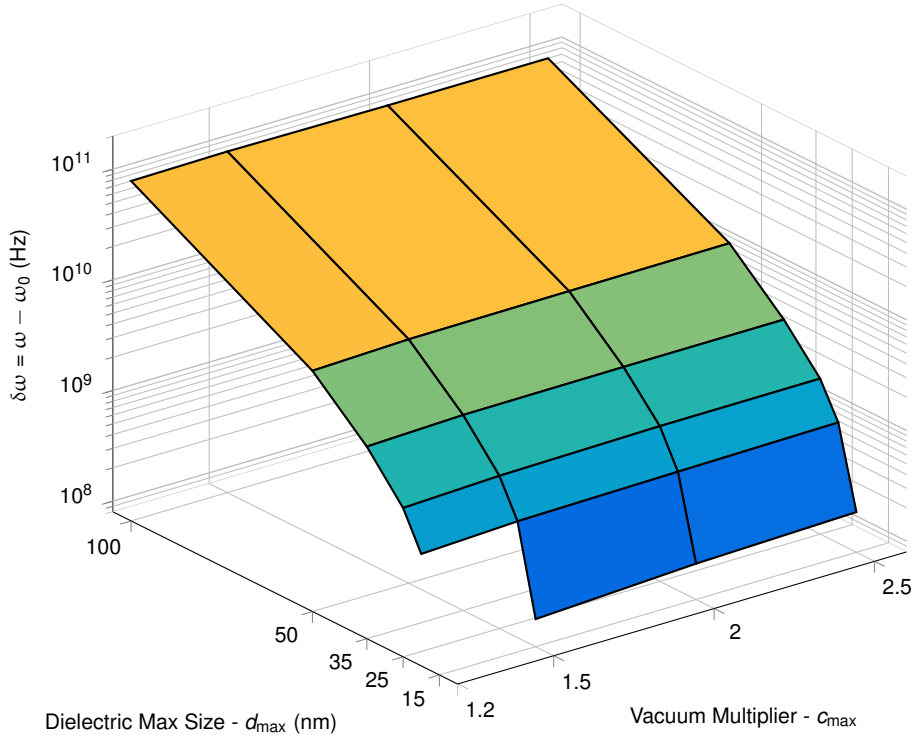

Figure 5.1.3: The simulated eigenfrequency for the same mode in the telecom C-band is shown here for different mesh parameters. ω_0 is the frequency with $d_{\max} = 15\,\mu$m, $c_{\text{vac}} = 1.2$.

Generally, we do better than this because we have the computational resources and the precision of the result becomes important for high-Q-factor devices.

We consider two different regions of our geometry when it comes to meshing, the dielectric element and the vacuum element. Since most of the energy of the wave is concentrated in the high-index dielectric part, we base the mesh size on this region. In the vacuum, the maximum mesh size is the dielectric value multiplied by a constant, c_{vac}. The behavior of various values of c_{vac} and $d_{\max}$ are used to calculate solution time and convergence in Fig. 5.1.3. The meshing around the domain boundaries are controlled by the internal COMSOL meshing algorithm. Results show that good performance is usually met with values of $d_{\max} = 25\,\mu$m,

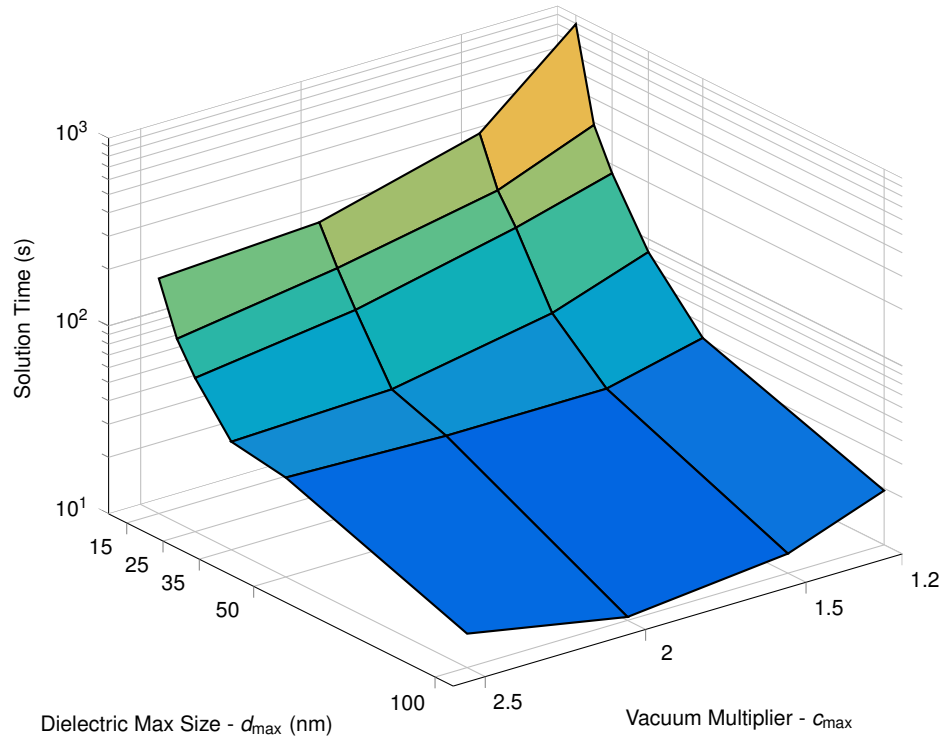

Figure 5.1.4: Similar to Fig. 5.1.3, but the solution time for one iteration of the solver is plotted here. Note that axes have been rotated to help visualization. Generally, as the total number of mesh elements increases, the solution times increase. However, in some instances the number of steps the solver takes until it reaches the convergence criteria changes, which explains the local variations in the this global trend.

$c_{\text{vac}} = 2$, but there is some model to model dependency here.

5.2 Eigenmode Simulation Results

The FEM numerical results are split into two related categories. First is the study of the modal shapes themselves. This is useful for understanding the resonance spectrum of the device and how it relates to the order of the modes, $\{m, n, l\}$ and the FSR of the structure. It is so important for determining the mode volume and

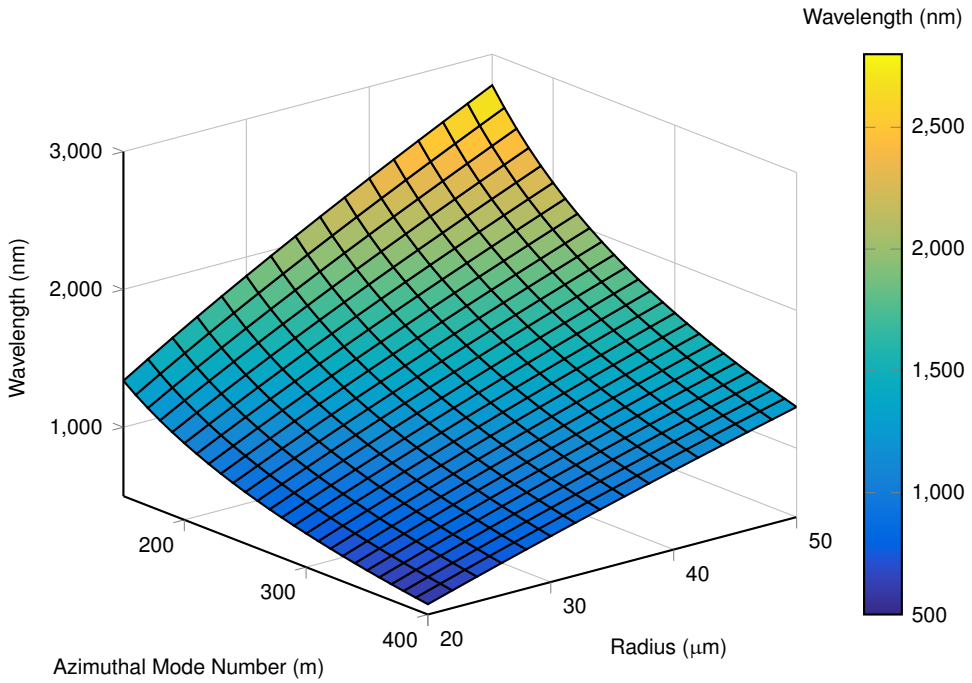

Figure 5.2.1: A plot of the change in wavelength for the primary mode, $\{m, 1, 1\}$, TE-polarized, for changes in the azimuthal mode number and the radius of a Si_3N_4 disk. The thickness of the simulated structure is 360 nm.

overlap between different modes. This ties directly into the second part of the results, which is engineering a geometry so that a nonlinear optical process can be driven. We shape the disk or ring by adjusting its geometry, polarization and cladding in order to satisfy both momentum and energy conservation conditions.

The modal structure, characterized by the mode numbers $\{m, l, 1\}$ and the polarization are the solutions to the fully-vectorized field equation. The dispersion of these modes is set by a combination of the material bulk properties and effects due to light-confinement of the structure. This controls the FSR and the linewidth of the cavity, crucial parameters to understanding the nonlinear performance of the device. It should be noted that some estimates on the Q-factor of the resonator can be made from these simulation results [40, 90, 91].

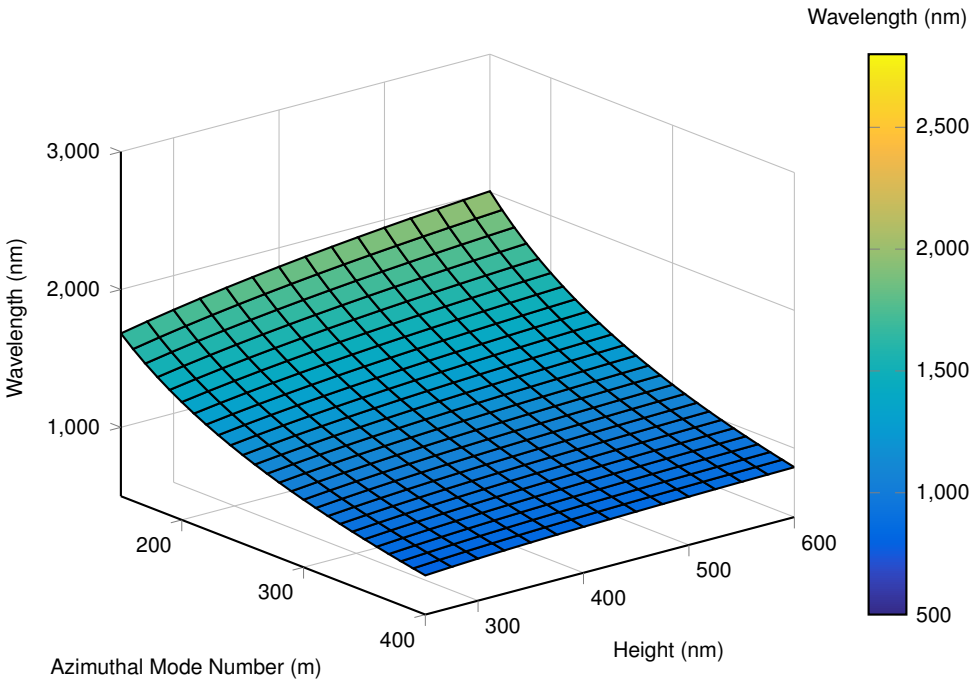

Figure 5.2.2: The same as the previous figure, except here the height of the disk is varied, not the radius. The radius of this simulation is 25 μm.

5.2.1 Natural Phase Matching For Nonlinear Processes

We propose two different methods for achieving natural phase-matching for FWM in these microresonator structures. One relies on the inherent differences in the dispersion between the devices TE and TM modes, while the other uses a wedged resonator in order to effectively tune the waveguide geometry with respect to frequency. Poling is also possible for certain materials like LN. These effects are combined with the inherent dispersion due to cross-section and bending radius in order to satisfy the energy conservation and momentum conservation relations:

$$\omega_{\mathrm{p1}} + \omega_{\mathrm{p2}} = \omega_s + \omega_i \tag{5.2.1}$$

$$m_{\mathrm{p1}} + m_{\mathrm{p1}} = m_s + m_i \tag{5.2.2}$$

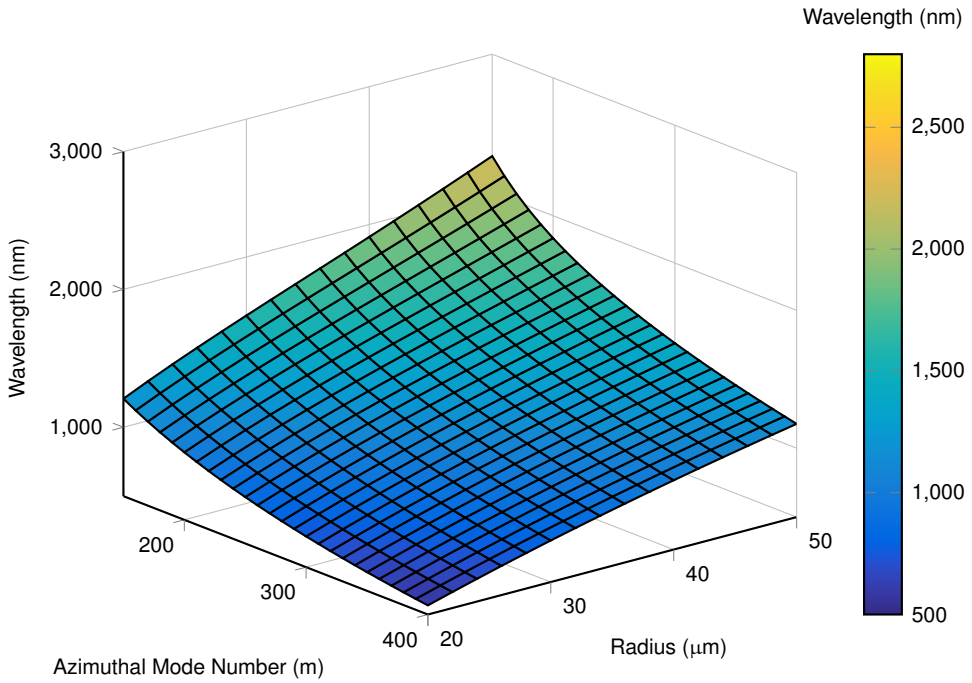

Figure 5.2.3: This plot complements Figure 5.2.1, because it is the primary TM-polarized mode. Comparing the two side-by-side shows how the guiding dispersion has a smaller effect on this polarization.

where p1 and p2 correspond to the two pumps, and s and i are for the signal and idler.

On-chip resonators typically only support a limited number of spatial modes, especially rings which can be designed to be single mode. Because of the discrete nature of the spectrum of the resonator, finding modes which satisfy the momentum conservation equations is relatively straightfoward. However, because of dispersion in the cavity, it can be difficult to satisfy the energy conversation relation. In order to be considered phase-matched, difference in the r.h.s. of Equation 5.2.1 has to be close to zero or negative, so that a strong pump can bring the total sum to be less than the resonance linewidth, $\Delta\omega$.

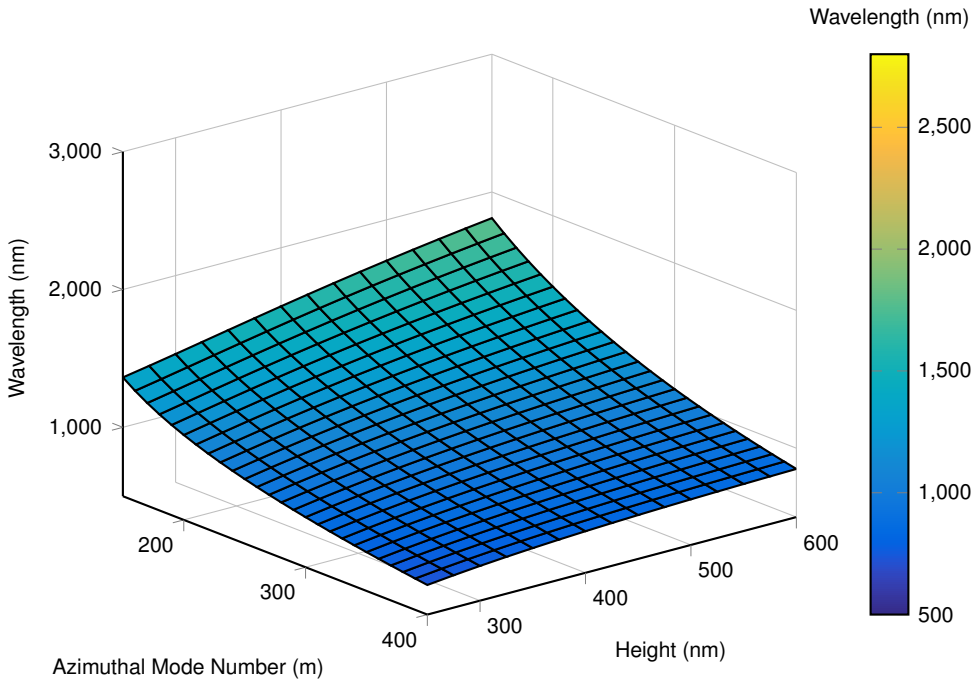

Figure 5.2.4: Similarly, we compare this plot of the TM polarized mode to Figure 5.2.2.

Resonator Wedge

For a given cross-section, restricting ourselves only to primary modes, higher-frequency light has a smaller mode volume. We can use this property to our advantage by wedging the edge of the resonator. Because of the variation in the thickness of the resonator, the fundamental mode is deeper into the wedge. In essence, a higher frequency mode sees a smaller cross-section of greater radius than a lower one. Figure 5.2.6 gives an example of the change in mode-shape for different wedge angles. This counter-acts the natural dispersion of the material in such a way that with proper choice of θ, the wedge angle, natural PM can occur [57].

The FSR for various angles and thicknesses is shown in Figure 5.2.5. The eigenmodes for primary TE excitations are shown in 5.2.6. The distortion of mode shape

can be clearly seen. As an example, simulations show that a Si_3N_4 resonator with a parameters of $R = 20\,\mu$m, $h = 500\,$nm, $\theta = 18^\circ$ can satisfy both PM conditions for QFC with a signal/idler pair at 1200 nm/640 nm.

We should note that a high precision in resonator wedge angle can be difficult to achieve. Practically the angle depends on the details of the etch process that defines the resonator. This etch process also determines the sidewall roughness of the device, which is a major if not primary contributor to intrinsic loss rate. A tradeoff between between these parameters is important to understanding the performance of the device.

Polarization

Due to the difference in GVD between the two polarizations as discussed earlier, it is possible to use the resonator's TE and TM modes to satisfy the necessary PM relations. In the example shown below, the lower frequency modes are TM-polarized while the the higher frequency pair is TE. FWM can be used to frequency convert a signal with a large detuning using two pumps located in the two central wavelengths. This necessarily means that the pump pairs are cross-polarized. While the inter-mode overlap is decreased compared to single-polarization FWM, this process can phase-match spectrally distant modes. Figure 5.2.7 shows the different field profiles of the four modes.

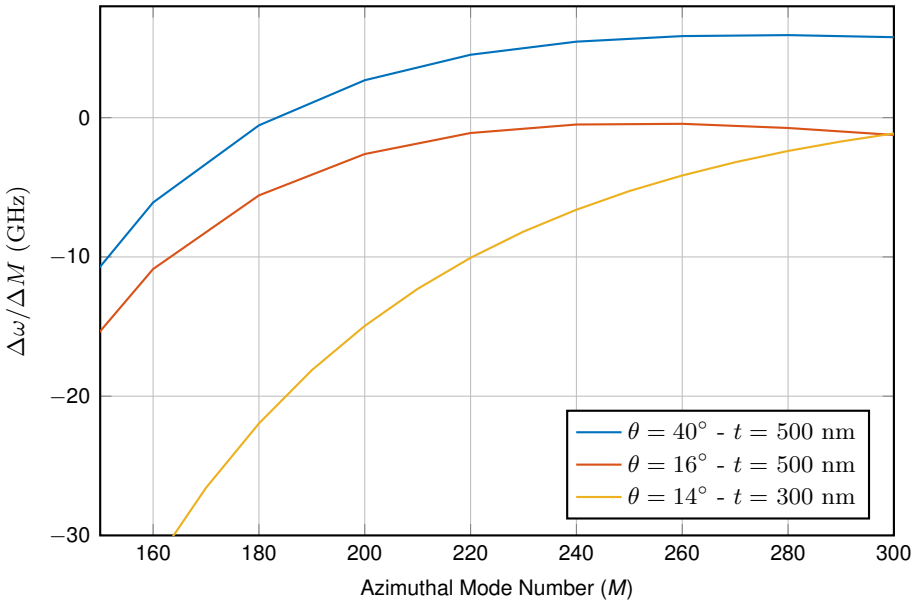

Figure 5.2.5: The change in FSR for different combinations of angles and resonator heights for a radius of 25 μm.

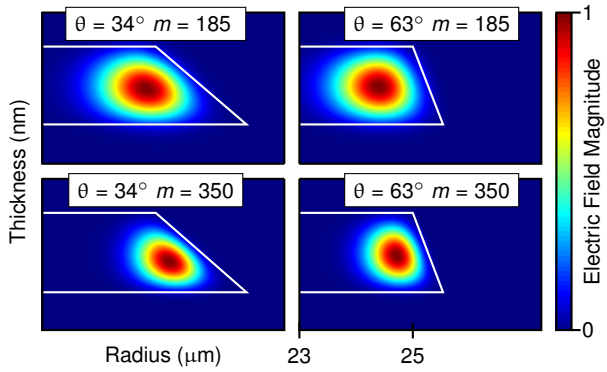

Figure 5.2.6: This plot shows the electric field for a primary TE-mode at different azimuthal mode numbers and resonator wedge angles.

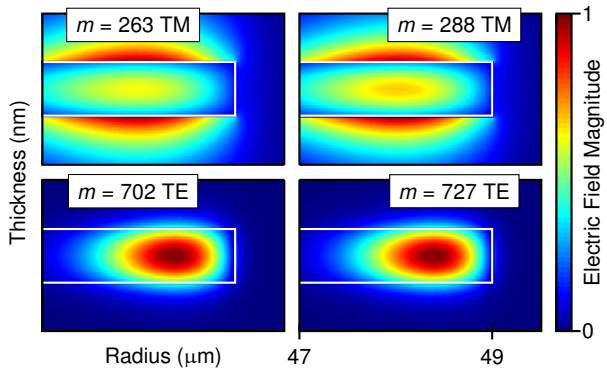

Figure 5.2.7: Four on-resonant waves that are phase-matched between the O-band and the visible range. This device can be used for QFC between a 1310-nm photon source (where standard fiber has zero dispersion) and a silicon SPD, for example.

5.2.2 Estimating Quality Factors

By using perfectly-matched layers (PMLs), the numerical code can estimate the radiative loss of the resonator. These layers correspond to domain elements placed on the edges of the simulated volume that have complex impedances in order to eliminate reflections from the edges of the vacuum box that the simulation takes place in. Using this method, bending loss can be calculated from the imaginary part of the now complex eigenfrequency.

5.3 Comparison to Analytic Models

Analytic models for spherical or toroidal geometry cavities describe WGMs well. However, for a device where the resonator resembles a flat disk, these same analytic models are invalid. In order to compare our numerical FEM solutions to an analytic expression, we need one that better takes into account the cylindrical symmetry of the device.

This method is based on the Helmholtz equation in cylindrical coordinates for the axial field of the WGMs. This equation is

$$\nabla^2 \boldsymbol{F} = \frac{n^2(\mathrm{r})}{c^2} \frac{\partial^2 \boldsymbol{F}}{\partial t^2} \tag{5.3.1}$$

where $\boldsymbol{F}$ is the field in the $\hat{z}$ direction. For TE modes, $\boldsymbol{F} = \boldsymbol{H_z}$ while for TM modes, $\boldsymbol{F} = \boldsymbol{E_z}$[59]. While this method represents the exact solution for an infinitely tall cylinder, we can use an effective-index method to account for the finite thickness of the resonator. We estimate the effective index of the device by simulating the resonator as a WG in the z-direction. Because of the boundary condition on the interface of the device, the solutions consist of Bessel functions of the first kind, $J_m(\tilde{k_1} r)$ inside the dielectric, and Hankel functions of the first kind, $H_m^{(1)}(\tilde{k_2} r)$ outside it.

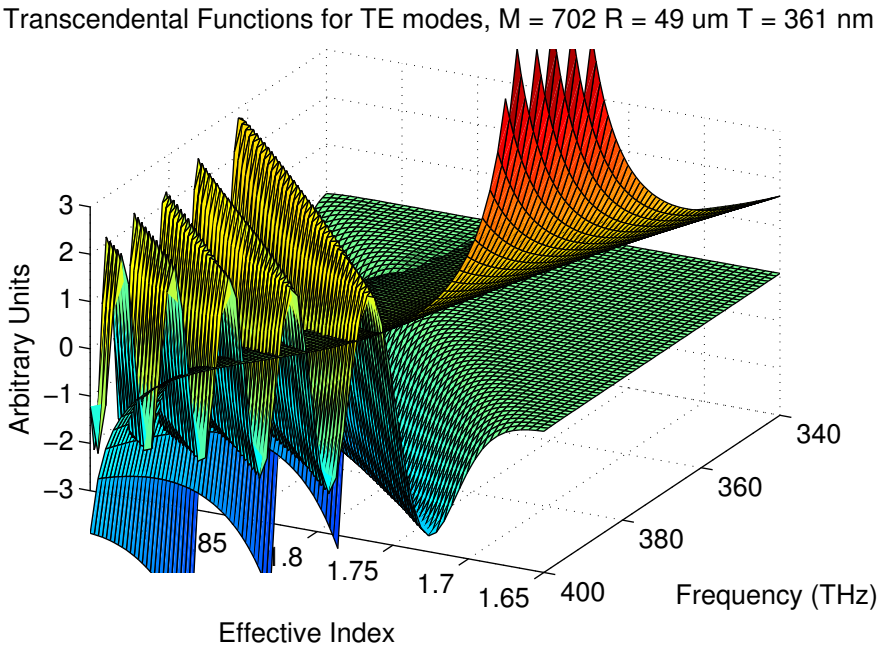

Figure 5.3.1: Eigenmodes of the resonator are represented by the points where both functions are simultaneously equal to 0.

This model and the FEM eigenmode solutions typically agree within a few percent in terms of absolute frequency. However, the FEM model directly gives the full field equations and does not split the calculation. We need less assumptions to construct the FEM model compared to this analytic one, which because of its use of the effective index method will always only be an approximation. For this reason, we continue with the FEM model.

6 Microresonators Coupling

The heart of the experiments described here and in the next two chapters are a collection of photonic chips fabricated at Sandia National Laboratory. These fall into two categories; rings fully encased in silicon oxide, and disks mounted on a pedestal surrounded by an air gap as seen in Section 2.3. Both are Si_3N_4 devices on silicon wafers with 2 bus waveguides (4-port devices). Both have etched edge couplers with inverse waveguide tapers to reduce coupling loses. However the rings and disks have dramatically different Q-factor and dispersion profiles which naturally tailors them to different applications.

In the following experiments, we will mainly focus on the rings. Because of their single mode (per polarization) nature and designed dispersion, they prove useful from a physics point of view. From a practical point of view, they are fully clad which makes them much easier to handle and couple.

In this Chapter, we will discuss the apparatus used for coupling into the chips and notes on the quality of the coupling itself. This equipment is used for all data acquisition in this and the next two chapters unchanged.

6.1 Sandia Experience

As part of our collaboration with Sandia, the author spent two months working along side Dr. Camacho's post-doc, Dr. Ian Frank at the Center for Integrated Nanotechnologies in New Mexico. This was valuable for the insight gained into device fabrication in general and details of our chips specifically. The coupling setup presented below is heavily influenced by that at Sandia.

Also, initial measurements in New Mexico showed expected Q-factor for the discs and lower than expected Q-factor for the rings. Initial pump-probe FWM experiments carried out at Sandia showed promise however, and the author returned from New Mexico with tens of chips of various geometries and bus WG to resonator gaps (to tune the coupling Q-factor).

6.2 Experimental Setup

The central apparatus of the resonator experimental setup is the alignment setup and enclosure. It consists of holders for the chip and the v-groove array, vacuum for chip capture, resistive heaters for temperature control, and motion control stages for alignment. A 12x zoom lens and digital camera provide guidance for alignment. The setup sits in an enclosure to protect the sensitive chip from dust and environmental factors. This is especially important in a lab which is quite dusty.

The chips have 4 edge couplers, with a standardized pitch, and a matched v-groove array holding fibers to interface with the ports. We needed mounts which could secure these devices and themselves be secured to standard third-party motion stages. Because 4 fibers had to be aligned simultaneously, we needed motion control in 6-degrees of freedom (full 3-D translation and rotation).

Figure 6.2.1 shows the finalized mount used in the experiment. We designed these mounts to interface between standard Thorlabs stages and the chips and v-grooves using the freeware computer-aided design program OpenSCAD. The mounts include provisions for standardized mounting hardware. The design allows for a thermistor and resistive heater within the mount on the chip side. Internal passages were also needed so that the chuck could secure the chip with vacuum. We prefer this approach to using tape or a clamp because it is clean, low-stress, and repeatable. The vacuum for the chuck is provided by a re-purposed pump from a basic set of vacuum tweezers that has been running non-stop for 3 years as of this writing. The building supplied vacuum proved contaminated.

After finalizing the design virtually, we 3-D printed mounts using Northwestern's 3D Printing & Rapid Prototyping Lab located in the Ford Motor Company Engineering Design Center. The first round of mounts were printed from RGD525 because of its suitability for temperatures near 60 degrees Celsius. After a small revision to better accommodate the vacuum port, the mounts were instead printed from RGD450 which is cheaper and gives a better finish. The high-temperature requirement was dropped because we showed that with the poor thermal conductivity of the plastic mounts, even our high-end temperature controller (SRS PTC10) could not maintain sufficient stability above 30 to 40 degrees Celsius. Experimentally, this meant we could not tune the resonances thermally, but the need for this never manifest itself.

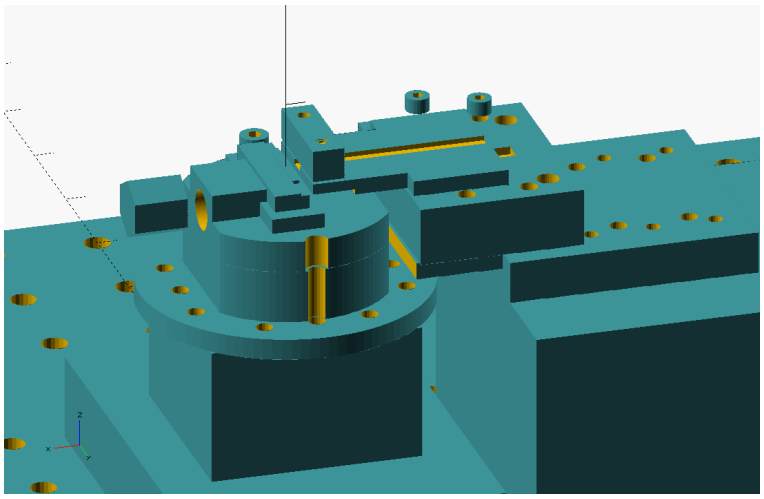

Figure 6.2.1: A CAD image of the vacuum chuck and v-groove holder. Thorlabs makes 3-D model files of their components available via their website which allows us to integrate them into the design process.

The vacuum chuck supporting the chip is mounted on a Thorlabs TTR001 stage that provides rotational degrees of freedom. This is mounted on a Thorlabs PT1 linear translation stage which allows us to easily look at all resonators along one edge of a chip. The v-groove array is mounted on a piezo- and differential drive-controlled Thorlabs NanoMax flexure stage which can translate in 3 directions. Because this stage is responsible for the critical alignment degrees of freedom, it is under computer control via a Thorlabs MDT693B piezo controller. With feedback from an optical powermeter, we can perform automatic periodic re-alignment to ensure consistent fiber-to-chip coupling over long measurements. Figure 6.2.2 shows a photo of the enclosure with the cover removed. The camera and lens system is mounted above the chip/v-groove interface.

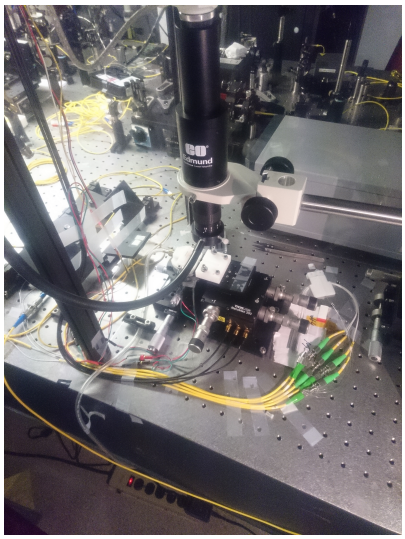

Figure 6.2.2: Photo of the coupling enclosure with the door removed. The v-groove is not mounted in this shot. The clear tube running below the table is for the vacuum. The 4 input/output fibers and cables for motion and temperature control enter the enclosure from the left.

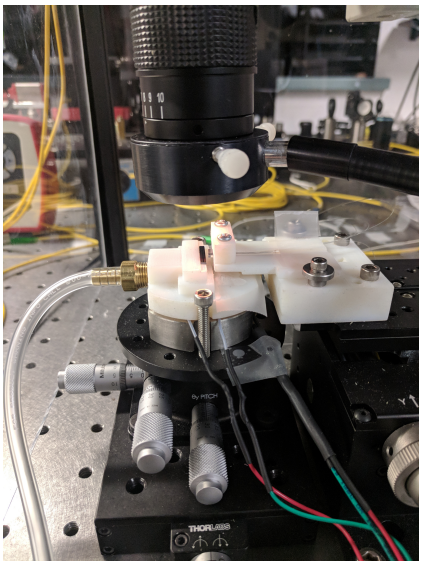

Figure 6.2.3: A closeup of the alignment setup.

6.3 Coupling

We use a simple hand-held red laser, used for optical fiber routing, to align the chip. Unlike the infrared light of our experiments, the red light is easily visible in the camera. Figure 6.3.1 shows this light coupling into a bus waveguide. The bright red spots are due to scattering at the facets. Once the chip is well aligned, the view from the camera resembles the photo in Figure 6.3.2. The diagonal line across the bottom of the screen is the line between the chip above and v-groove below.

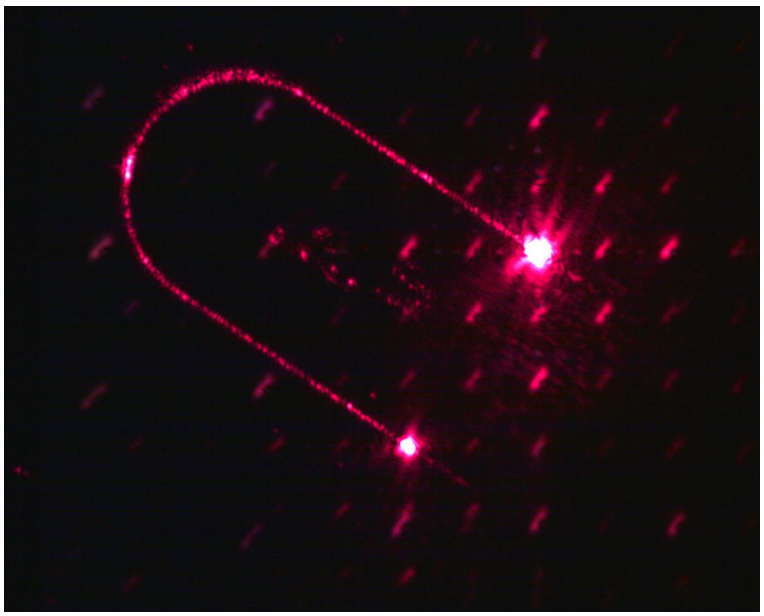

Figure 6.3.1: Red laser light used for alignment. In a dark room, the scattering within the waveguide and in the coupling region is clearly visible.

Transmission losses in this setup are measured to be as low as 3.0 dB per facet. This estimate is based on optimum alignment with clean fibers and facet. It also assumes all loss due to the chip is during WG-fiber coupling. The fiber in the v-groove array is highly-nonlinear fiber, cleaved flat. Because of smaller core diameter compared to regular single-mode fiber, the mode of this fiber better matches that

of the chip. Generally extremely small separations or contact between chip and v-groove lead to lowest losses. We use index matching fluid applied in the gap between the fibers and the chip to provide the final 3-dB improvement in coupling loss reduction.

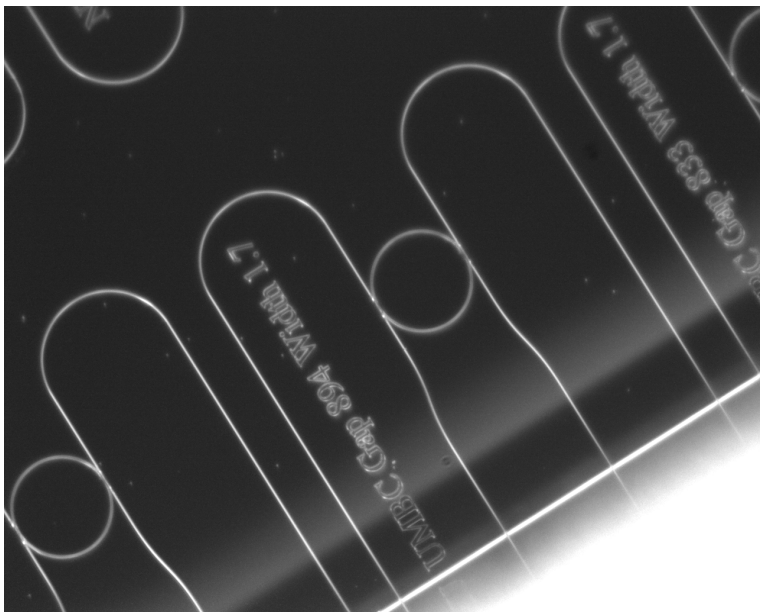

Figure 6.3.2: Coupled and aligned chip, before the index matching fluid is added. The bus WG reflect in the v-groove array in the bottom of the imagine. The optical fibers themselves are not visible while aligning the setup.

The coupling setup provides low loss and good long-term stability. However, fibers and chips can be damaged. Overzealous alignment can damage and chip waveguides, as seen in Figure 6.3.3. As expected, the coupling loss increased from a typical value of 6-7 dB (round trip, from fiber across bus WG to fiber) to more than 40 dB. Another source of damage is to the facet of the chip or fiber, as seen in Figure 6.3.4. High input power combined with bad alignment can burn the interfaces.

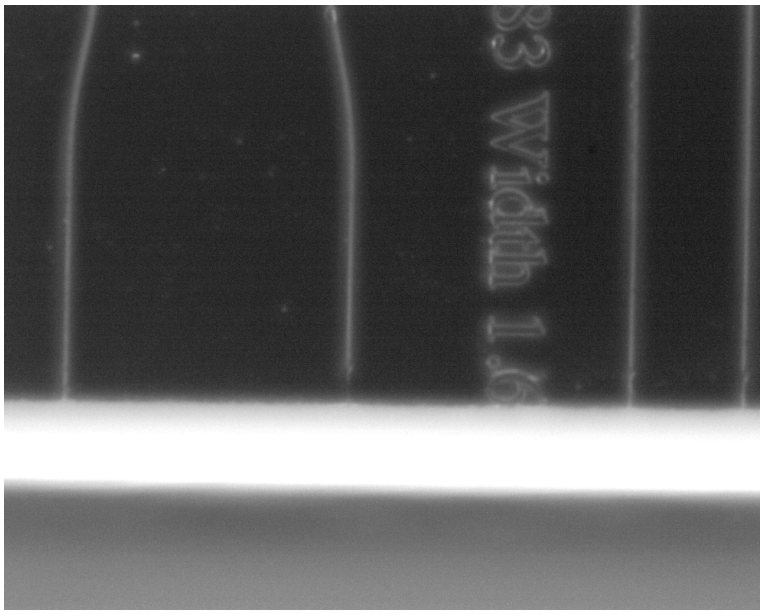

Figure 6.3.3: Broken waveguide shown in the center of the image (to the left of the chip inscription).

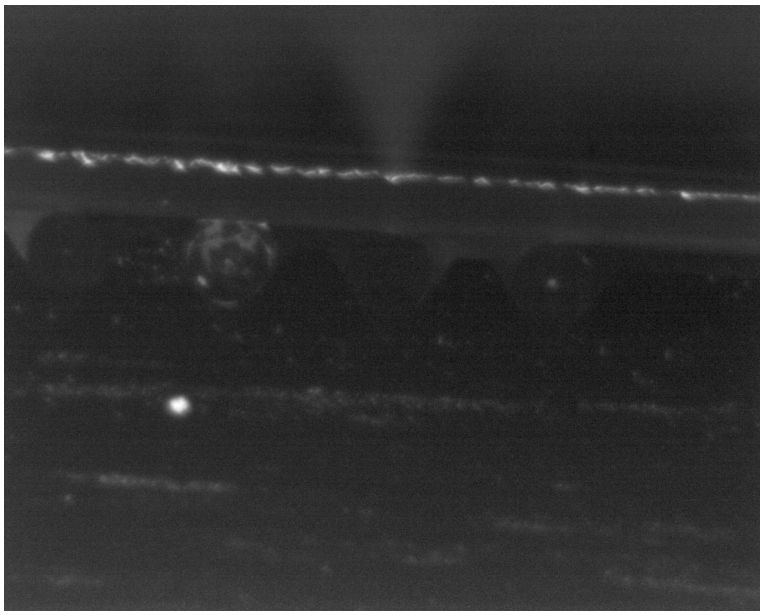

Figure 6.3.4: A damaged fiber in the second position from the left can be seen in the v-groove array. This kind of damage eventually hampered the experiment because of compatibility issues between the remaining chips and arrays.

7 Microresonators

All-Optical Switching

Motivated by work such as Pelc. et al. [35] and others [92, 93, 94], we investigated the possibility to use our Si_3N_4 ring resonators as all-optical switches targeted towards quantum applications. Our group has demonstrated this ability using cross-phase modulation in a fiber loop [95]. We demonstrated high fidelity of 96% between the input and output state at 6 GHz switching speed. However, the size and power requirement of the switch could be improved. We investigate the suitability of our ring resonator system to accomplish the same goal.

7.1 Introduction

Our resonator-based switch relies on the Kerr-effect driven by a strong pump pulse to drive the switching function. Figure 7.1.1 shows two possible modes of operation. In the first case, when the pump is not present, the signal light couples into the resonator and is passed through the cavity to the output port of the device. When the pump is turned on, the pump shifts the cavity resonances to such an extent that the signal is no longer resonant. Our discussion will focus on this mode. However, an alternate exists in which the signal light only couples into the cavity in the presence of the pump.

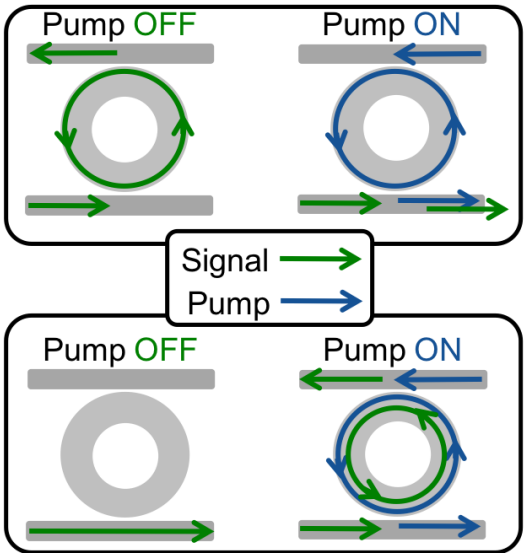

Figure 7.1.1: Two modes of operation for our switch are demonstrated here. Two bus waveguides couple into a resonator and function as the inputs and outputs of the system.

Because we are interested in all-optical switching of quantum signals, the first switching mode is advantageous. The strong pump, when enhanced by the cavity, does not come into direct contact with the signal. Any light that it generates in the cavity, whether through FWM or Raman scattering would be filtered by the cavity resonances, so would not present as in-band noise to the quantum signal.

The intrinsic performance of our resonator as an add-drop filter is the basis for its switching contrast [96]. The filter transmission is directly related to the interplay between the loss-rates to the two bus waveguides, and the intrinsic loss rate of the cavity. Two different conditions are presented in Figure 7.1.2,

$$\frac{1}{\tau_t} = \frac{1}{\tau_d} + \frac{1}{\tau_i}, \tag{7.1.1}$$

$$\frac{1}{\tau_t} = \frac{1}{\tau_d}. \tag{7.1.2}$$

τ_d is the loss rate into the drop waveguide, while τ_t is the loss rate into the through waveguide, or input. The intrinsic loss rate of the cavity is represented by τ_i. Our devices have equal coupling rates to the bus waveguides as described by Equation 7.1.2, but at the expense of allowing some light to be transmitted in the through port, as seen in Figure 7.1.2. Ideally, we would want devices which match the condition described in Equation 7.1.1.

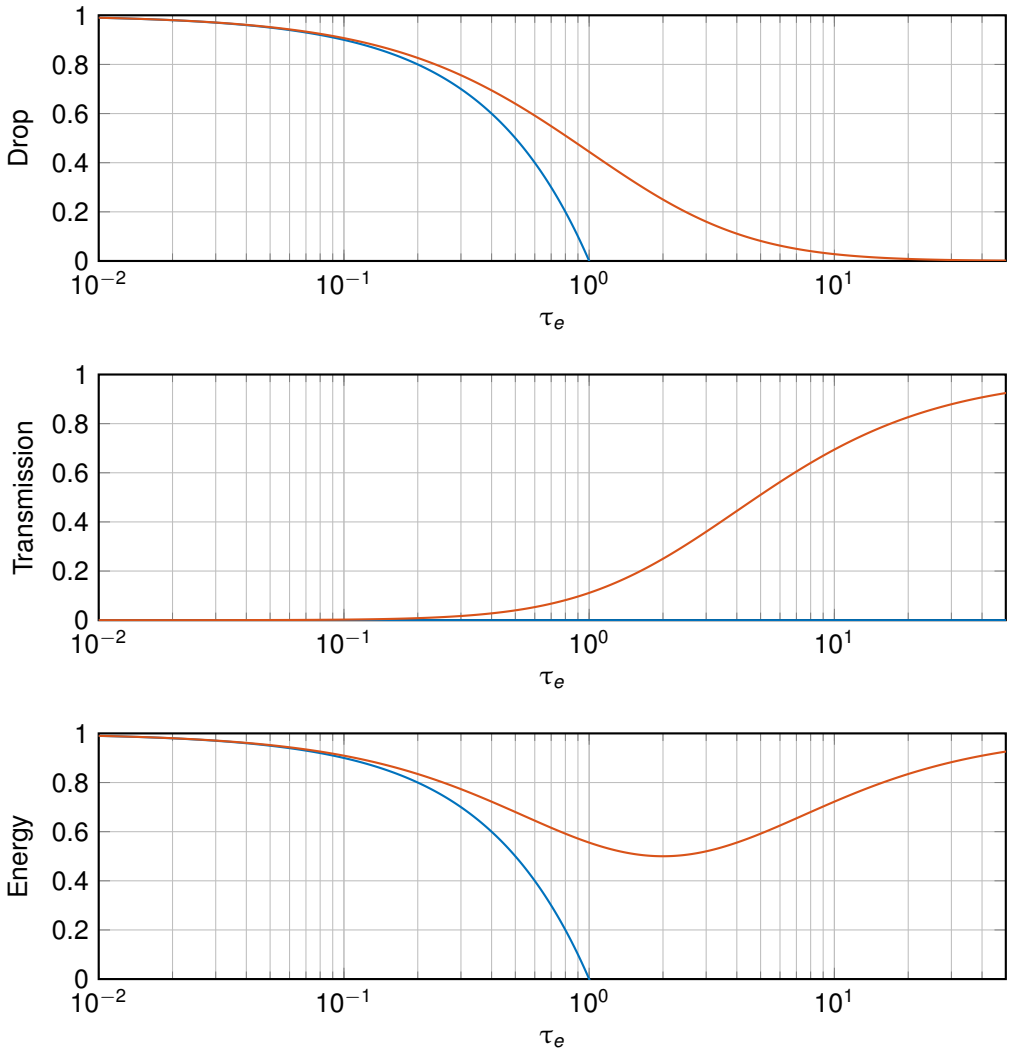

Figure 7.1.2: The energy transmitted through the drop port, transmitted through the bus waveguide without coupling into the resonator, and the total of these two energies. The missing energy is dissipated in the resonator. The red curve represents equal bus waveguide loss rates.

7.2 Experimental Setup

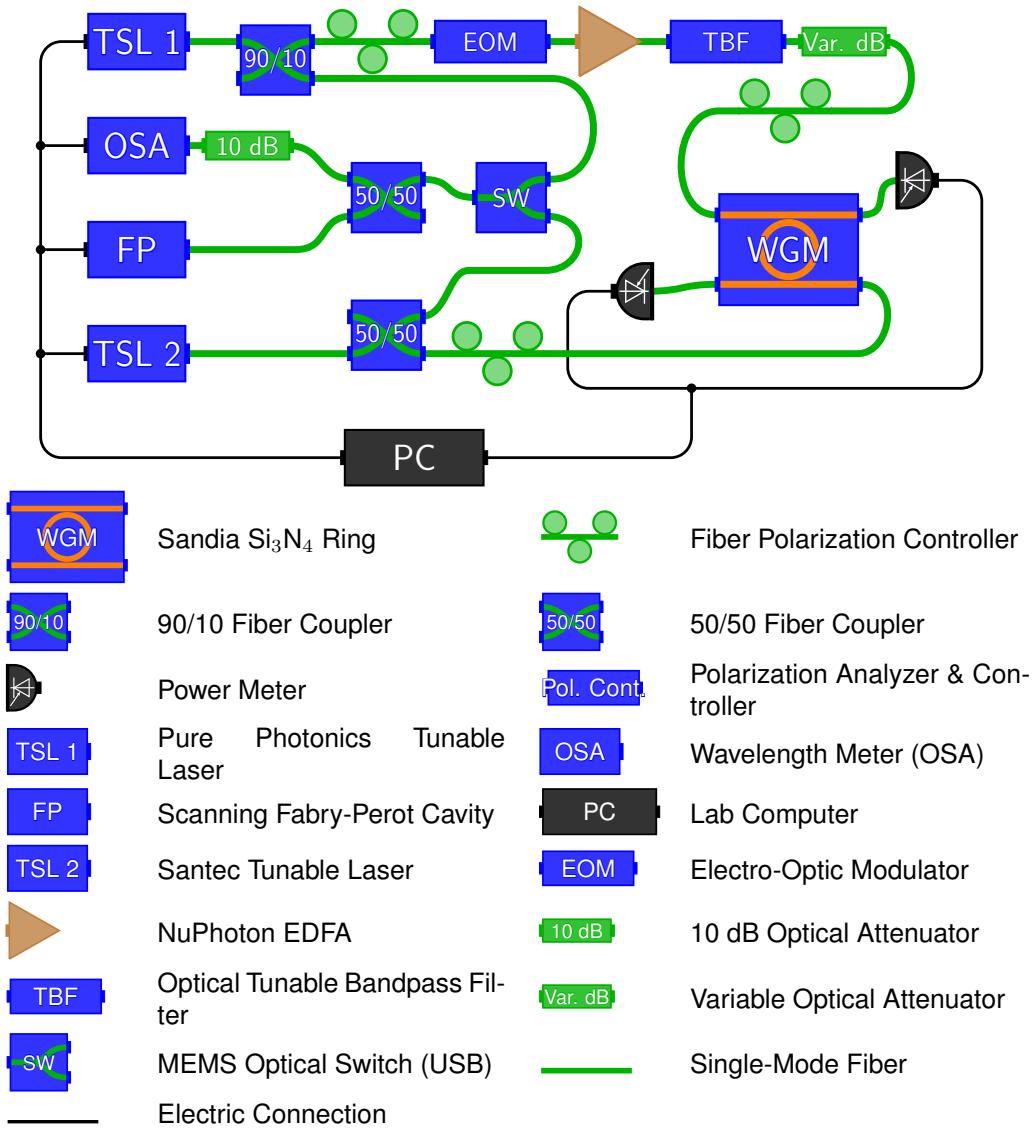

Figure 7.2.1: Experimental setup for switching

In order to experimentally test the switching behavior, we use two tunable lasers. One represents the pump which drives the all-optical switching operation, and the other is the signal. Figure 7.2.1 shows experimental setup. We note the two tunable

lasers. TSL 1 is the pump laser, with a LN modulator to create the switching window. The EDFA and the variable attenuator are used to set the switching pump maximum power. On the other hand, the signal is continuous wave (CW) and relatively low powered. In effect, it probes the shift in the resonance of the cavity. Laser frequency measurement is identical to that described in Section 8.1 with the addition of an optical microelectromechanical system (MEMS) switch which selects the laser of interest, pump or probe.

Because this is a resonant $\chi^{(3)}$ system, performance is an interplay between bulk material properties, pump power and resonator loss and size. These physical parameters are responsible for the Q-factor of the resonator and the FSR. Because we use the shift in resonances to accomplish our switching behavior, signal (or probe) and pump lasers need to be on the grid of supported resonances. A smaller radius produces a compact device with correspondingly smaller mode size, but may make the FSR impractical. Also, a small Q-factor may lower the pump power required to shift the cavity, but the spectral bandwidth of the resonance needs to support the entire signal spectrum. Directly related to this, the temporal lifetime of the cavity sets a bound on the ultimate supported switching speed and switching window for the device.

Finally, thermal considerations play a large part of the device performance. A compact resonator with a large finesse produces a large cavity enhancement which drives the thermal nonlinearity in the system. This effect is the dominate term responsible for the switching rate of the cavity.

For a quantum system, we must also talk about generation of inner-band spontaneous noise from the pump into the signal band. For quantum signals, these noise photons can easily become equal in number to the signal itself. To avoid this pitfall,

we propose to operate the switch in such a way that the passive state (pump off), the signal light couples through the resonator and exists the opposite port. When the pump is turned on, the resonance shifts, and the signal now continues down the bus waveguide, unperturbed by the cavity. Any spontaneous noise generated by the pump will only populate the spectrum where resonances support it, leaving the band occupied by the signal unperturbed.

7.3 Switching Results

Preliminary switching performance is shown in Figures 7.3.1 and 7.3.2. With 800 mW of peak pump power and a 2 ns. switching window, the pump shifts the cavity enough to change the signal contrast by roughly 15%. The first figure shows the cavity shifting the cavity away from the signal, causing more of it to go through the through-port. This is the mode of operation we propose for quantum signals. The second figure shows the same experiment but with the signal wavelength shifted such that the signal is shifted into cavity by the pump. Performance is roughly symmetric, as expected. Figure 7.3.3 shows the measured contrast as a function of the pump power as compared to a simulation of the operation.

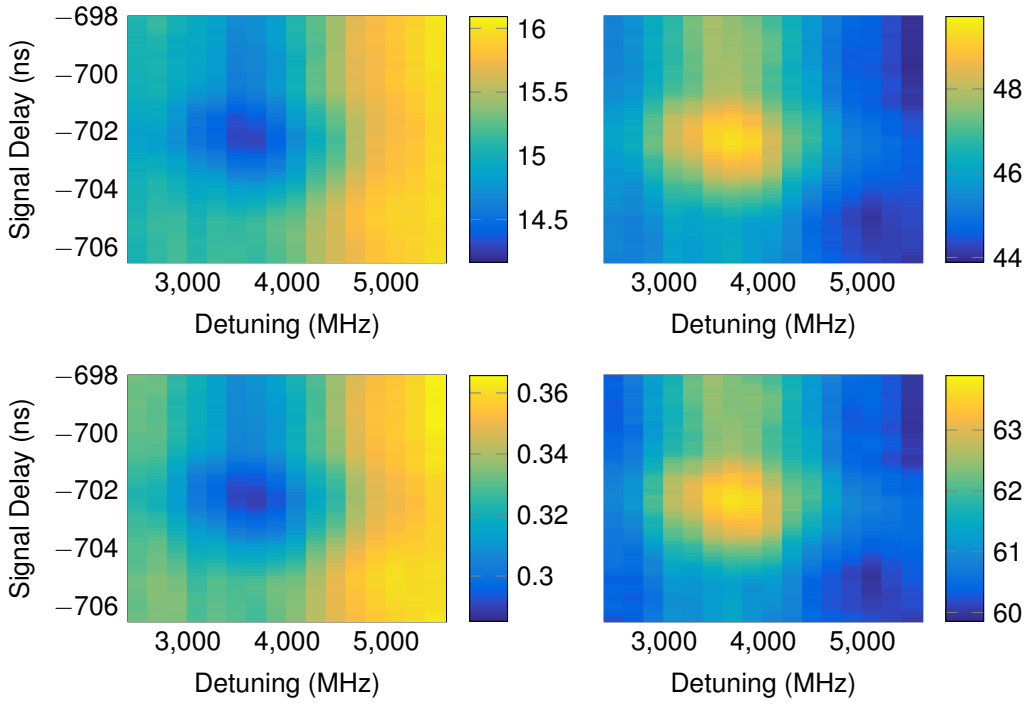

Figure 7.3.1: Experimental switching data. The signal power is plotted here. The top left is the power of the drop port of the resonator. The top right data is the from the through-port. The bottom left plot is the ratio of the two ports. The bottom right is the total power measured, this can be used to see if the coupling changes dramatically. The avg pump power here is 800 mW peak. The pump switches light out of the cavity in this case.

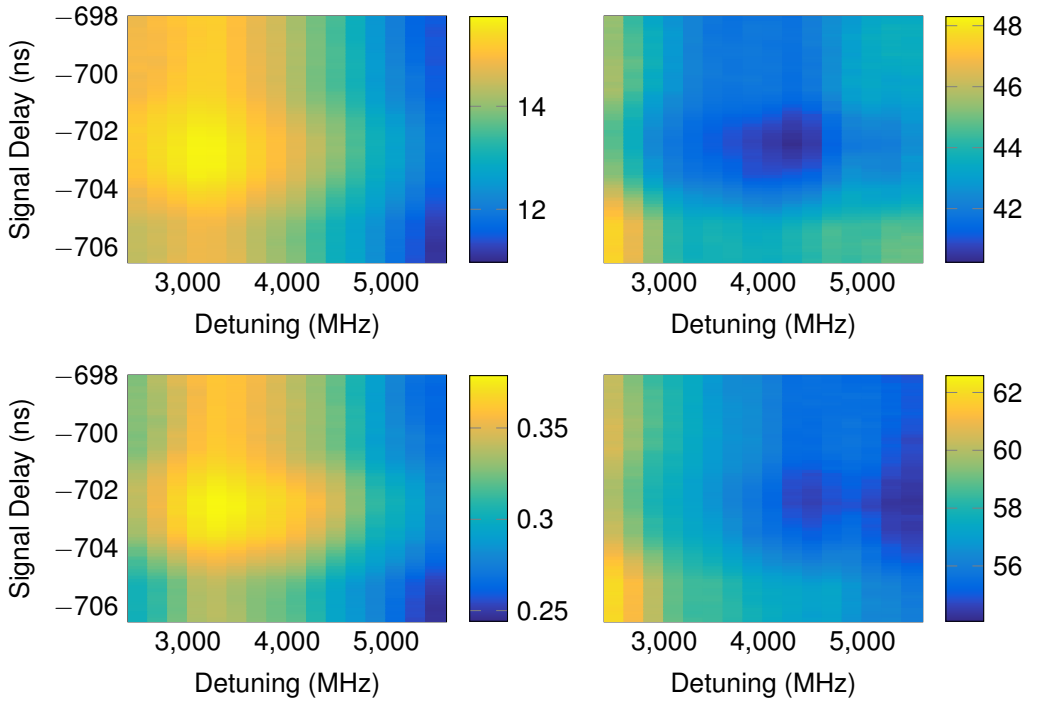

Figure 7.3.2: This is the experimental data. The top left is the power of the drop port (Port 4). The top right data is the from the port 2. The bottom left plot is the ratio of the top left to the top right. The bottom right is the total power measured, this can be used to see if the coupling changes dramatically. The avg pump power here is 5.71 mW (or 1.3 W peak), but this is before the 50/50 and the chip. Here the pump switches light into the cavity.

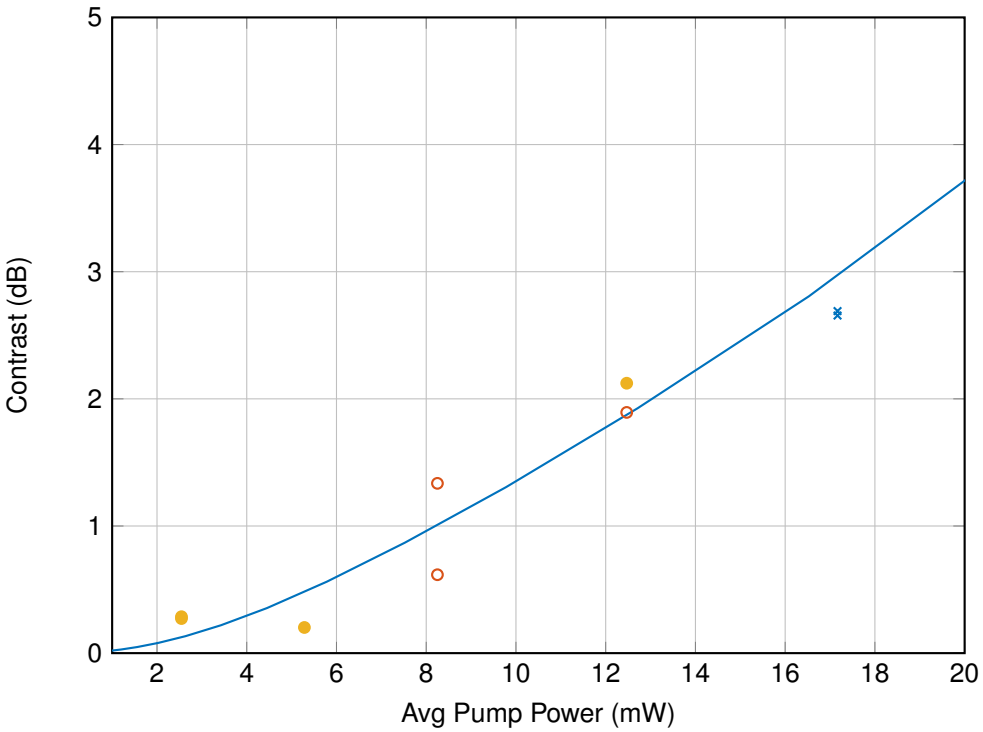

Figure 7.3.3: A comparison of the contrast measured (the ratio of the through to drop power) as a function of the average pump power. The blue line presents a simulation of the experiment.

8 Microresonators

Four-Wave Mixing

This Chapter covers a set of ring resonator nonlinear optics experiments and the device characterization to support them.

8.1 Dispersion

Dispersion is one of the most important differentiators between the ring and disk resonator devices. If we are interested in phase-matching between four independent waves, as opposed to simple cross-phase or self-phase modulation, we need a device that has a small anomalous dispersion. Only the ring devices have this because of the cross-section of the resonator. Simply put, the disk resonator is too thin, so its dispersion is decidedly normal in the C-band. While our simulations show a small anomalous dispersion in the C-band, perfect for FWM or comb-generation, we need to measure to verify this fact.

To facilitate this, our ring resonators come in a range of widths, between 1.6 μm and 2.1 μm. Simulations show that GVD is larger (more anomalous) as the width of the resonator cross-section decreases.

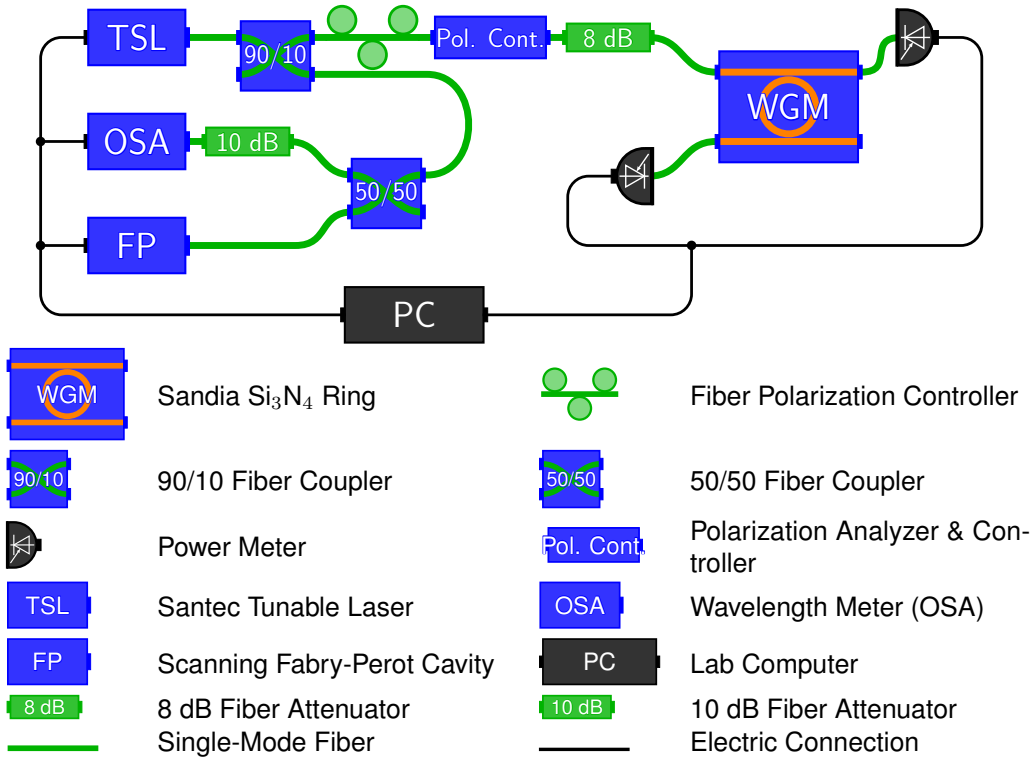

Figure 8.1.1: The optical setup used to measure the Q-factor and dispersion of the ring resonators. Measuring both the thru- and drop-port optical power during the laser sweeps allows us to calibrate out any coupling degradations.

Figure 8.1.1 shows the optical setup of the dispersion measurement. A tunable laser (usually a SANTEC TLS-210, sometimes a Pure Photonics PPCL200) is coupled into the resonator. The drop and through port is monitored by power meters to register the shape of the resonance that the laser scans across. To increase the accuracy of the measurement of the frequency of the laser, we rely on a scanning Fourier-transform OSA (a Thorlabs OSA203C) and a scanning Fabry-Pérot interferometer. The whole sweep is computer controlled as shown in Figure 8.1.2, where the control signals are mapped out. In this instance, the experiment is managed by a Linux computer which controls the laser and a power meter via a USB-GPIB controller. Another power meter is controlled directly via USB. A 300 MHz oscil-

loscope (Rigol DS1302CA) is used as a data acquisition system to interface with the scanning interferometer. A specialized function generator outputs a saw tooth pulse to drive a piezo to scan the interferometer and amplify the photo current. The oscilloscope triggers from the sawtooth and the computer saves the trace.

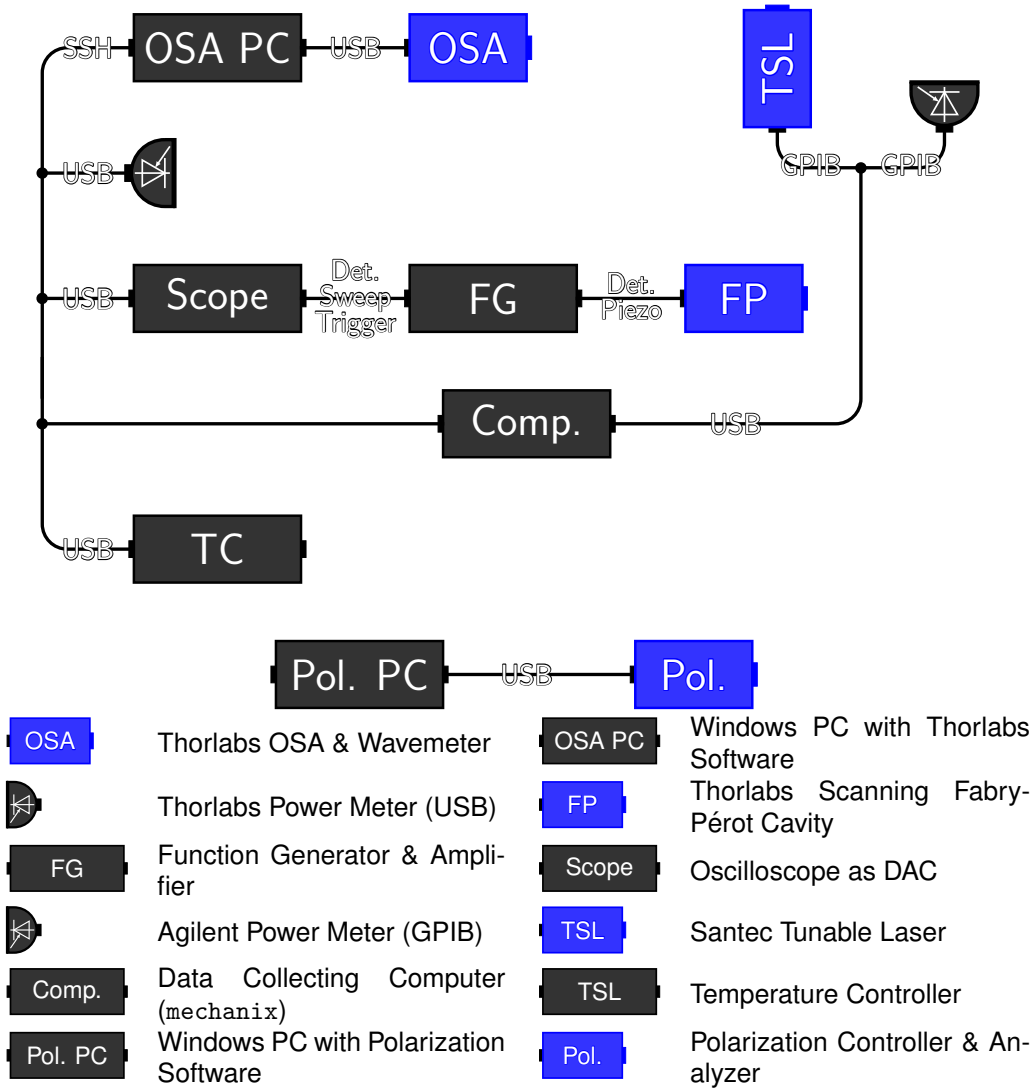

Figure 8.1.2: The electrical compliment to the optical setup shown in Figure 8.1.1. Most instruments directly interfaced with the measurement computer. Later versions of the data acquisition software we wrote would eliminate some of the extra computers.

Finally a completely independent system is used to control the polarization controller. Despite using a manual fiber polarization controller to set the chip input polarization, the effective waveplates respesented by each paddle depends on wavelength because the retardance of the fiber is wavelength dependent. Because the resonator supports two distinct polarization modes, the gradual change in polarization over the 100 nm laser sweep can change the results of the scan. For this we use an active polarization controller (Thorlabs DPC) which locks the polarization as the laser sweeps.

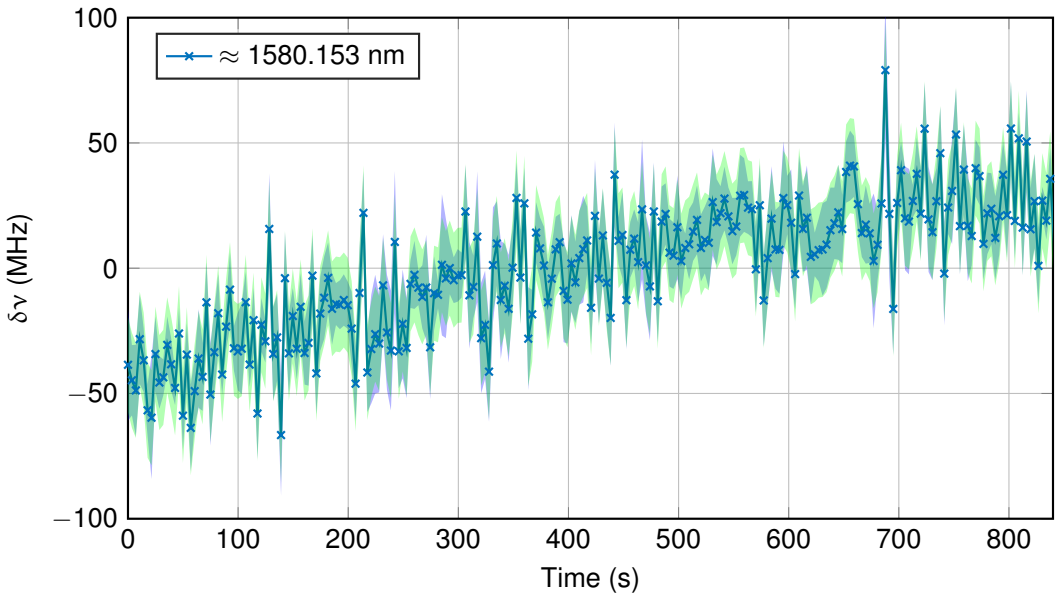

Figure 8.1.3: This plot shows the difference in frequency measure with our wavemeter as a function of time for the SANTEC TLS-210 after the initial warm up and stabilization period.

To reconstruct the dispersion, we first find the peak of the power meter traces. We then reconstruct the relative frequency of the trace from the interferometer data. Because this device (Thorlabs SA200-12B) has an FSR of 1.5 GHz (and a Finesse of over 200), as the laser scans in steps of 200 to 500 MHz, we can reconstruct the

relative frequency of the measurement. To compare the individual resonance traces to each other, we calibrate the initial and final points of these relative traces with the scanning OSAs wavemeter function. One key to good performance is good laser frequency stability, as shown in Figure 8.1.3.

The central frequency of a resonant mode depends on the geometry of the resonator and its effective index. This effective index depends on both the bulk material properties and a contribution from the confinement of the light and its interaction with the material boundary between the guiding feature and the cladding. We tune the dispersion of the device by adjusting the geometry as described earlier. If we were to expand out the resonance locations, where ν_m is the frequency of the m-th resonator mode, around a central mode ν_0, the mode of the resonator can be expressed as:

$$\nu_l \approx \nu_0 + D_1 l + \frac{D_2}{2} l^2 + ..., \tag{8.1.1}$$

where $l = m - m_0$, the difference in mode number from the central point of the expansion. The first term approximates the cavity FSR as:

$$D_1 = \Delta\nu_{\mathrm{FSR}} = \frac{c}{R n_g}, \tag{8.1.2}$$

where R is the ring radius. D_2 is the group velocity dispersion term. If it is positive, we have anomalous GVD around the central wavelength. Figure 8.1.4 is a plot of this dispersion for a chip with a cross-section of 2.1 μm width and 1.6 μm with a height of 750 nm. The D_2 of the thinner (thicker) device is 1.8 MHz (606 kHz) which agrees well with the simulated values of 2.04 MHz (1.04 MHz). Comparing the dispersion parameter,

$$\beta_2 = -\frac{D_2}{v_g \Delta\omega_{\mathrm{FSR}}^2}, \tag{8.1.3}$$

of the rings to that of fiber yields similar values. The rings range from -13.2 ps^2/km to -39.2 ps^2/km while standard SMF is -23 ps^2/km in the C-band.

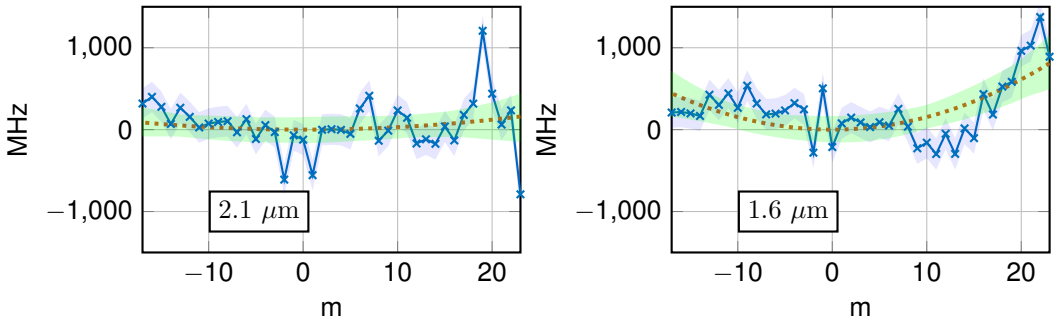

Figure 8.1.4: Experimental measurements of the dispersion for two different cross-sectional widths of ring resonator.

8.2 Phase-Sensitive Amplification

By carefully tailoring the dispersion of $\chi^{(3)}$ on-chip resonators, compact, scalable systems for a whole host of nonlinear parametric processes have been demonstrated. From photon-pair generation to octave spanning frequency combs, these systems harness chaotic phase-sensitive FWM processes.

In this section, we attempt to experimentally probe some of these features. We propose a system which uses a RF electro-optic modulator (EOM)-based frequency comb to probe and pump 3 resonator comb lines directly. As these 3 lines are generated from a single laser and co-propagate in the fiber, they maintain a consistent phase relationship between themselves. By adjusting the phase of the central line relative to the others, the phase-sensitive properties of the system can be probed. [97].

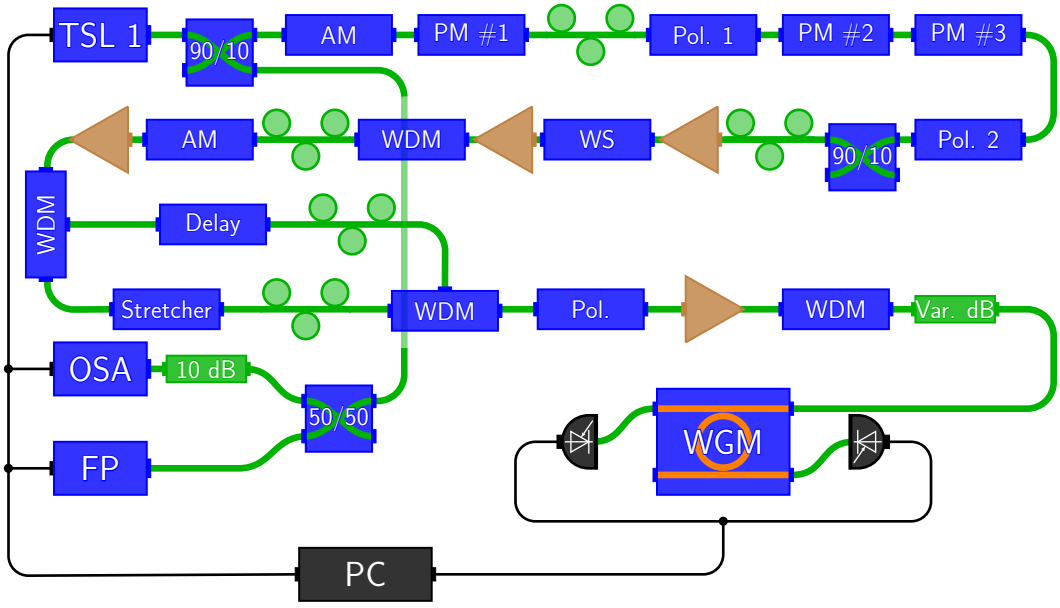

Figure 8.2.1: The experimental setup used to probe the phase-sensitivity of the ring resonator.

The final, most mature experimental setup is shown in Figure 8.2.1. This setup can be divided into two parts. The first step is to generate the frequency comb via sideband generation. This is followed by the shaping and tuning of the lines.

In order to seed 3 adjacent resonances of the ring resonator, we need a RF generated frequency comb that has significant power across at least 2 FSRs ($2 \times 218\,\text{GHz}$) of the ring resonator cavity. Our LN modulations and the associated RF amplifiers that drive them set the maximum spacing of the comb generated via sideband generation to 20 GHz. This means we need to generate a comb of sufficient width and intensity such that there is sufficient optical power in the resulting 3 modes to seed the EDFAs that set the final input laser powers. To do this a series of specialized phase and amplitude modulators designed to handle 33 to 35 dBm (27 dBm is typical) of RF power are driven by a signal synthesized by a 20-GHz sweep signal generator.

A commercial OAWG device (Finisar WaveShaper) is used to manipulate the spectral components of the resulting light. We filter out all generated sidebands except the 3 we are interested in for driving the resonator. We can also set their intensity and phase at this point to ensure the proper setup in the resonator.

8.2.1 RF Comb

The RF generated comb proved key to the overall performance of the system. Polarization instability plagued the system. Figure 8.2.2 shows the final comb used in this experiment.

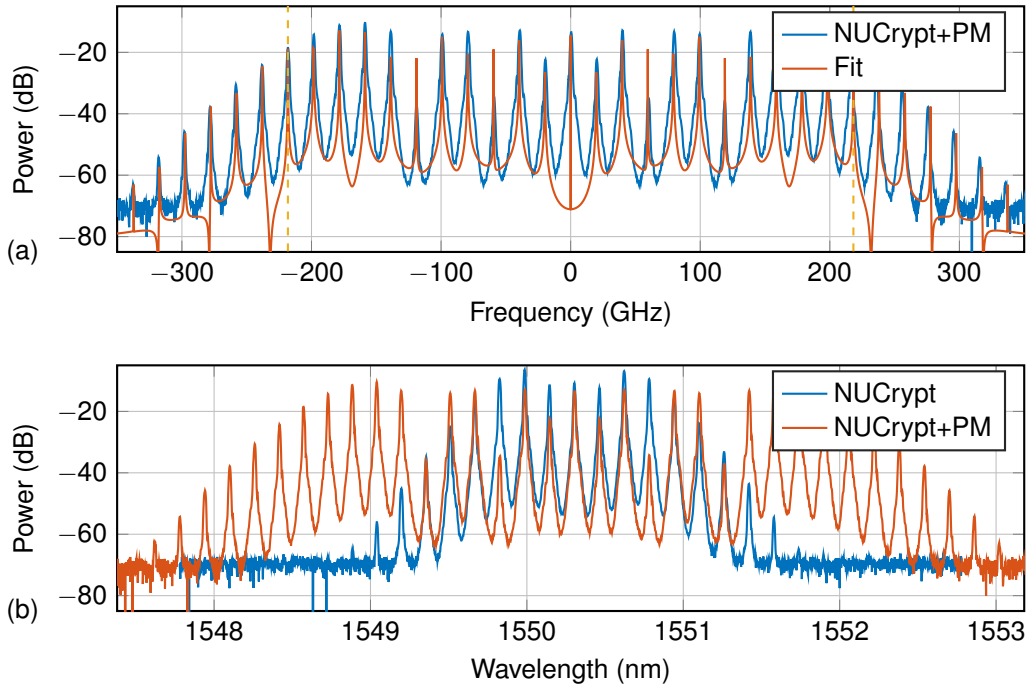

Figure 8.2.2: (a, b) Low V_π model with 30 dBm of RF power and computed spectrum based (shown in (a)). (b) shows the multiple stages of modulation needed to generate this comb.

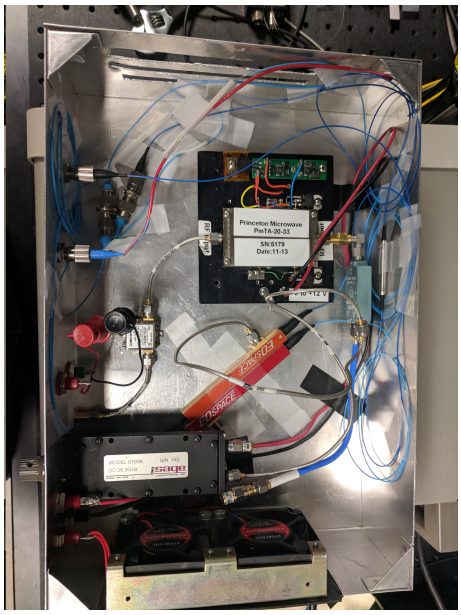

Figure 8.2.3: The extra modulators with associated RF electronics used to expand the comb.

8.2.2 Four Wave Mixing

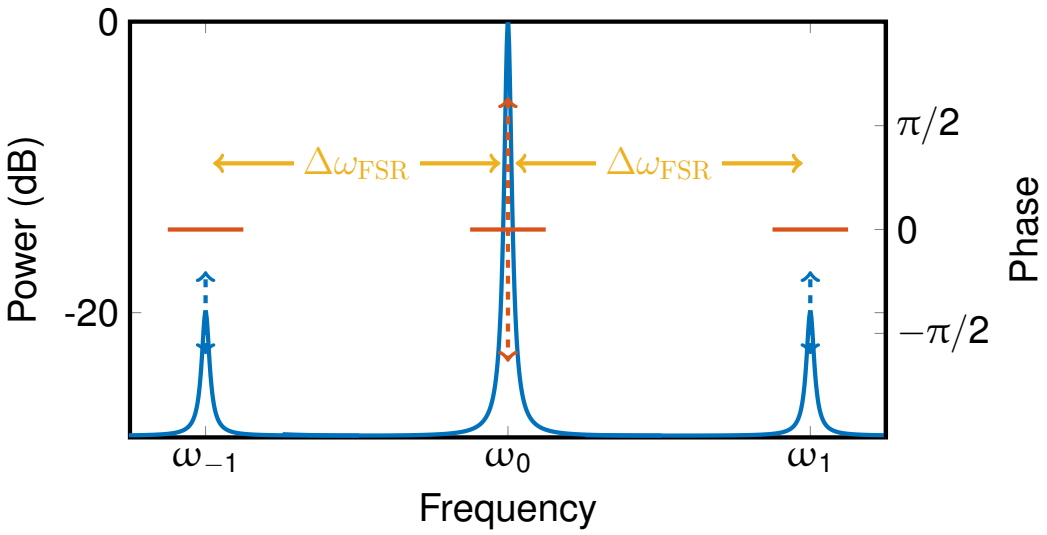

Figure 8.2.4: Input into the WGM. Each of the three lines is at a cavity resonance. We can vary the phase of the center wave (pump) independently. We can also vary the power of each line individually, but operate in the regime where the pump is roughly 10 or 20 dB greater than the two driven side-lobes which are equal in power.

Preliminary results searching for FWM in the silicon nitride ring resonator have shown some promise. Due to system stability issues, only a transient look into this was seen. We look at the 5th resonator cavity line detunned to the blue of the central pump (near 1550 nm) on a detector. As we sweep the phase of middle of the 3 phase-locked lines at a rate of 5 Hz, we see modulation of the fifth resonator cavity line at that rate. We present this as preliminary evidence of phase-sensitive FWM in the resonator system.

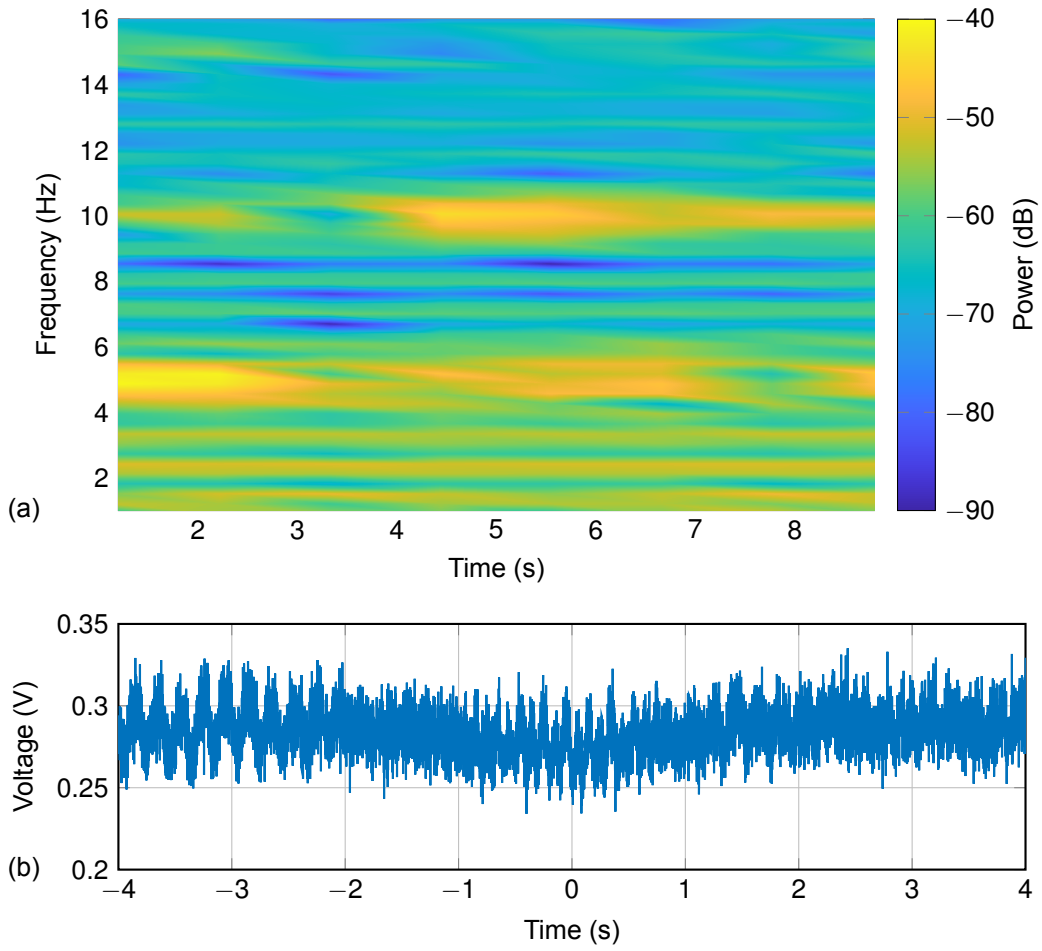

Figure 8.2.5: (a) Spectrogram and (b) time trace of preliminary phase-sensitivity due to FWM.

Further study of this signal was compromised. With improved stability of the input laser lines, we hoped to directly measure and better characterize this effect. However, probing the chip at higher powers resulted in a burned v-groove array fiber. Due to previous damage of the chip, it was impossible to continue using this combination of fiber array and resonator.

After an exhaustive search of our stock of Sandia supplied chips and fiber arrays, suitable candidates were found. However, further study of these chips showed lower

Q-factors. With the increased pump power this required, phase-sensitive FWM effects are observed in the fiber leading into the chip. These mask any effect from the chip itself.

9 Conclusions & Future Directions

The future of quantum optics and integrated photonics is a bright one. It is hard to anticipate how this technology will be leveraged in the future but if we had to predict, we are still in the infancy of the exponential growth that the field is undergoing.

9.1 Lithium Niobate on Silicon

LN is an excellent $\chi^{(2)}$ optical material. Prof. Fathpour's group from CREOL have demonstrated a LN on silicon chip which is strip loaded with Si_3N_4 for both nonlinear optics [22, 72] and EOM at high speeds [98]. It should be noted that this design allows for cascaded second and third-order effects [99]. Our collaboration with this group to precisely measure the optical nonlinear coefficient and QPM grating quality is ongoing. Others have shown LN WGs directly on insulator [23].

One possible application for these waveguides is for our mode-selective receiver design as discussed in Chapter 3. It may be possible to integrate the waveguide with filtering elements directly. simplifying the experiment. If a resonator-based frequency comb is combined with a OAWG, it may be possible to implement the whole receiver in a robust few-chip design.

9.2 Phase Sensitive Resonator Experiment

The experiments in Chapter 8 are limited by the Q-factor of the resonator. Rings with cross-sections very similar to ours (1.5 μm wide, 730 nm tall) have been demonstrated with loaded Q-factors over 600,000 [100]. This would lower our required pump power by roughly 2 orders of magnitude, eliminating the FWM from the SMF which dominated any effects from the resonator itself.

9.3 Photon Pair Sources

Chapter 4 makes the case for the use of a:Si-H for photon-pair generation. While the experiment discussed was done in a WG, we also tested resonator devices. These rudimentary rings suffered from high scattering loss and were not phase-matched for FWM in any band we tested. However, in principle, these limitations can be overcome.

In our quest for novel devices, we propose to combine the generation of pairs in a ring with filters to act as both pump suppression and signal/idler demultiplexing. Figure 9.3.1 shows a schematic for a proposed design. While all the technical details are outside the scope of this work, we believe it is possible to engineer the required 100 dB of pump suppression by utilizing edge coupling to reduce inter-chip pump scattering and utilizing 7 or more stages of coupled ring resonator filters [101]. The filter FSR has to be roughly 3/2 that of the generation ring. Silicon nitride or silicon are also viable materials for this design.

With this first-step of integration, this chip can be used as just one element of a larger scheme, or copied for a multiplexed source setup.

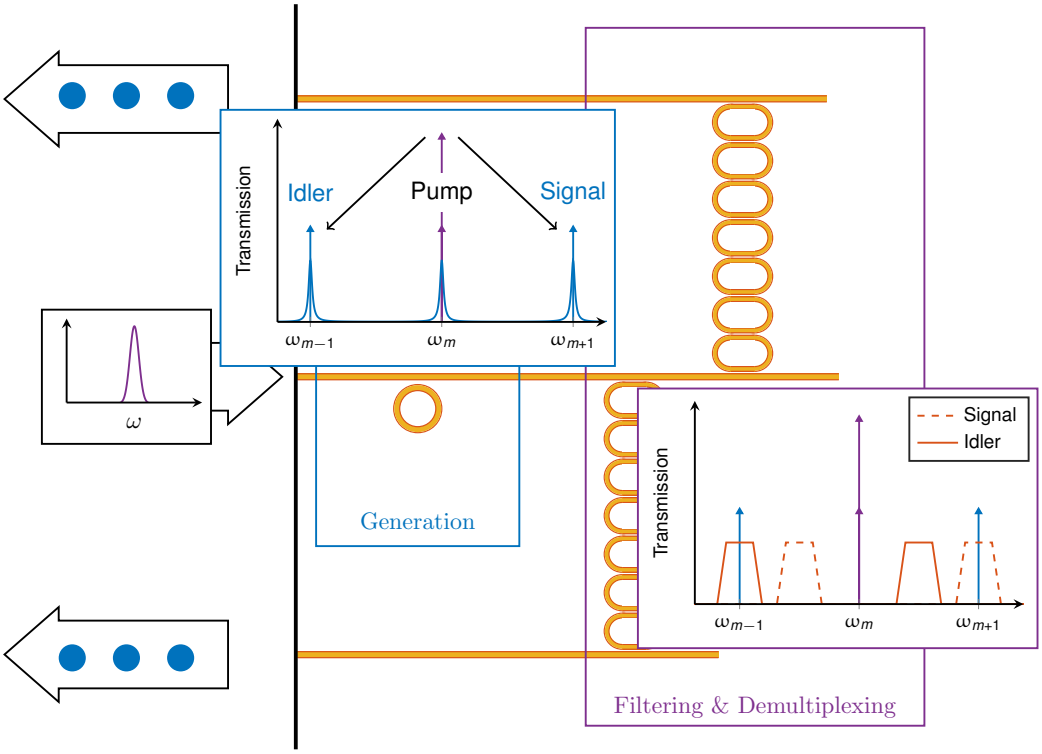

Figure 9.3.1: A conceptual diagram of the proposed chip which will generate, filter and demultiplex photon pairs. On-chip heaters are needed to match the resonator spectra across the individual elements.

References

[1] G. P. Agrawal, *Nonlinear Fiber Optics* (Elsevier Pte Ltd., 2009).

[2] E. Temprana, E. Myslivets, L. Liu, V. Ataie, N. Alic, and S. Radic, "Overcoming Kerr-induced capacity limit in optical fiber transmission," Science **348**, 1445–1448 (2015).

[3] F. N. Baynes, F. Quinlan, T. M. Fortier, Q. Zhou, A. Beling, J. C. Campbell, and S. A. Diddams, "Attosecond timing in optical-to-electrical conversion," Optica **2**, 141–146 (2015).

[4] J. P. Gordon, H. J. Zeiger, and C. H. Townes, "The maser-new type of microwave amplifier, frequency standard, and spectrometer," Physical Review **99**, 1264–1274 (1955).

[5] P. a. Franken, a. E. Hill, C. W. Peters, and G. Weinreich, "Generation of optical harmonics," Physical Review Letters **7**, 118–119 (1961).

[6] R. W. Boyd, *Nonlinear Optics* (Academic Press, 2008), 3rd ed.

[7] W. Bogaerts, P. De Heyn, T. Van Vaerenbergh, K. De Vos, S. K. Selvaraja, T. Claes, P. Dumon, P. Bienstman, D. Van Thourhout, and R. Baets, "Silicon microring resonators," Laser Photonics Reviews **6**, 47–73 (2012).

[8] V. B. Braginsky, M. L. Gorodetsky, and V. S. Ilchenko, "Quality-factor and nonlinear properties of optical whispering-gallery modes," Physics Letters A **137**, 393–397 (1989).

[9] M. L. Gorodetsky, A. A. Savchenkov, and V. S. Ilchenko, "Ultimate Q of optical microsphere resonators." Optics Letters **21**, 453–455 (1996).

[10] N. Vukovic, N. Healy, P. Mehta, T. D. Day, P. J. A. Sazio, J. V. Badding, and A. C. Peacock, "Thermal nonlinearity in silicon microcylindrical resonators," Applied Physics Letters **100** (2012).

[11] C. Wang, M. J. Burek, Z. Lin, H. A. Atikian, V. Venkataraman, I.-C. Huang, P. Stark, and M. Lončar, "Integrated high quality factor lithium niobate microdisk resonators," Optics Express **22**, 30924 (2014).

[12] K. Nozaki, T. Tanabe, A. Shinya, S. Matsuo, T. Sato, H. Taniyama, and M. Notomi, "Sub-femtojoule all-optical switching using a photonic-crystal nanocavity," Nature Photonics **4**, 477–483 (2010).

[13] R. M. Camacho, "Entangled photon generation using four-wave mixing in azimuthally symmetric microresonators Abstract :," Optics Express **20**, 1470–1483 (2012).

[14] X. Zeng and M. A. Popović, "Triply-resonant micro-optical parametric oscillators based on Kerr nonlinearity: nonlinear loss, unequal resonance-port couplings, and coupled-cavity implementations," ArXiv **1310**, 21 (2013).

[15] D. V. Strekalov, A. S. Kowligy, V. G. Velev, G. S. Kanter, P. Kumar, and Y.-P. Huang, "Phase matching for the optical frequency conversion processes in whispering gallery mode resonators," Journal of Modern Optics pp. 1–14 (2015).

[16] Y.-P. Huang and P. Kumar, "Mode-resolved photon counting via cascaded quantum frequency conversion." Optics Letters **38**, 468–70 (2013).

[17] Y.-P. Huang, V. G. Velev, and P. Kumar, "Quantum frequency conversion in nonlinear microcavities." Optics Letters **38**, 2119–21 (2013).

[18] Q. Li, M. Davanço, and K. Srinivasan, "Efficient and low-noise single-photon-level frequency conversion interfaces using silicon nanophotonics," ArXiv pp. 1–22 (2015).

[19] S. B. Papp, P. Del'Haye, and S. A. Diddams, "Parametric seeding of a microresonator optical frequency comb," Optics express **21**, 17615–17624 (2013).

[20] R. P. Feynman, "Quantum Mechanical Computers 1," Optics News **11**, 11–20 (1985).

[21] H. J. Kimble, "The quantum internet." Nature **453**, 1023–1030 (2008).

[22] A. Rao, M. Malinowski, A. Honardoost, J. R. Talukder, P. Rabiei, P. Delfyett, and S. Fathpour, "Second-harmonic generation in periodically-poled thin film lithium niobate wafer-bonded on silicon," Optics Express **24**, 29941 (2016).

[23] C. Wang, X. Xiong, N. Andrade, V. Venkataraman, X.-F. Ren, G.-C. Guo, and M. Lončar, "Second harmonic generation in nano-structured thin-film lithium niobate waveguides," Optics Express **25**, 6963 (2017).

[24] M. Zhang, C. Wang, R. Cheng, A. Shams-Ansari, and M. Lončar, "Monolithic ultra-high-Q lithium niobate microring resonator," Optica **4**, 1536 (2017).

[25] Y. Okawachi, K. Saha, J. S. Levy, Y. H. Wen, M. Lipson, and A. L. Gaeta, "Octave-spanning frequency comb generation in a silicon nitride chip." Optics Letters **36**, 3398–3400 (2011).

[26] E. S. Hosseini, S. Yegnanarayanan, A. H. Atabaki, M. Soltani, and A. Adibi, "High quality planar silicon nitride microdisk resonators for integrated photonics in the visible wavelength range." Optics Express **17**, 14543–14551 (2009).

[27] K. Ikeda, R. E. Saperstein, N. Alic, and Y. Fainman, "Thermal and Kerr nonlinear properties of plasma-deposited silicon nitride/ silicon dioxide waveguides." Optics Express **16**, 12987–94 (2008).

[28] J. E. Sharping, K. F. Lee, M. A. Foster, A. C. Turner, B. S. Schmidt, M. Lipson, A. L. Gaeta, and P. Kumar, "Generation of correlated photons in nanoscale silicon waveguides." Optics Express **14**, 12388–93 (2006).

[29] K.-I. Harada, H. Takesue, H. Fukuda, T. Tsuchizawa, T. Watanabe, K. Yamada, Y. Tokura, and S.-i. Itabashi, "Generation of high-purity entangled photon pairs using silicon wire waveguide." Optics Express **16**, 20368–20373 (2008).

[30] K.-I. Harada, H. Takesue, H. Fukuda, T. Tsuchizawa, T. Watanabe, K. Yamada, Y. Tokura, and S.-I. Itabashi, "Frequency and polarization characteristics of correlated photon-pair generation using a silicon wire waveguide," IEEE Journal of Selected Topics in Quantum Electronics **16**, 325–331 (2010).

[31] K.-Y. Wang and A. C. Foster, "Ultralow power continuous-wave frequency conversion in hydrogenated amorphous silicon waveguides." Optics Letters **37**, 1331–3 (2012).

[32] J. Matres, G. C. Ballesteros, P. Gautier, J.-M. Fédéli, J. Martí, and C. J. Oton, "High nonlinear figure-of-merit amorphous silicon waveguides." Optics Express **21**, 3932–40 (2013).

[33] C. Grillet, L. Carletti, C. Monat, P. Grosse, B. Ben Bakir, S. Menezo, J. M.

Fedeli, and D. J. Moss, "Amorphous silicon nanowires combining high nonlinearity, FOM and optical stability," Optics Express **20**, 22609 (2012).

[34] H. Sun, K.-Y. Wang, and A. C. Foster, "Pump-degenerate phase-sensitive amplification in amorphous silicon waveguides," Optics Letters **42**, 3590 (2017).

[35] J. S. Pelc, K. Rivoire, S. Vo, C. Santori, D. A. Fattal, and R. G. Beausoleil, "Picosecond all-optical switching in hydrogenated amorphous silicon microring resonators." Optics Express **22**, 3797–810 (2014).

[36] K.-Y. Wang, V. G. Velev, K. F. Lee, A. S. Kowligy, P. Kumar, M. A. Foster, A. C. Foster, and Y.-P. Huang, "Multichannel photon-pair generation using hydrogenated amorphous silicon waveguides," Optics Letters **39**, 914–917 (2014).

[37] R. P. Feynman, R. B. Leighton, and M. Sands, *The Feynman Lectures on Physics*, vol. II: Mainly Electromagnetism and Matter (Basic Books, 1964).

[38] D. J. Griffiths, *Introduction to Electrodynamics* (Pearson Benjamin Cummings, 2008).

[39] J. D. Jackson, *Classical Electrodynamics* (Wiley, 1999), 3rd ed.

[40] M. Oxborrow, "Traceable 2-D Finite-Element Simulation of the Whispering-Gallery Modes of Axisymmetric Electromagnetic Resonators," IEEE Transactions on Microwave Theory and Techniques **55**, 1209–1218 (2007).

[41] K. Homma, D. Habs, and T. Tajima, "Probing the semi-macroscopic vacuum by higher-harmonic generation under focused intense laser fields," Applied Physics B: Lasers and Optics **106**, 229–240 (2012).

[42] O. J. Pike, F. Mackenroth, E. G. Hill, and S. J. Rose, "A photon–photon collider in a vacuum hohlraum," Nature Photonics **8**, 434–436 (2014).

[43] R. Hunsperger, *Integrated Optics: Theory and Technology*, vol. 33 of *Springer Series in Optical Sciences* (Springer-Verlag, 1983).

[44] P. Kwiat, K. Mattle, H. Weinfurter, A. Zeilinger, A. Sergienko, and Y. Shih, "New high-intensity source of polarization-entangled photon pairs," Physical Review Letters **75**, 4337–4341 (1995).

[45] Q. Lin, F. Yaman, and G. P. Agrawal, "Photon-pair generation in optical fibers through four-wave mixing: Role of Raman scattering and pump polarization," Physical Review A **75**, 1–20 (2007).

[46] P. Kumar, "Quantum frequency conversion." Optics Letters **15**, 1476–1478 (1990).

[47] M. M. Fejer, G. A. Magel, D. H. Jundt, and R. L. Byer, "Quasi-phase-matched second harmonic generation: tuning and tolerances," IEEE Journal of Quantum Electronics **28**, 2631–2654 (1992).

[48] D. Chang, C. Langrock, Y.-w. Lin, C. R. Phillips, C. V. Bennett, and M. M. Fejer, "Complex-transfer-function analysis of optical-frequency converters," Optics Letters **39**, 5106–5109 (2014).

[49] R. Remez and A. Arie, "Super-narrow frequency conversion," Optica **2**, 472–475 (2015).

[50] V. G. Velev, C. Langrock, P. Kumar, M. M. Fejer, and Y.-P. Huang, "Selective Manipulation of Overlapping Quantum Modes," in "IEEE Summer Topicals Meeting," (2014), p. WD4.

[51] L. Rayleigh, *Theory of Sound* (MacMillan, 1878), 1st ed.

[52] P. Del'Haye, A. Schliesser, O. Arcizet, T. Wilken, R. Holzwarth, and T. J. Kippenberg, "Optical frequency comb generation from a monolithic microresonator." Nature **450**, 1214–1217 (2007).

[53] L. M. Duan and H. J. Kimble, "Scalable photonic quantum computation through cavity-assisted interactions," Physical Review Letters **92**, 127902–1 (2004).

[54] S. F. Preble, Q. Xu, and M. Lipson, "Changing the colour of light in a silicon resonator," Nature Photonics **1**, 293–296 (2007).

[55] A. Arbabi and L. L. Goddard, "Dynamics of self-heating in microring resonators," IEEE Photonics Journal **4**, 1702–1711 (2012).

[56] I. S. Grudinin, H. Lee, T. Chen, and K. J. Vahala, "Compensation of thermal nonlinearity effect in optical resonators." Optics Express **19**, 7365–7372 (2011).

[57] V. G. Velev, P. Kumar, and Y.-P. Huang, "Natural Phase Matching in Microdisk Cavities," in "CLEO 2014," (2014), p. JTh2A.72.

[58] M. Borselli, T. J. Johnson, and O. Painter, "Beyond the Rayleigh scattering limit in high-Q silicon microdisks: theory and experiment." Optics Express **13**, 1515–1530 (2005).

[59] J. E. Heebner, T. C. Bond, and J. S. Kallman, "Generalized formulation for performance degradations due to bending and edge scattering loss in microdisk resonators." Optics express **15**, 4452–73 (2007).

[60] H. Lee, T. Chen, J. Li, K. Y. Yang, S. Jeon, O. Painter, and K. J. Vahala, "Chemically etched ultrahigh-Q wedge-resonator on a silicon chip," Nature Photonics **6**, 369–373 (2012).

[61] P. S. Kuo, J. Bravo-Abad, and G. S. Solomon, "Second-harmonic generation using 4-quasi-phasematching in a GaAs whispering-gallery-mode microcavity." Nature Communications **5**, 3109 (2014).

[62] A. S. Kowligy, P. Manurkar, N. V. Corzo, V. G. Velev, M. Silver, R. P. Scott, S. J. B. Yoo, P. Kumar, G. S. Kanter, and Y.-p. Huang, "Quantum Optical Arbitrary Waveform Manipulation and Measurement in Real Time," Optics Express **22**, 1–8 (2014).

[63] P. Manurkar, N. Jain, M. Silver, Y.-P. Huang, C. Langrock, M. M. Fejer, P. Kumar, and G. S. Kanter, "Multidimensional mode-separable frequency conversion for high-speed quantum communication," Optica **3**, 1300 (2016).

[64] D. V. Reddy, M. G. Raymer, C. J. McKinstrie, L. Mejling, and K. Rottwitt, "Temporal mode selectivity by frequency conversion in second-order nonlinear optical waveguides," Optics Express **21**, 13840–13863 (2013).

[65] B. Brecht, D. V. Reddy, C. Silberhorn, and M. G. Raymer, "Photon temporal modes: a complete framework for quantum information science," ArXiv pp. 1–13 (2015).

[66] C. Polycarpou, K. N. Cassemiro, G. Venturi, a. Zavatta, and M. Bellini, "Adaptive detection of arbitrarily shaped ultrashort quantum light states," Physical Review Letters **109**, 1–5 (2012).

[67] N. N. Oza, J. B. Altepeter, M. Medic, E. R. Jeffrey, and P. Kumar, "Entangled photon polarimetry," Optics Express **19**, 26011–26016 (2011).

[68] J. Huang and P. Kumar, "Observation of quantum frequency conversion," Physical Review Letters **68**, 2153–2156 (1992).

[69] J. Chen, A. J. Pearlman, A. Ling, J. Fan, and A. L. Migdall, "A versatile waveguide source of photon pairs for chip-scale quantum information processing," Optics Express **17**, 6727 (2009).

[70] K. R. Parameswaran, R. K. Route, J. R. Kurz, R. V. Roussev, M. M. Fejer, and M. Fujimura, "Highly efficient second-harmonic generation in buried waveguides formed by annealed and reverse proton exchange in periodically poled lithium niobate," Optics Letters **27**, 179 (2002).

[71] Q. Zhang, X. Xie, H. Takesue, S. W. Nam, C. Langrock, M. M. Fejer, and Y. Yamamoto, "Correlated photon-pair generation in reverse-proton-exchange PPLN waveguides with integrated mode demultiplexer at 10 GHz clock," Optics Express **15**, 10288 (2007).

[72] A. Rao, J. Chiles, S. Khan, S. Toroghi, M. Malinowski, G. F. Camacho-Gonz??lez, and S. Fathpour, "Second-harmonic generation in single-mode integrated waveguides based on mode-shape modulation," Applied Physics Letters **110** (2017).

[73] C. Wang, M. Zhang, B. Stern, M. Lipson, and M. Lončar, "Nanophotonic lithium niobate electro-optic modulators," Optics Express **26**, 1547 (2018).

[74] T. Yamamoto, T. Komukai, K. Suzuki, and A. Takada, "Multicarrier light source with flattened spectrum using phase modulators and dispersion medium," Journal of Lightwave Technology **27**, 4297–4305 (2009).

[75] R. Wu, V. R. Supradeepa, C. M. Long, D. E. Leaird, and A. M. Weiner, "Generation of very flat optical frequency combs from continuous-wave lasers using

cascaded intensity and phase modulators driven by tailored radio frequency waveforms." Optics letters **35**, 3234–3236 (2010).

[76] F. M. Soares, N. K. Fontaine, R. P. Scott, J. H. Baek, X. Zhou, T. Su, S. Cheung, Y. Wang, C. Junesand, S. Lourdudoss, K. Y. Liou, R. a. Hamm, W. Wang, B. Patel, L. a. Gruezke, W. T. Tsang, J. P. Heritage, and S. J. B. Yoo, "Monolithic InP 100-Channel x 10-GHz Device for Optical Arbitrary Waveform Generation," IEEE Photonics Journal **3**, 975–985 (2011).

[77] R. P. Scott, N. K. Fontaine, J. P. Heritage, and S. J. B. Yoo, "Dynamic optical arbitrary waveform generation and measurement," Optics Express **18**, 18655–18670 (2010).

[78] N. K. Fontaine, R. P. Scott, and S. Yoo, "Dynamic optical arbitrary waveform generation and detection in InP photonic integrated circuits for Tb/s optical communications," Optics Communications **284**, 3693–3705 (2011).

[79] S. S. Rao, *Engineering Optimization: Theory and Practice* (Wiley, 2009), 4th ed.

[80] Y.-P. Huang and P. Kumar, "Distilling quantum entanglement via mode-matched filtering," Physical Review A - Atomic, Molecular, and Optical Physics **84**, 1–5 (2011).

[81] S. Clemmen, A. Perret, S. K. Selvaraja, W. Bogaerts, D. Van Thourhout, R. Baets, P. Emplit, and S. Massar, "Generation of correlated photons in hydrogenated amorphous-silicon waveguides." Optics Letters **35**, 3483–3485 (2010).

[82] R. Sun, K. McComber, J. Cheng, D. K. Sparacin, M. Beals, J. Michel, and L. C. Kimerling, "Transparent amorphous silicon channel waveguides with

silicon nitride intercladding layer," Applied Physics Letters **94** (2009).

[83] J. Cardenas, C. B. Poitras, J. T. Robinson, K. Preston, L. Chen, and M. Lipson, "Low loss etchless silicon photonic waveguides." Optics Express **17**, 4752–4757 (2009).

[84] S. X. Wang and G. S. Kanter, "Robust multiwavelength all-fiber source of polarization-entangled photons with built-in analyzer alignment signal," IEEE Journal of Selected Topics in Quantum Electronics **15**, 1733–1740 (2009).

[85] H. Takesue and K. Inoue, "1.5-Microm Band Quantum-Correlated Photon Pair Generation in Dispersion-Shifted Fiber: Suppression of Noise Photons By Cooling Fiber." Optics Express **13**, 7832–7839 (2005).

[86] W. Suh, Z. Wang, and S. Fan, "Temporal coupled-mode theory and the presence of non-orthogonal modes in lossless multimode cavities," IEEE Journal of Quantum Electronics **40**, 1511–1518 (2004).

[87] H. A. Haus, *Electromagnetic Noise and Quantum Optical Measurements* (Springer, 2000), 1st ed.

[88] M. Oxborrow, "Configuration of COMSOL Multiphysics for simulating axisymmetric dielectric resonators : explicit weak-form expressions axisymmetric electromagnetic resonators," Online pp. 1–6 (2006).

[89] K. Luke, Y. Okawachi, M. R. E. Lamont, A. L. Gaeta, and M. Lipson, "Broadband mid-infrared frequency comb generation in a Si3N4 microresonator," Optics Letters **40**, 4823 (2015).

[90] A. D. Greenwood and J.-M. Jin, "A Novel Efficient Algorithm for Scattering from a Complex BOR Using Mixed Finite Elements and Cylindrical PML," IEEE Transactions on Antennas and Propagation **47**, 620–629 (1999).

[91] M. I. Cheema and A. G. Kirk, "Accurate determination of the quality factor of axisymmetric resonators by use of a perfectly matched layer," ArXiv **1101**, 1–7 (2012).

[92] G. Priem, P. Dumon, W. Bogaerts, D. Van Thourhout, G. Morthier, and R. Baets, "Optical bistability and pulsating behaviour in Silicon-On-Insulator ring resonator structures." Optics express **13**, 9623–9628 (2005).

[93] V. R. Almeida, C. Barrios, R. R. Panepucci, M. Lipson, M. A. Foster, D. G. Ouzounov, and A. L. Gaeta, "All-optical switching on a silicon chip." Optics Letters **29**, 2867–9 (2004).

[94] Y. H. Wen, O. Kuzucu, T. Hou, M. Lipson, and A. L. Gaeta, "All-optical switching of a single resonance in silicon ring resonators." Optics Letters **36**, 1413–1415 (2011).

[95] N. N. Oza, Y.-P. Huang, and P. Kumar, "Entanglement-Preserving Photonic Switching: Full Cross-Bar Operation With Quantum Data Streams," IEEE Photonics Technology Letters **26**, 356–359 (2014).

[96] C. Manolatou, M. J. Khan, S. Fan, P. R. Villeneuve, H. a. Haus, and J. D. Joannopoulos, "Coupling of modes analysis of resonant channel add-drop filters," IEEE Journal of Quantum Electronics **35**, 1322–1331 (1999).

[97] Y. K. Chembo, "Quantum dynamics of Kerr optical frequency combs below and above threshold: Spontaneous four-wave mixing, entanglement, and squeezed states of light," Physical Review A **93**, 033820 (2016).

[98] A. Rao, A. Patil, P. Rabiei, A. Honardoost, R. DeSalvo, A. Paolella, and S. Fathpour, "High-performance and linear thin-film lithium niobate

Mach–Zehnder modulators on silicon up to 50 GHz," Optics Letters **41**, 5700 (2016).

[99] A. Honardoost, G. F. Camacho Gonzalez, S. Khan, M. Malinowski, A. Rao, J. E. Tremblay, A. Yadav, K. Richardson, M. C. Wu, and S. Fathpour, "Cascaded Integration of Optical Waveguides with Third-Order Nonlinearity with Lithium Niobate Waveguides on Silicon Substrates," IEEE Photonics Journal **10**, 1–9 (2018).

[100] A. Dutt, C. Joshi, X. Ji, J. Cardenas, Y. Okawachi, K. Luke, A. L. Gaeta, and M. Lipson, "On-chip dual-comb source for spectroscopy," Science Advances **4**, e1701858 (2018).

[101] J. R. Ong, R. Kumar, and S. Mookherjea, "Ultra-high-contrast and tunable-bandwidth filter using cascaded high-order silicon microring filters," IEEE Photonics Technology Letters **25**, 1543–1546 (2013).

[102] J. W. Eaton, D. Bateman, and S. Hauberg, *GNU Octave Manual Version 3* (Network Theory Ltd., 2008).

A | Mode Sorting Simulation Code

Chapter 3 discusses simulations for a temporal-mode sorting all-optical receiver that relies on tailored temporal pump shapes in order to select by upconversion a signal mode. The sections below are examples of the MATLAB functions that solve for the waveguide interaction direction (Sec. A.1) and the optimized pump shape (Sec. A.2). Finally we discuss quickly some notes on the computation time of these simulations in section A.3.

It should be noted that these are not the only functions that were used for the results in chapter 3, but only a subset. Specifically, these functions (along with a master script, which is not shown) specifically solve the multi-pump problem. This is the case where a single WG with a multi-peaked QPM grating is used with multiple pumps which selectively upconvert individual signal modes to dedicated frequencies. Also, supporting functions for generating signal modes, initial conditions for optimization, and processing of the data are not included.

A.1 Nonlinear Waveguide Interaction Solver Code

Listing A.1.1: Split-step fourier transform function.

```
function [Ar,As] = QFC_QPM_Solver_pNsM_v1beta(chi,t,...
Ap,As,beta,z_QPM,c_QPM,dk_QPM,a)
% Vesselin Velev - Only for Multi-Pump, Multi-Signal
```

```
% Interactions distances are in cm, times are in ps!,
% QPM vector has to be equally spaced
% The 1D solver allows width variation via a dk vector
% here a dk vector is the target phase-mismatch for
% each pump/sig pair.
% Ar = [length(t),#p,#s]
% chi             - Chi
% t               - T-vector, check shape, if error,
%                   may need to transpose
% Ap              - Pump mode vectors, Ap(n,m), where
%                   n is the size of t, and m is the
%                   # of signals
% As              - Signal mode vectors, As(n,m), where
%                   n is the size of t, and m is the
%                   # of signals
% beta            - Beta, ps/cm
% z_QPM           - Z-grid for propogation down waveguide
% c_QPM           - Quasi-phase match grating, set to 1
%                   for uniform, same size as z_QPM
% dk_QPM          - Phase-mismatch, 1 value per pump, Not
%                   a vector for width variation
% a               - Loss, in dB/cm, for the sum-frequency,
%                   a(1) and the input frequency, a(2)
% This order of variables is historical, somewhat
% <<----------------------------------------->>

nu=0;
mu=beta;
eta=chi;

a = log(10.^(a./20));    % input of a is in db/cm,
                         % converts to units for solverS

Trange = max(t)-min(t);

Nms = length(t);

for j=1:Nms
    zx(j,1)=Trange*(j-1)/Nms;
    kx(j,1)=2*pi*(j-1-0.5*Nms)/Trange;
    hjx(j,1)=(-1)^(j-1);
end
```

```
sAp = size(Ap);
sAs = size(As);

az = zeros(sAp(1),sAp(2),sAs(2));
bz = reshape(As,[sAs(1),1,sAs(2)]);

Nz = length(z_QPM);

dz = z_QPM(2) - z_QPM(1);

evolA = exp(1i*mu*repmat(kx,1,sAp(2))*dz...
    +1i*repmat(dk_QPM,sAp(1),1)*dz+a(1)*dz);
evolB = exp(1i*nu*kx*dz+a(2)*dz);

for ii = 1:Nz
    c = c_QPM(ii);
    [az,bz] = solvL(az,bz,hjx,evolA,evolB);
    [az,bz] = solvNL(az,bz,Ap,eta,dz,c);
end

Ar = az;
As = reshape(bz,sAs);
end

function [az1, bz1] = solvL(Az,Bz,hjx,evolaz,evolbz)
az1 = bsxfun(@times,fft(bsxfun(@times,...
    ifft(bsxfun(@times,Az,hjx)),evolaz)),hjx);
bz1 = bsxfun(@times,fft(bsxfun(@times,,...
    ifft(bsxfun(@times,Bz,hjx)),evolbz)),hjx);
end

function [az1, bz1] = solvNL(Az,Bz,Ap,eta,dz,c)
bzReS = repmat(Bz,1,size(Ap,2),1);
az1 = bsxfun(@times,1i*eta*Ap,bzReS*dz*c)+Az;
bz1 = Bz+sum(1i*eta*dz*conj(c)*
             bsxfun(@times,conj(Ap),Az),2);
end
```

A.2 Random Walk Pump Optimization Code

Listing A.2.1: Random walk function.

```
function [ApN_outF,Zdist,solT,P_out,Sel_out] =
opt_pNsM_v6_beta(chi,t,A,V,Ap,beta,z_QPM,c_QPM,...
dk,number_com,TargetN,steps,randStep,combSpace,sType,a)
% Vesselin Velev - last update 21.01.2017 - Only for
% Multi-Pump, Multi-Signal Interactions
% This does the walking!
% chi             - Chi
% t               - T-vector, check shape, if error,
%                   may need to transpose
% A               - Signal mode vectors, A(n,m), where
%                   n is the size of t, and m is the
%                   # of signals
% V               - Used to calculate probabilities
% Ap              - Initial guess for the pump, usually
%                   a multiple of the target modes
% beta            - Beta, ps/cm
% z_QPM           - Z-grid for propogation down waveguide
% c_QPM           - Quasi-phase match grating, set to 1
%                   for uniform, same size as z_QPM
% dk              - Phase-mismatch, 1 value per pump, Not
%                   a vector for width variation
% number_com      - Number of comb lines
% pN              - For which signal do you want a pump
%                   optimized?
% TargetN         - Stop when conversion hits how much?
% steps           - Or if that doesn't work, go how many
%                   (accepted) steps?
% randStep        - How far can I go each iteration?
% combSpace       - Spacing of comb lines in THz
% sType           - What kind of save do you want? every
%                   20 steps a seperate file (1) or
%                   overwritten (anything else)?
% a               - Loss, in dB/cm, for the sum-frequency,
%                   a(1) and the input frequency, a(2)
% This order of variables is historical, somewhat
% This version, A is normalized sum(abs(A).^2*dt), before
% it was sum(abs(A.^2))
% <<-------------------------------------->>
```

```
dt = t(2)-t(1);
sA = size(A);
prob = transpose(V(1:sA(2)).^2/(sum(V.^2)));

for k=1:sA(2)
    As(:,k) = sqrt(prob(k))*A(:,k);
end

dw = combSpace*2*pi;     % Comb line spacing, angular THz
w = linspace(-(number_com-1)/2,(number_com-1)/2,
             number_com)*dw;

Zdist = [];
Zsel = [];

numPump = size(Ap,2);
numSig = size(A,2);


c = zeros(number_com,numPump);

for ii=1:number_com
    for jj=1:numPump
        c(ii,jj) = 1/(max(t)-min(t))*dt*sum(Ap(:,jj)
                   .*exp(1i*w(ii)*t));
    end
end

Ap_recon = zeros(length(t),numPump);
for ii=1:number_com
    for jj=1:numPump
        Ap_recon(:,jj) = Ap_recon(:,jj)+c(ii,jj)
                         .*exp(-1i*w(ii)*t);
    end
end

Z = [];


fprintf(1,'<<--+--+--+--+--+--+---+␣␣␣Target␣Prob␣For
Pumps␣=␣%1.4f␣+--+--+--+--+--+-->>\n',TargetN(1));
for ii=1:numPump
```

```
    fprintf(1,'|   P%2.0d   -   S%2.0d   ',ii,ii);
end
fprintf(1,'|   Dist   | Popt# | AccR | G#   | S#   |\n');

accStep = 0;
totalStep = 0;
c_opt = c;
directions = 12;

sqrtC = 10;
sqrtCtest = 10;
l = 0;

c2_tp = zeros(number_com,numPump,directions);

ApN_opt = Ap;
TargM = [diag(prob(1:numPump))*TargetN,zeros(numPump,
                                    numSig-numPump)];

while sqrtC > 0.001 && accStep < steps

    tic;

    totalStep = totalStep+1;

    accept = 0;

    pNum = randperm(numPump);
    pNum = pNum(1:randi(numPump,1));

    Ap_tp = zeros(length(t),numPump,directions);
    for jj=1:directions

        c2_tp(:,:,jj) = c_opt;
        Ap_tp(:,:,jj) = ApN_opt;

        for kk=1:length(pNum)
            rk = randi(number_com);
            c2_tp(:,pNum(kk),jj) = c_opt(:,pNum(kk));
            c2_tp(rk,pNum(kk),jj) = c2_tp(rk,pNum(kk),jj)
                *(1+randStep(1)*(rand-0.5)*exp(1i*2*pi
                *randStep(2)*(rand-0.5)));
```

```
        Ap_tp(:,pNum(kk),jj) = t*0;

        for ii=1:number_com
            Ap_tp(:,pNum(kk),jj) =
                    Ap_tp(:,pNum(kk),jj)
                    +c2_tp(ii,pNum(kk),jj)
                    .*exp(-1i*w(ii)*t);
        end
    end
end

parfor jj=1:directions

    [Amp,~] = QFC_QPM_Solver_pNsM_v1beta(chi,t,
            Ap_tp(:,:,jj),As,beta,z_QPM,c_QPM,dk,a);

    Ploop = reshape(sum(abs(Amp).^2*dt),
                    [numPump,numSig]);

    P(:,:,jj) = Ploop;

    for ii=1:numPump
        if Ploop(ii,ii) > TargM(ii,ii)
            Ploop(ii,ii) = TargM(ii,ii);
        end
    end

    dP = (Ploop-TargM).^2;
    sqrtC_tp(jj) = sqrt(sum(sum(dP)));
end

[~,i] = min(sqrtC_tp);
Zdist = [Zdist, sqrtC_tp(i)];
Sel = diag(P(:,:,i))./sum(P(:,:,i),2);

if sqrtC_tp(i) < sqrtC
    accept = 1;
    accR(totalStep) = 1;
end

if sqrtC_tp(i) > sqrtC
```

```
    randNum = rand;
    ratio = sqrtC/sqrtC_tp(i);
    accR(totalStep) = 2;

    if randNum > ratio
        accept = 1;
        accR(totalStep) = 3;
    end
end

if accept == 1
    accStep = accStep+1;
    ApN_opt = Ap_tp(:,:,i);
    c_opt = c2_tp(:,:,i);
    sqrtC = sqrtC_tp(i);

    if sqrtCtest > sqrtC_tp(i)
        l = l+1;
        P_out(:,:,l) = P(:,:,i);
        Sel_out(:,l) = Sel;
        ApN_out(:,:,l) = ApN_opt;
        ApN_outF = ApN_opt;

        sqrtCtest = sqrtC_tp(i);
    end

    if mod(accStep,10) == 0
        t1 = num2str(TargetN);

        if sType == 1
            save(['opt_pNsM_v5_beta.',t1(3:end),'.',
            num2str(number_com),'_',...
            datestr(clock,'HH.MM.SS_dd-mmm-yyyy')
            ,'.mat']);
        else
            save(['opt_pNsM_.',t1(3:end),'.',...
            num2str(number_com),'_',....
            datestr(clock,'dd-mmm-yyyy'),'.mat']);
        end
    end
end
```

```
    for n = 1:numPump
        fprintf(1,'| %1.4f - %1.4f ',P_out(n,n,l),Sel(n));
    end
    fprintf(1,'| %1.4f | ',sqrtC_tp(i));
    for n = 1:numPump
        if n <= length(pNum)
            fprintf(1,'%1.0d%',pNum(n));
        else
            fprintf(1,' ');
        end
    end
    fprintf(1,'   | %4.0d | %4.0d | %4.0d |\n',...
        accR(totalStep),accStep,totalStep);

    solT(totalStep) = toc;
end
```

A.3 Simulation Computation Performance

Efficient code is important to any simulation project. Long computation times restrict the detail in which the parameter space of the simulation can be sampled. In this section, we discuss some straightforward code optimizations used in the the code above to reduce the execution time of a simulation.

While Matlab itself is extremely versatile and easy to use, there are fewer options for execution or algorithm optimizations compared to a more general programming language. However, some basic changes can yield a dramatic increase in performance. Above all, writing code that avoids loops to index over matrix elements is extremely important. Utilizing logical indexing or streamlining operations with functions such as `bsxfun` proved to be very effective. For large blocks of code that exist in loops, the built-in tools from the parrallel toolbox can be used. In the subsections below we outline other attempts at boosting performance and their

success.

A.3.1 Fast-Fourier Transform Speed Tests

Matlab uses the FFTW library internally to perform the FFT transform. Like most other libaries, the computation speed is significantly faster for vectors of length 2^n.

Figure A.3.1 shows the performance for the nonlinear WG solver for different time scales. Listed below are the 3 different time vector size types used in the test:

```
t1 = [512,1024,2048,4096,8192];
t2 = [501,1001,2001,4001,8001];
t3 = [500,1000,2000,4000,8000];
```

Clearly, the power-of-two length is somewhat faster than the powers of ten case. Both are significantly faster than `t2`, despite the fact that the values in `t2` are not primes. It should be noted that the improvement in performance comes only from the calls to the functions `fft` and `ifft` inside the main function.

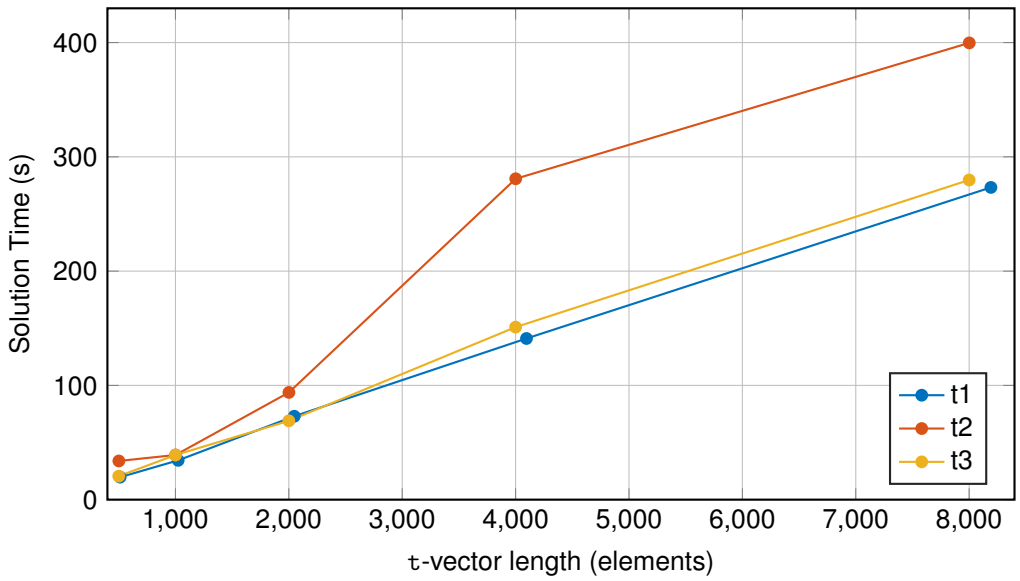

Figure A.3.1: Matlab uses the FFTW library, and it is optimized for power of 2 computations. The propogation code executes fastest with a time (and optical signals) with a length that is a power of 2.

A.3.2 Graphics Processing Unit Computation Testing

As graphics processing units (GPUs) have become more powerful, interest in using these highly specialized processors for more general computational tasks has increased. A standard GPU die may have between 200 to 3000 individual processors, which makes them ideal for massively parallel tasks. An overview of this subject is beyond the scope of this work, but simulations like ours which utilize FFT are prime candidates for a performance boost using these specialized processors.

MATLAB, as part of its 'parallel computing toolbox', supports CUDA-enabled NVIDIA GPUs in a native way. Many basic MATLAB functions are capable of taking advantage of this capability, allowing a user to write code which with few modifications runs on both architectures. We took advantage of this ability to test what performance advantage it would give our nonlinear WG solver.

	Type	Spec.
Processors	2 x Xeon E5-2680v2	10 Cores, 2.8 GHz Each
System Memory	128 GHB DDR3	
GPUs	2 x NVIDIA Tesla K40	2880 Cores, 12 GB Memory
Software	Scientific Linux 6.5	
	MATLAB	

Table A.3.1: This is the specifications of the computer provided by Microway for NVIDIA's Tesla program.

The computer hardware for this test was provided by Microway through NVIDIA's Tesla test drive program. The hardware specifications of the computer are listed in Table A.3.1. The latest generation cards at the time of publication promise roughly twice the performance per card described here

Looking at the results, shown in Fig. A.3.2, leaves us with some key points. The most important to stress is that for this task, the MATLAB CUDA solution is very quick for large problems. For imput vectors of lenght 2^{17}, the speed increases by a factor of ≈ 12. Second, an improvement of over 2 can be had by optimizing the code using built-in matlab functions only. In this case, an older version of the code did not use the function `bsxfun`, but instead a for-loop.

However, the GPU solution has a fixed overhead of roughly 44 seconds. This may be due to transferring the matrices to the cards and setting up computation threads. Also, because the cards have a limited amount of memory (12 GB) compared to the system memory (128 GB in this case, but over 1 TB is possible), there are problems which would benefit from the large number of cores but cannot be used on this hardware because of memory constraints. We see the large increase because the speed of our simulation is limited by processor speed.

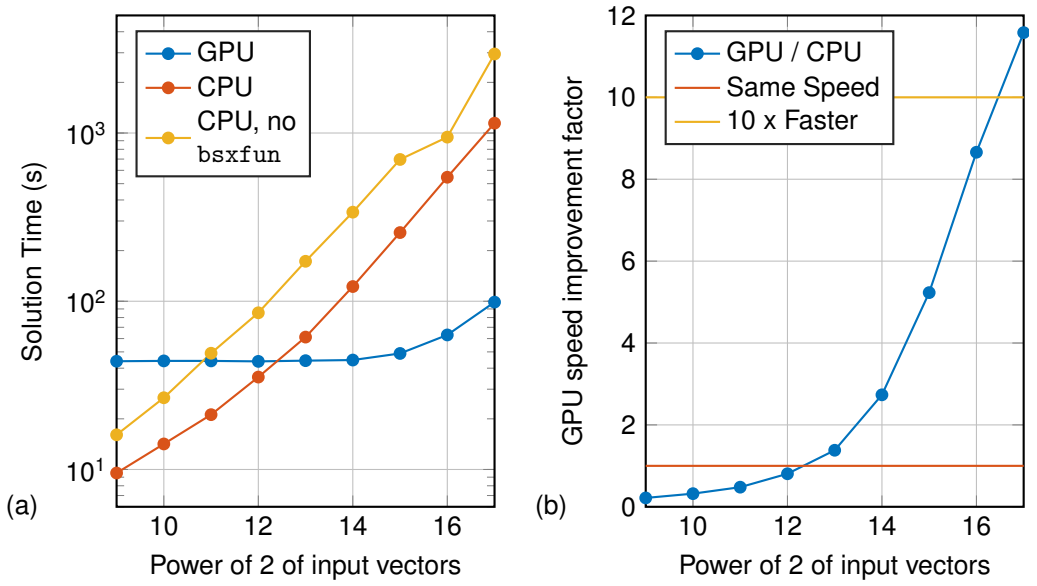

Figure A.3.2: The left plot (a) shows that the GPU solution is very quick, but only at large sizes can the speed compensate for the fixed overhead of setting up the computation. A straight comparison of the GPU to the CPU is shown in (b). This plot clearly shows the potential speedup for this computation.

A.3.3 GNU Octave Performance Comparison

GNU Octave is a freeware high-level programming language that is mostly compatible with MATLAB [102]. The software project provides a command-line utility and graphical interace. Because the project is open-source, operating systems and hardware that is not supported by MATLAB can execute standard MATLAB scripts and functions. We used this ability to test our split-step Fourier method solver on advanced RISC machine (ARM)-based devices.

Because this architecture is becomming more common and accessible, certain laboratory uses such as device control or simple calculation are possible at an extremely low price-point. In this quick comparsion, we use two devices to represent the high-performance and low-performance spectrum of these devices. The high-end

device is a Sony Z3 smartphone that has a 2.5 GHz, 4-core processor with 3 GB of random access memory (RAM) which runs Android. The low-end is represented by a first-generation Raspberry Pi B. This is a single-board computer sold for $35 and has a single-core 700 MHz processor with 256 MB of memory. Newer versions of this computer maintain the low pricepoint but are significantly faster.

In this test, it is clear that the ARM devices are significantly slower than an admittedly high-end x86-64 workstation by roughly an order of magnitude. However, as seen in Fig. A.3.3, it is clear that for smaller projects, these devices have acceptable performance. This is despite the very real possiblity that GNU Octave has not been well optimized for this alternative architecture. There are many factors at work to describe the performance difference beside the raw computational power of the processors, but it is beyond the scope of this discussion.

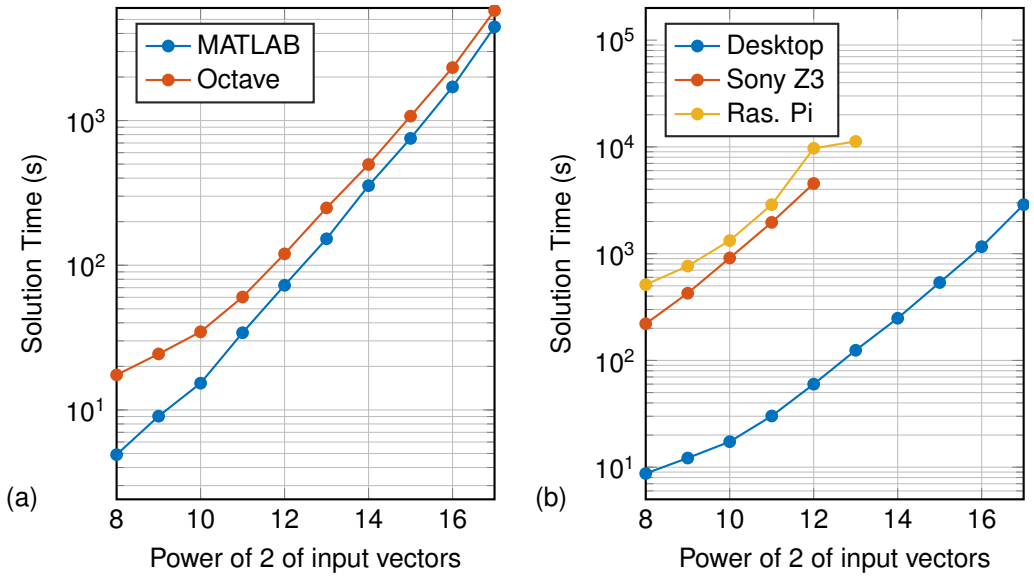

Figure A.3.3: (a) On the desktop, performance suffers when identical code is executed on GNU Octave compared to MATLAB. It's good to see the money goes somewhere! (b) The cross-platform nature of GNU Octave allows it to run on a variety of platforms unsupported by MATLAB. This plot compares the solution time for two ARM-based devices, a Sony Z3 smartphone and a first-generation Raspberry Pi B and our lab's 12-core workstation.

While it is unlikely that someone will use this method to run simulations on their smartphone, such a low-cost device could be used for data gathering and onboard analysis in a lab setting. Unlike a microcontroller (such a traditional Arduino), a Raspberry Pi runs a Linux distribution and has full networking and input/output (I/O) capability. However, it is cheaper and more compact than a traditional personal computer (PC).

A.3.4 MEX Implementation of Solver

MATLAB's MEX function generator allows a user to autogenerate C code from a MATLAB function. Certain problems that do not rely heavily on optimized build-in

functions or are hard to vectorize cane see a dramatic performance increase when implemented in this way. In this subsection, we tested this method on our nonlinear WG solver.

It should be noted that we made no optimizations to the MEX code generator or to the generated code itself. Figure A.3.4 shows the results of this trial. The autogenerated C code is actually significantly slower than the native MATLAB code. This is likely due to the fact that our code is easy to vectorize and relies heavily on functions that are already optimized.

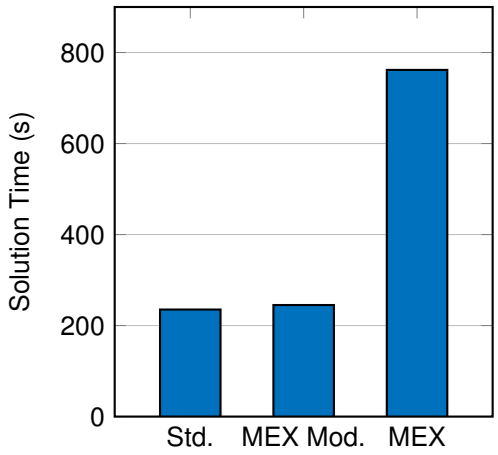

Figure A.3.4: The setting here is $2^{14} = 16384$. It is important to note that this trend will likely vary with the size of the array. The standard code is the heavily optimzied code shown in section A.1. The center bar represents a minimal modification of this native MATLAB code in order to support the MEX code generation. Finally, on the right is the execution time of the MEX code itself.

B Waveguide Complex Transfer Function Simulation

Typically, WGs require some form of quasi-phase matching. Periodic poling, as desribed in Subsection 2.2.2, flips the orientation of the crystal domains so that the phase relationship between the signal and pump never become greater than 180 degrees. However, variations or errors in fabrication can reduce the effective nonlinearity of the device through poorly defined or unflipped domains and variations in waveguide width, among others.

In this Appendix, we will focus on simulating the effects of WG width variations and their distortions have on the CTF of the device. Figure B.1.1 shows experimental results for SHG which is a direct measurement of the square of the magnitude of CTF. Understanding this effect helps us improve the simulations shown in Chapter 3, as discussed in Section 3.4.

B.1 Phase-Mismatch Error

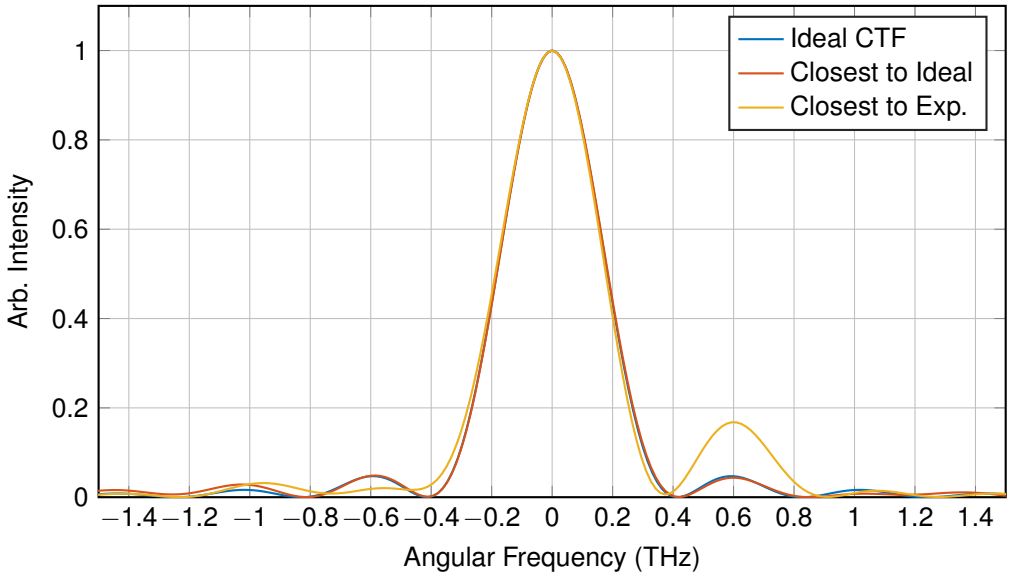

Figure B.1.1: Statistically simulated CTFs.

In order to simulate phase-mismatch, we assume that the poling of the waveguide is ideal, but the width of the WG varies. In the solver, we implement this change by replacing the pump/signal to upconverted phase-mismatch from a constant, Δk, to a function of the position, $\Delta k(z)$. We take

$$\Delta k(z) = \Delta k + \mathfrak{N}(\mu = 0, \sigma), \tag{B.1.1}$$

where $\mathfrak{N}$ is a set of random numbers from a Gaussian distribution with a mean of zero and a variable standard deviation, σ. The number of elements of the vector $\Delta k(z)$ is set by the length of the waveguide divided by the estimated correleation length of the waveguide width errors. Typically we estimate the width correlation length to be 1 or 2 mm. Figure B.1.2 shows an example of 100 runs with various correlation lengths and standard deviations.

For each randomly generated wavenumber-mismatch vector, we run the split-step Fourier solver in the low-conversion limit for CW SFG. If we consider $\hat{B}_i(z,\Omega)$ to be spectrum of the signal light, the output spectrum of the upconverted light can be calculated by

$$\hat{B}_i(L,\Omega) = \hat{d}(\Omega)\hat{B}_s^*(-\Omega)E_p \exp\{-i[k(\omega_i+\Omega)-k(\omega_i)]L\}, \tag{B.1.2}$$

where E_p is the pump amplitude. Because we only consider GVD between the C-band and the SFG frequency, the CTF is

$$\hat{d}(\Omega) = \frac{\hat{B}_i(L,\Omega)}{\hat{B}_s^*(-\Omega)E_p}, \tag{B.1.3}$$

where $\Omega = \omega - \omega_0$ is the detunning. With the result from the solver, we calculate $\hat{d}(\Omega)$.

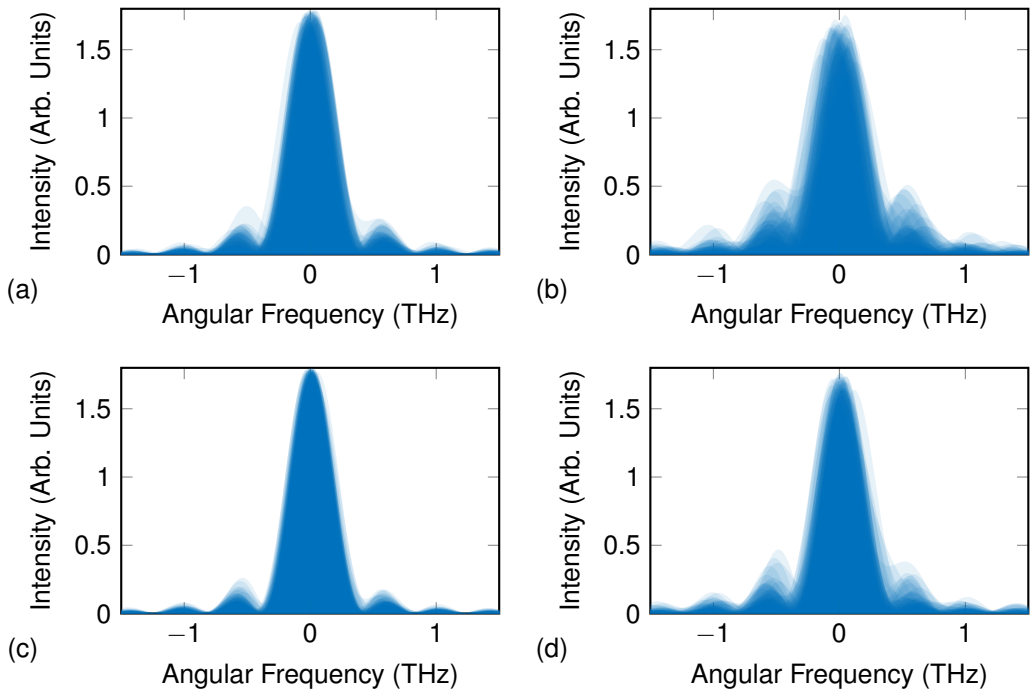

Figure B.1.2: A map of the CTF intensity for 100 random sampled $\Delta k(z)$ distributions. (a) has 23 samples with $\sigma = 1\,\mathrm{cm}^{-1}$. (b) has 23 samples with $\sigma = 2\,\mathrm{cm}^{-1}$. (c) has 46 samples with $\sigma = 1\,\mathrm{cm}^{-1}$. (b) has 46 samples with $\sigma = 2\,\mathrm{cm}^{-1}$.

To calculate the difference between simulated CTFs and the experimental data, we calculate the sum of squares of the difference,

$$S = \sum_{i=1}^{n} (y^i_{\mathrm{Cal}} - y^i_{\mathrm{Exp}})^2, \tag{B.1.4}$$

for the sum over the data points in the experimental data. Figure B.1.3 shows the best results from the samples in Figure B.1.2 compared to the SHG data.

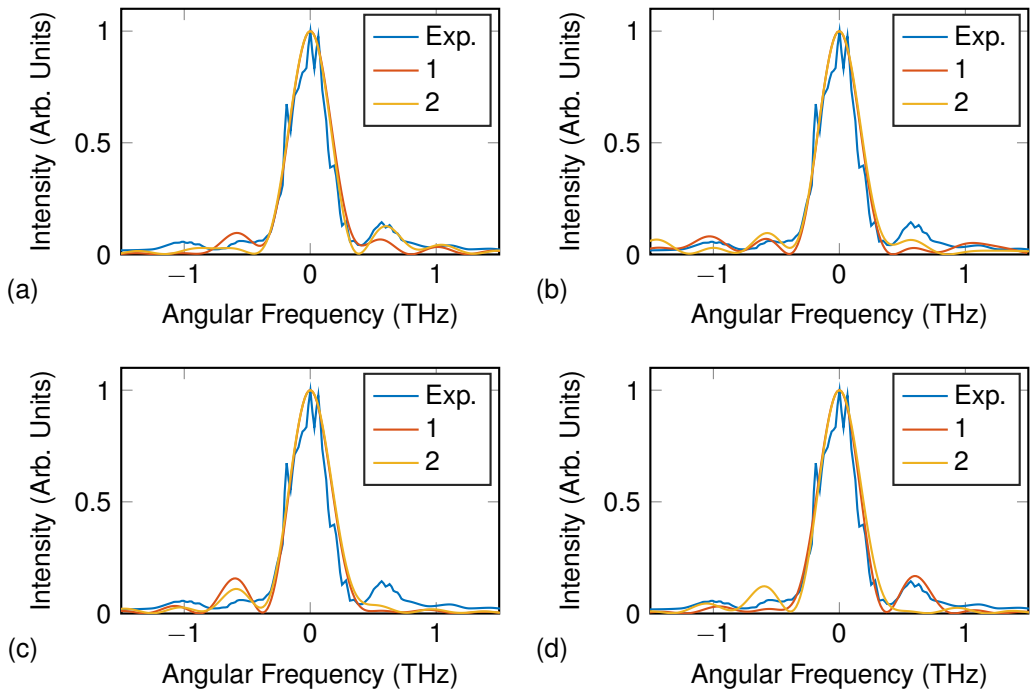

Figure B.1.3: 4 plots with the 2 smallest sum of squares. (a) has 23 samples with $\sigma = 1\,\mathrm{cm}^{-1}$. (b) has 23 samples with $\sigma = 2\,\mathrm{cm}^{-1}$. (c) has 46 samples with $\sigma = 1\,\mathrm{cm}^{-1}$. (d) has 46 samples with $\sigma = 2\,\mathrm{cm}^{-1}$.

C | Data Acquisition Code

Whenever possible and practical, we developed software to interface with test equipment to streamline data aquisition and processing. Initially based on Matlab code used to control an OSA with a broken front panel, the final version of the codebase is python-based, cross-platform (when possible) and supports 24 instruments.

Each instrument is represented by a python class which interfaces with it via General Purpose Interface Bus (GPIB), USB Test & Measurement Class (USBTMC), or specific drivers directly. While not all instrument functions are exposed to the user through these classes, the current capabilities are such that almost all data respented in this dissertation used this python codebase for data acquisition. Data taking is usually done via python scripting and saved into Matlab data files for analysis.

C.1 Supported Instruments

Table C.1.1 is a list of the supported instruments and the names of classes that expose their functionality to python. These files combined with the execution scripts are the two parts of the data acquisition codebase.

Instrument	Type	File Name
ANDO AQ6317B	OSA	`pyANDO.py`
Agilent 34401A	6.5 Digit Multimeter	`pyAgilPM.py`
Agilent 81531A	Optical Powermeter	`pyAgilPM.py`
Agiltron Switch	Optical Switch	`pyAgiltron4.py`
AxiDraw v3	Motion Controller	`pyAxiDraw.py`
BNC Model 645	50 MHz Func. Generator	`pyBNC.py`
Finisar WaveShaper 1000A	OAWG	`pyWaveShaper.py`
Finisar WaveShaper 4000A	OAWG	`pyWaveShaper4.py`
HP 8168F	Laser	`pyHP1998.py`
HP 8564EC	40 GHz ESA	`pyHPESA.py`
HP 83650B	50 GHz Signal Generator	`pyHPsweepSigGen.py`
HP 83731B	20 GHz Signal Generator	`pyHPsigGen.py`
JDSU TB9	Optical Filter	`pyJDSUfilter.py`
MCC USB-1208FS	Analog/Digital I/O	`pyMccDAQ.py`
NuPhotonics 2000	EDFA	`pyNuEDFA.py`
Pure Photonics PPCL200	Laser	`pyPPCL200.py`
Rigoll DS1302CA	Oscilloscope	`pyRigolWin.py`
Santec TLS-210	Laser	`pySANTEC.py`
SRS PTC10	PID Temp. Controller	`pySRStemp.py`
SRS SIM928	Voltage Source	`pySRSivs.py`
SRS SIM970	Digital Voltage Meter	`pySRSdvm.py`
Thorlabs PM100D	Optical Powermeter	`pyThorPM.py`
Thorlabs MDT693B	Piezo Motion Controller	`pyThorMove.py`
Thorlabs OSA203C	OSA	`pyOSA.py`

Table C.1.1: The listed instruments are supported by the python data acquisition codebase.

C.2 Python Instrument Class Examples

Listing C.2.1: Class to control the ANDO AQ6317B OSA.

```
# This is the rPi version, but should also work with Linux
# This should considered a fork and improvement from the
# Windows Version

import sys
import serial
import time
import numpy as np
import matplotlib.pyplot as plt

class pyANDO(object):

    comport = None

    def __init__(self,comport):
        self.comport = comport

    def close(self,s):
        s.close()

    def initANDO(self):
        addr = 03
        ser = serial.Serial(self.comport,9600,timeout=10)

        ser.write("++mode 1\n")
        ser.write("++addr " + str(addr) + "\n")
        ser.write("++auto 0\n")
        ser.write("++eoi 1\n")
        ser.write("++eos 3\n")
        return ser

    def ID(self):
        ser = self.initANDO()

        ser.write("++auto 0\n")
        ser.write("*IDN?\n")
        ser.write("++auto 1\n")
```

```
        # Tell the OSA to send data of Trace A
        idn = ser.readline()

        ser.close()
        return idn

    def max(self,l):
        ser = self.initANDO()
        if l == 0:
            ser.write("WRTA\n")
        if l == 1:
            ser.write("MAXA\n")

        ser.close()

    def setup(self,l,s,r,ref,scale):
        ser = self.initANDO()

        ser.write("CTRWL"+str(l)+"\n")
        ser.write("SPAN"+str(s)+"\n")
        ser.write("RESLN"+str(r)+"\n")
        ser.write("SMPL0\n")
        ser.write("REFL"+str(ref)+"\n")
        ser.write("LSCL"+str(scale)+"\n")
        ser.write("SMID\n")

        ser.write("RPT\n")
        ser.close()

    def lchange(self,l):
        ser = self.initANDO()
        ser.write("CTRWL"+str(l)+"\n")
        ser.close()

    def saveTrace(self,name):
        ser = self.initANDO()

        #ser.write("SGL\n")
        c = 1

        while (c == 1):
            time.sleep(0.5)
```

```
        ser.write("++auto␣0\n")
        ser.write("SWEEP?\n")
        ser.write("++auto␣1\n")
        c = ser.readline()
        ser.write("++auto␣0\n")
        if c == 0:
            ser.write("STP\n")

ser.write("++auto␣0\n")
ser.write("LDATA\n")
ser.write("++auto␣1\n")
# Tell the OSA to send data of Trace A
Ldat = ser.readline()
ser.write("++auto␣0\n")
ser.write("WDATA\n")
ser.write("++auto␣1\n")
# Tell the OSA to send Wavelength of Trace A
Wdat = ser.readline()
ser.write("++auto␣0\n")
time.sleep(5)
ser.write("RPT\n")
time.sleep(5)

ser.write("RESLN?\n")
ser.write("++auto␣1\n")
# Resolution of the measurement
res = ser.readline()
ser.write("++auto␣0\n")

ser.write("SMPL?\n")
ser.write("++auto␣1\n")
# Samples of measurement, 0 is AUTO
smpl = ser.readline()
ser.write("++auto␣0\n")

ser.write("SENS?\n")
ser.write("++auto␣1\n")
# Sensitivity
sens = ser.readline()
ser.write("++auto␣0\n")

ser.write("AVG?\n")
```

```
        ser.write("++auto␣1\n")
        # Averaging
        avg = ser.readline()
        ser.write("++auto␣0\n")
        ser.close()

        Ldat = Ldat.translate(None,'\r')
        Wdat = Wdat.translate(None,'\r')
        res = res.translate(None, '\r\n')

        smpl = smpl.translate(None, '\r\n')
        if smpl == '␣␣␣␣0':
            smpl = 'AUTO␣-␣See␣Sample␣Points'


        sens = sens.translate(None, '\r\n')
        sensDict = {'1': 'HIGH␣1\n',
                    '2': 'HIGH␣2\n',
                    '3': 'HIGH␣3\n',
                    '4': 'NORM␣RANG␣HOLD\n',
                    '5': 'NORM␣RANG␣AUTO\n',
                    '6': 'MID\n'}

        avg = avg.translate(None, '\r\n')

        resS = 'RES:␣'+res+'␣nm\n'
        smplS = 'SAMPLES:␣'+smpl+'\n'
        sensS = 'SENSITIVITY:␣'+sensDict[sens[0]]

        avgS = 'AVERAGING:␣'+avg+'␣SAMPLES\n'

        f = open(name+'.csv', 'w')
        f.write(resS)
        f.write(smplS)
        f.write(sensS)
        f.write(avgS)
        f.write(Wdat)
        f.write(Ldat)
        f.close()

    def showTrace(self):
        ser = self.initANDO()
```

```
#ser.write("SGL\n")
c = 1

while (c == 1):
    time.sleep(0.5)
    ser.write("++auto␣0\n")
    ser.write("SWEEP?\n")
    ser.write("++auto␣1\n")
    c = ser.readline()
    ser.write("++auto␣0\n")
    if c == 0:
        ser.write("STP\n")



ser.write("++auto␣0\n")
ser.write("LDATA\n")
ser.write("++auto␣1\n")
Ldat = ser.readline()
ser.write("++auto␣0\n")
ser.write("WDATA\n")
ser.write("++auto␣1\n")
Wdat = ser.readline()
ser.write("++auto␣0\n")
time.sleep(5)
ser.write("RPT\n")
time.sleep(5)

ser.write("RESLN?\n")
ser.write("++auto␣1\n")
res = ser.readline()
ser.write("++auto␣0\n")

ser.write("SMPL?\n")
ser.write("++auto␣1\n")
smpl = ser.readline()
ser.write("++auto␣0\n")

ser.write("SENS?\n")
ser.write("++auto␣1\n")
sens = ser.readline()
```

```
ser.write("++auto␣0\n")

ser.write("AVG?\n")
ser.write("++auto␣1\n")
avg = ser.readline()
ser.write("++auto␣0\n")
ser.close()

Ldat = Ldat.translate(None,'\r')
Wdat = Wdat.translate(None,'\r')
res = res.translate(None, '\r\n')

smpl = smpl.translate(None, '\r\n')
if smpl == '␣␣␣␣0':
    smpl = 'AUTO␣-␣See␣Sample␣Points'


sens = sens.translate(None, '\r\n')
sensDict = {'1': 'HIGH␣1\n',
            '2': 'HIGH␣2\n',
            '3': 'HIGH␣3\n',
            '4': 'NORM␣RANG␣HOLD\n',
            '5': 'NORM␣RANG␣AUTO\n',
            '6': 'MID\n'}
avg = avg.translate(None, '\r\n')

resS = 'RESOLUTION:\t'+res+'␣nm'
smplS = 'SAMPLES:\t'+smpl
sensS = 'SENSITIVITY:\t'+sensDict[sens[0]]

avgS = 'AVERAGING:\t'+avg.strip()+'␣SAMPLES'


x = np.array(map(float,Wdat.split(',')[1:]))
y = np.array(map(float,Ldat.split(',')[1:]))

plt.plot(x,y)
if np.min(y) < -110:
    maxY = np.max(y)
    plt.ylim((-85,maxY+5))

plt.xlabel('Wavelength␣(nm)')
```

```
        plt.ylabel('Power (dBm)')
        plt.title('ANDO AQ6317B Trace A')
        plt.grid(True)

        print(resS)
        print(smplS)
        print(sensS)
        print(avgS)
        print('SAMPLES:\t'+Wdat.split(',')[0].strip())
        plt.show()

    def send(self,comm):
        ser = self.initANDO()
        ser.write(comm+"\n")
        ser.write("++auto 1\n")
        out = ser.readline()
        ser.write("++auto 0\n")
        ser.close()

        return out

    def returnTrace(self):
        ser = self.initANDO()

        #ser.write("SGL\n")
        c = 1

        while (c == 1):
            time.sleep(0.5)
            ser.write("++auto 0\n")
            ser.write("SWEEP?\n")
            ser.write("++auto 1\n")
            c = ser.readline()
            ser.write("++auto 0\n")
            if c == 0:
                ser.write("STP\n")

        ser.write("++auto 0\n")
        ser.write("LDATA\n")
        ser.write("++auto 1\n")
        Ldat = ser.readline()
        ser.write("++auto 0\n")
```

```
        ser.write("WDATA\n")
        ser.write("++auto␣1\n")
        Wdat = ser.readline()
        ser.write("++auto␣0\n")
        time.sleep(5)
        ser.write("RPT\n")

        npW = np.fromstring(Wdat, sep=',')[1:]
        npL = np.fromstring(Ldat, sep=',')[1:]
        return (npW,npL)
```

Listing C.2.2: Class to control the Santec TLS-210 Tunable Laser.

```
# This is the updated version, for Windows and Linux

import sys
import serial
import time
import numpy as np
import readchar
import matplotlib.pyplot as plt

class pySANTEC(object):

    comport = None

    def __init__(self,comport):
        self.comport = comport

    def close(self,s):
        s.close()

    def initSANTEC(self,timeOut,mode):
        addr = 01
        ser = serial.Serial(self.comport,19200,
                            timeout=timeOut)

        ser.write("++mode␣1\n")
        ser.write("++addr␣" + str(addr) + "\n")
        ser.write("++auto␣" + str(mode) + "\n")
        ser.write("++eoi␣1\n")
```

```
        ser.write("++eos␣3\n")


        return ser

    def on(self,co):
        ser = self.initSANTEC(1,0)

        ser.write("LO\n")
        # coherence mode? Off for narrow line width
        if co == True:
            ser.write("CO\n")

        time.sleep(5)
        ser.close()

    def off(self):
        ser = self.initSANTEC(1,0)

        ser.write("CF\n")
        ser.write("LF\n")
        time.sleep(3)
        ser.close()


    def lamChange(self, l):
        ser = self.initSANTEC(0.5,1)

        ser.write("WA␣{:.3f}".format(l)+"\n")

        tune = '1'
        ser.write("SU\n")
        ser.readline()[-1]

        while tune != '0':
            ser.write("SU\n")
            tune = ser.readline()[-1]

        ser.close()

    def mwChange(self,mW):
        ser = self.initSANTEC(0.5,0)
```

```
        ser.write("LP␣"+str(mW)+"\n")
        time.sleep(1)
        ser.close()


    def fine(self, l):
        ser = self.initSANTEC(0.5,0)

        ser.write("FT␣"+str(l)+"\n")
        time.sleep(1)
        ser.close()

    def wrt(self, l):
        ser = self.initSANTEC(0.5,1)

        ser.write(str(l)+"\n")
        out = ser.readline()
        time.sleep(1)
        ser.close()
        return out

    def chk(self):
        ser = self.initSANTEC(0.5,1)
        ser.write("SU\n")
        status = ser.readline()
        ser.close()
        return status

    def sweepLam(self,lamVec,delay,out):

        ser = self.initSANTEC(0.05,1)

        for ii in range(lamVec.size):
            ser.write("WA␣{:.3f}".format(lamVec[ii])+"\n")

            tune = '1'
            ser.write("SU\n")
            ser.readline()[-1]

            while tune != '0':
                ser.write("SU\n")
```

```
                tune = ser.readline()[-1]

            if delay != 0:
                time.sleep(delay)

            if out == True:
                print(format(ii)+': Lambda = {:.3f}'.
                        format(lamVec[ii])+' nm')

        ser.close()

    def moveLam(self):

        ser = self.initSANTEC(0.05,1)

        stepV = np.array([0.001,0.002,0.005,0.01,0.02,
                        0.05,0.1,0.2,0.5,1,2,5,10,20])

        inChar = 'a'
        stepInd = 2
        step = stepV[stepInd]
        print('<--- Change Wavelength - Step Size: '
              +str(step)+' nm --->')

        while inChar != 'q':

            inChar = readchar.readkey()
            if inChar == '8':

                ser.write('WA\n')
                lam = ser.readline()[-8:]
                ser.write("WA {:.3f}".
                          format(float(lam)+step)+"\n")

                tune = '1'
                ser.write("SU\n")
                ser.readline()[-1]

                while tune != '0':
                    ser.write("SU\n")
                    tune = ser.readline()[-1]
```

```
                ser.write('WA\n')
                print('Lambda: '+ser.readline()+' nm')

            if inChar == '2':

                ser.write('WA\n')
                lam = ser.readline()[-8:]

                ser.write("WA {:.3f}".
                          format(float(lam)-step)+"\n")

                tune = '1'
                ser.write("SU\n")
                ser.readline()[-1]

                while tune != '0':
                    ser.write("SU\n")
                    tune = ser.readline()[-1]

                ser.write('WA\n')
                print('Lambda: '+ser.readline()+' nm')

            if inChar == '+':
                if stepInd < stepV.size-1:
                    stepInd += 1
                    step = stepV[stepInd]

                print('Step Size: '+str(step)+' nm')

            if inChar == '-':
                if stepInd > 0:
                    stepInd -= 1
                    step = stepV[stepInd]

                print('Step Size: '+str(step)+' nm')

        print('<---+---+---+- Done -+---+---+--->')


        ser.close()

    def status(self):
```

```
        ser = self.initSANTEC(0.5,1)

        ser.write("WA\n")
        ser.readline()

        print("<<---+---␣TSL-210␣Laser␣Status␣---+--->>")

        ser.write("WA\n")
        print('Wavelength:\t\t␣'+ser.readline()+'␣nm')
        ser.write("FT\n")
        print('Fine␣Tunning:\t\t␣'+ser.readline())
        ser.write("OP\n")
        print('Power:\t\t\t␣'+ser.readline()+'␣dBm')
        ser.write("LP\n")
        print('Power:\t\t\t␣'+ser.readline()+ '␣mW')
        ser.write("CV\n")
        print('Coherence␣Level:\t␣'+ser.readline())

        print("<<---+---+---+---+----+---+---+---+--->>")


        ser.close()
```

Listing C.2.3: Class to control the Thorlabs Powermeter.

```
from ThorlabsPM100 import ThorlabsPM100
import numpy as np
import visa

class pyThorPM(object):

    comport = None

    def __init__(self,comport):
        self.comport = comport

    def initThorlabsPM(self):
        rm = visa.ResourceManager()
        inst = rm.open_resource(self.comport)
        pm = ThorlabsPM100(inst=inst)
```

```
        return pm

    def ID(self):

        rm = visa.ResourceManager()
        port = rm.open_resource(self.comport);
        idn = port.query('*IDN?')

        return idn

    def sensorID(self):
        pm = self.initThorlabsPM()
        idn = "Thorlabs PM100D Sensor: "
              +pm.system.sensor.idn

        return idn

    def power(self,out):
        pm = self.initThorlabsPM()
        mW = pm.read*1e3
        dBm = 10*np.log10(mW)

        if out == True:
            print("{:1.3e}".format(mW) + " mW ({:6.4f}".
                    format(dBm) + ' dBm)')

        return mW
```

Listing C.2.4: Class to control the Finisar WaveShaper 1000A OAWG.

```
from wsapi import *
import time
import numpy as np

class pyWaveShaper(object):

    wsConfig = None

    def __init__(self,wsConfig):
        self.wsConfig = wsConfig
```

```
def ID(self):
    ws_create_waveshaper('ws1',self.wsConfig)
    sno = ws_get_sno('ws1')
    con = ws_get_configversion('ws1')
    ws_delete_waveshaper('ws1')

    idn = "Serial Number :"+sno+
          ", Config Version :"+con

    return idn

def allBlock(self):
    ws_create_waveshaper('ws1',self.wsConfig)

    wsFreq = np.arange(191.25,196.275,0.001)
    wsAtten = 60*np.ones(wsFreq.size)
    wsPhase = np.zeros(wsFreq.size)
    wsPort = np.zeros(wsFreq.size)

    profileWS = ''
    for ii in range(wsFreq.size):
        profileWS = profileWS+
        '{:0.3f}'.format(wsFreq[ii])+
        '\t{:0.3f}'.format(wsAtten[ii])+
        '\t{:0.3f}'.format(wsPhase[ii])+
        '\t{:0.3f}'.format(wsPort[ii])+'\n'

    ws_load_profile('ws1',profileWS)
    ws_delete_waveshaper('ws1')

def allTransmit(self):
    ws_create_waveshaper('ws1',self.wsConfig)

    wsFreq = np.arange(191.25,196.275,0.001)
    wsAtten = 0*np.ones(wsFreq.size)
    wsPhase = np.zeros(wsFreq.size)
    wsPort = np.ones(wsFreq.size)

    profileWS = ''
    for ii in range(wsFreq.size):
        profileWS = profileWS+
        '{:0.3f}'.format(wsFreq[ii])+
```

```
            '\t{:0.3f}'.format(wsAtten[ii])+
            '\t{:0.3f}'.format(wsPhase[ii])+
            '\t{:0.3f}'.format(wsPort[ii])+'\n'

        ws_load_profile('ws1',profileWS)
        ws_delete_waveshaper('ws1')

    def loadProfile(self,wsFreq,wsAtten,wsPhase,wsPort):
        ws_create_waveshaper('ws1',self.wsConfig)
        # Error checking goes here

        profileWS = ''
        for ii in range(wsFreq.size):
            profileWS = profileWS+
            '{:0.3f}'.format(wsFreq[ii])+
            '\t{:0.3f}'.format(wsAtten[ii])+
            '\t{:0.3f}'.format(wsPhase[ii])+
            '\t{:0.3f}'.format(wsPort[ii])+'\n'

        ws_load_profile('ws1',profileWS)
        ws_delete_waveshaper('ws1')

    def loadProfileWindow(self,centerFreq,widthFreq,
                          attenWindow,phaseWindow):

        wsFreq = np.arange(191.25,196.275,0.001)
        wsAtten = 60*np.ones(wsFreq.size)
        wsPhase = np.zeros(wsFreq.size)
        wsPort = 0*np.ones(wsFreq.size)

        for ii in range(centerFreq.size):
            indexInit = np.where(
                        np.abs(wsFreq-centerFreq[ii])
                        <1e-5)[0][0]
            indexDiff = widthFreq[ii]/0.001/2
            index0 = int(indexInit-indexDiff)
            index1 = int(indexInit+indexDiff)

            wsAtten[index0:index1] = attenWindow[ii]
            wsPhase[index0:index1] = phaseWindow[ii]
            wsPort[index0:index1] = 1
```

```
        self.loadProfile(wsFreq,wsAtten,wsPhase,wsPort)
        return [wsFreq,wsAtten,wsPhase,wsPort]
```

D Lithium Niobate Simulation

In collaboration with Prof. Fathpour's group, we are interested in testing their unique WG for nonlinear optics [22]. The device consists of a patterned Si_3N_4 ridge which defines the guiding region on a LN wafer bonded to a silicon-on-insulator wafer.

In this Appendix, we show some preliminary simulations of these devices. The first section contains an overview of the geometry of the waveguide and plots of the mode shapes. The second section takes the dispersion calculated from the simulation to estimate the QPM grating for SHG and SFG between the telecom C-band and roughly 750 nm.

D.1 Geometry

The cross-section of the waveguide is formed by bonding a 400-nm-thick film of Y-cut LN with a 400-nm by 2 μm Si_3N_4 ridge. Figure D.1.1 shows this geometry and Figure D.1.2 shows the indices of refraction for the materials involved in the simulation. Figure D.1.3 shows the guided modes.

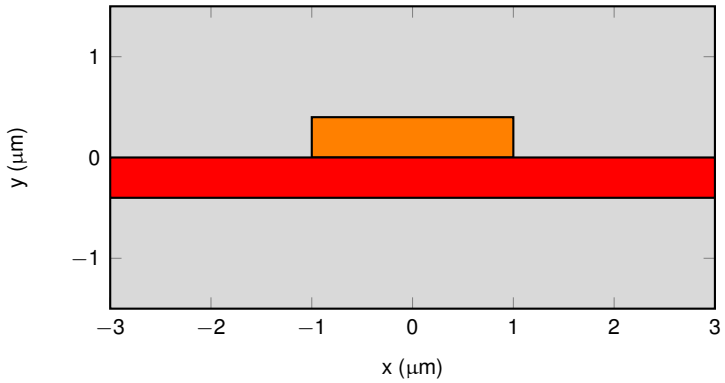

Figure D.1.1: The simulated cross-section. The orange section is the silicon nitride loading ridge. The red represents lithium niobate. The waveguide is encased in SiO_2.

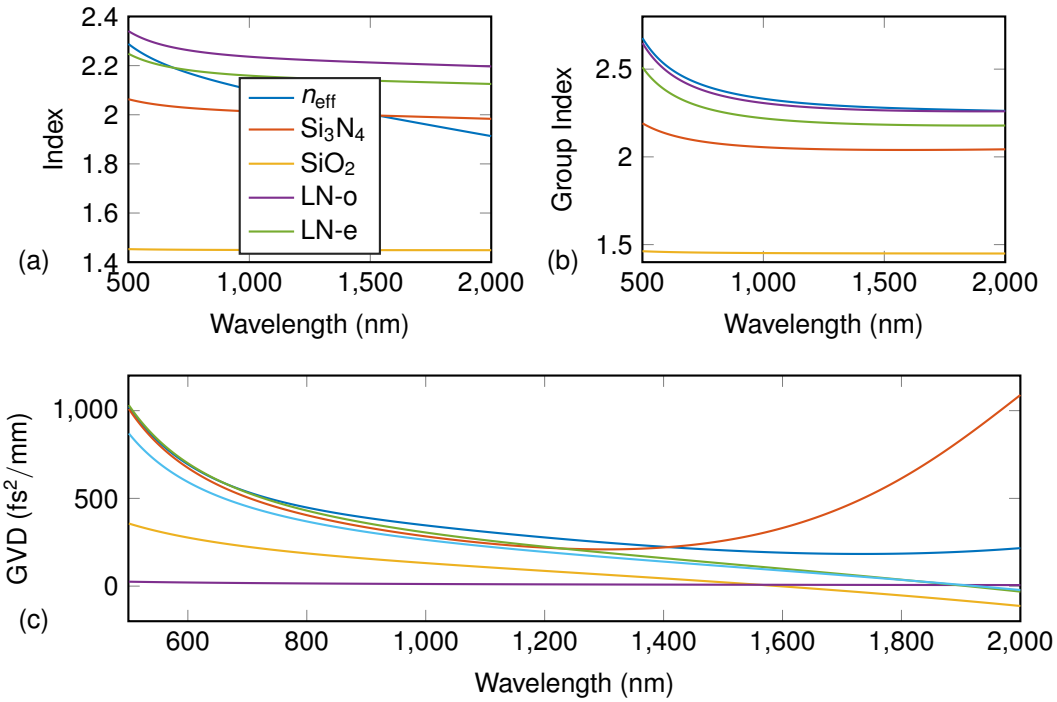

Figure D.1.2: The refractive index, (a), group index, (b), and the group-velocity dispersion, (c) of the materials in the simulations, plus the effective index of the waveguide.

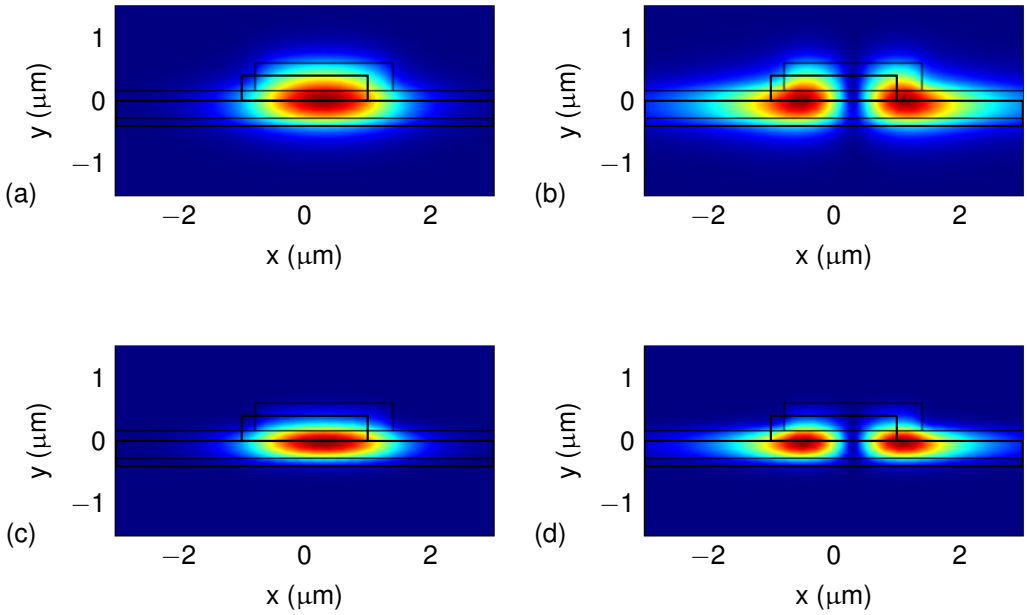

Figure D.1.3: Electric field magnitude for the first two guiding modes of the WG. (a,c) is fundamental mode, while (b, d) is the secondary mode. (a, b) are at 1560 nm, while (c, d) are at the SH of 780 nm.

D.2 Poling Period

The WG needs a QPM grating to facilitate phase-matching between the a pump in the 1500-1650 nm spectrum window and the band which roughly corresponds to it's SHG.

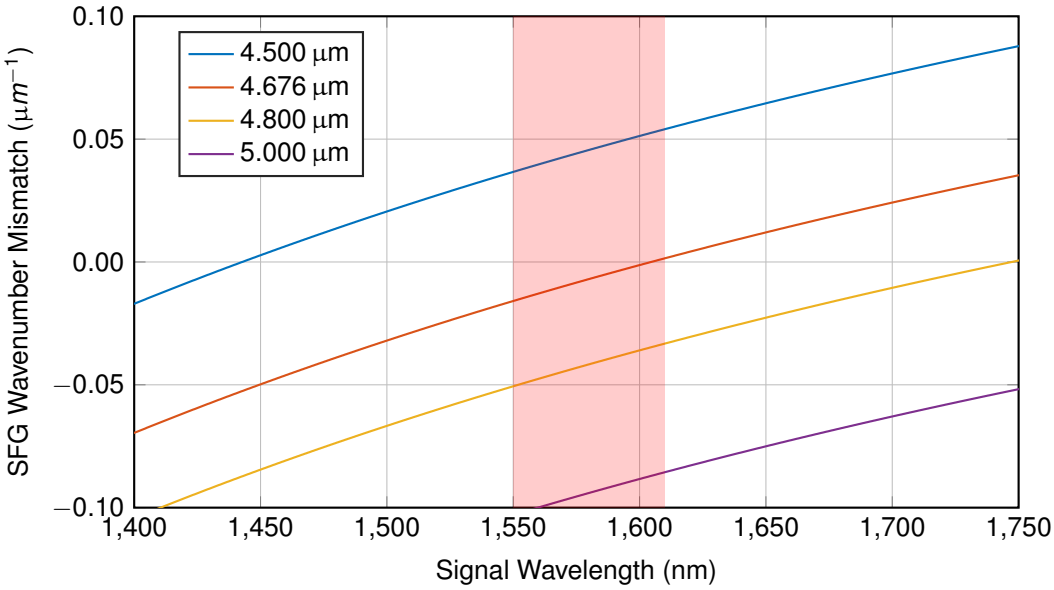

Figure D.2.1: A plot of different grating periods. The sum-frequency phase-mismatch is 0 near 1610 nm for a grating period of 4.676 μm.

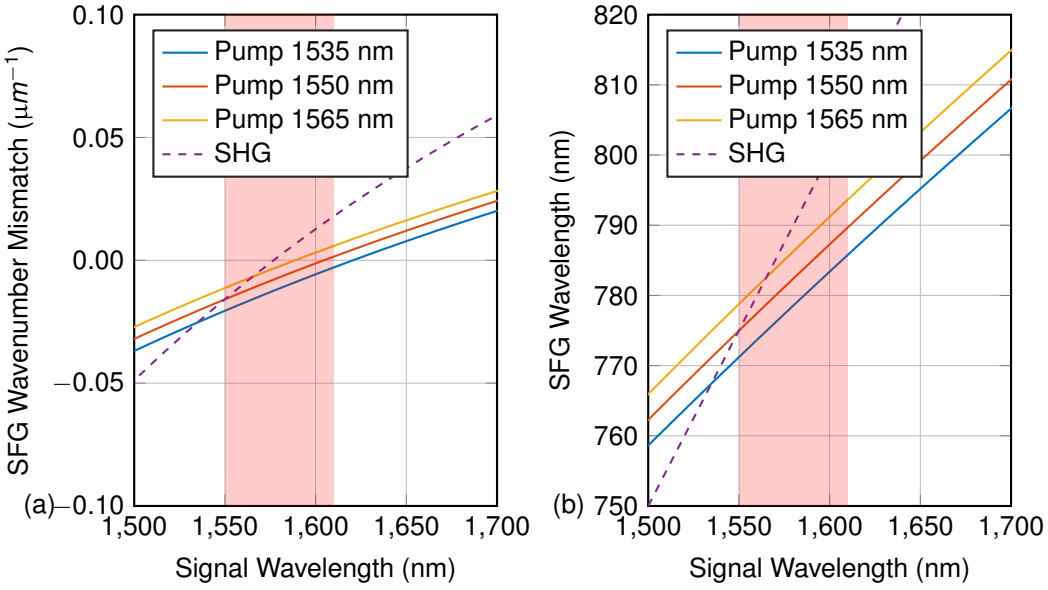

Figure D.2.2: (a), a comparison of the phase mis-match with a grating of 4.676 μm for SHG pumped at 3 different wavelengths and SHG. (b) plots SFG wavelength vs signal wavelength.